Optical Characterization of III Nitride Semiconductors Using Cathodoluminescence Techniques

by

Yu Huang

A Dissertation Presented in Partial Fulfillment
of the Requirements for the Degree
Doctor of Philosophy

Approved October 2011 by the
Graduate Supervisory Committee:

Fernando A. Ponce, Chair
Kong-Thon Tsen
Michael Treacy
Jeffery Drucker
Robert Culbertson

ARIZONA STATE UNIVERSITY

December 2011

ABSTRACT

Group III-nitride semiconductors have attracted much attention for applications on high brightness light-emitting diodes (LEDs) and laser diodes (LDs) operating in the visible and ultra-violet spectral range using indium gallium nitride in the active layer. However, the device efficiency in the green to red range is limited by quantum-confined Stark effects resulting from the lattice mismatch between GaN and InGaN. In this dissertation, the optical and micro-structural properties of GaN-based light emitting structures have been analyzed and correlated by utilizing cathodoluminescence and transmission electron microscopy techniques. In the first section, optimization of the design of GaN-based lasers diode structures is presented. The thermal strain present in the GaN underlayer grown on sapphire substrates causes a strain-induced wavelength shift. The insertion of an InGaN waveguide mitigates the mismatch strain at the interface between the InGaN quantum well and the GaN quantum barrier. The second section of the thesis presents a study of the characteristics of thick non-polar *m*-plane InGaN films and of LED structures containing InGaN quantum wells, which minimize polarization-related electric fields. It is found that in some cases the in-plane piezoelectric fields can still occur due to the existence of misfit dislocations which break the continuity of the film. In the final section, the optical and structural properties of InGaAlN quaternary alloys are analyzed and correlated. The composition of the components of the film is accurately determined by Rutherford backscattering spectroscopy.

To My Parents

ACKNOWLEDGMENTS

Firstly, I would like to thank my advisor, Prof. Fernando Ponce, for giving me the great opportunity to study in his research group. I am indebted to his generous support and visionary guidance during my PhD study.

I would like to thank all the former and current group members, namely, Dr. Zhihao Wu, Dr. Jacob Brooskby, Dr. Alec Fischer, Qiyuan Wei, Kewei Sun, Ti Li, Reid Juday, Jingyi Huang, and Yong Wei. Special thanks to Dr. Alec Fischer for teaching me the CL techniques.

I would also like to thank my committee members: Prof. Jeffery Drucker, Prof. Kong-Thon Tsen, Prof Michael Treacy, and Prof. Robert Culbertson for thoughtful insights and helpful comments for this dissertation.

Finally, I want to thank Prof. Russell Dupuis and his group at the Georgia Institute of Technology; Dr. Toshiya Yokogawa from Panasonic Corporation, Japan; and Prof. Hiroshi Amano from Meijo University, Japan, for providing samples and interesting problems that are the subject of the research reported here.

TABLE OF CONTENTS

Page

CHAPTER Page

CHAPTER Page

CHAPTER Page

CHAPTER Page

LIST OF TABLES

LIST OF FIGURES

Figure Page

Figure Page

Figure Page

CHAPTER 1

INTRODUCTION TO SOLID STATE LIGHTING MATERIALS

1.1. BACKGROUND OF LIGHTING HISTORY

Few technologies have affected human life more than artificial light, from the way we work and play, to industry, education, and warfare. Artificial lighting technologies are crucial for modern civilizations. The evolution of luminous efficacy for lighting technologies in the past fifty years, shown in Fig. 1.1, results from a constant search for light sources with higher efficiency. The success of lighting technologies has depended to a great extent on the development of the materials that are used to generate light.

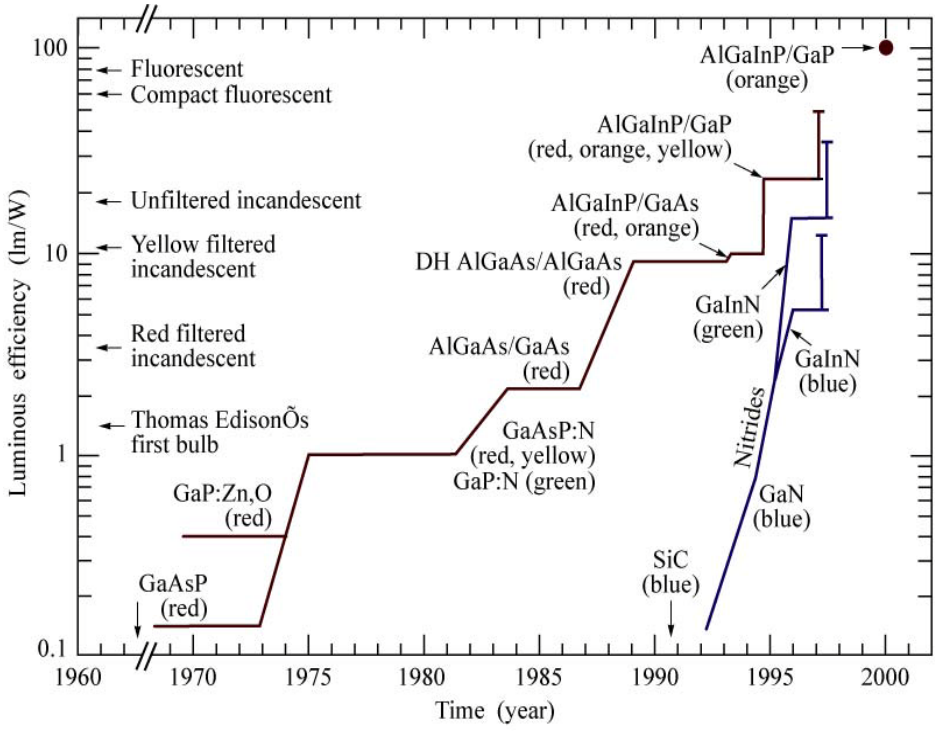

FIG. 1.1. Evolution of luminous efficacy for various lighting technologies showing the history of development of solid state lighting.[1]

Controllable fire is the first artificial lighting source that was produced by striking certain stones together or rubbing wood against wood. Fire is an inefficient light source since most of its black body emission falls in the infrared range that cannot be detected by the human eye but that is felt by the skin. The incandescent lamp, developed independently by Joseph Swan and Thomas Edison in 1879, was the first realization of light from electricity. Typical incandescent lamps have a luminous efficacy of about 16 lm/W and an overall efficiency of 4%.[2-5] Fluorescent lamps, invented in 1939, use electricity to excite a low-pressure gas to emit sharp atomic lines.[2-5] White light is produced by down-conversion of the atomic lines into longer-wavelengths using phosphor coatings. Because the reemitted light is in the visible range, the efficiency of fluorescent lamps is much higher than that of incandescent lamps. The efficacy of a fluorescent lamp based on mercury vapor is limited to about 71 lm/W, with an overall efficiency of 18%. This is due to the unavoidable energy loss in converting 250 nm UV photons into visible ones. In contrast, solid-state lighting involves direct conversion of electricity into visible light using light-emitting diodes (LEDs). It can theoretically achieve 100% conversion efficiency, by avoiding thermal losses such as the generation of infrared radiation in the incandescent lamps or plasmas in fluorescent lamps.

1.2.SOLID STATE LIGHTING MATERIALS

Ideal materials for solid-state lighting should satisfy three important criteria: (a) a direct band gap within the visible spectrum, (b) the availability of p and n doping to allow electron-hole recombination, and (c) physical and chemical stability to withstand high current operation and manufacturing processing. Fig. 1.2 shows the band gap versus the chemical bond length for the main semiconductor materials that are candidates for solid state lighting.

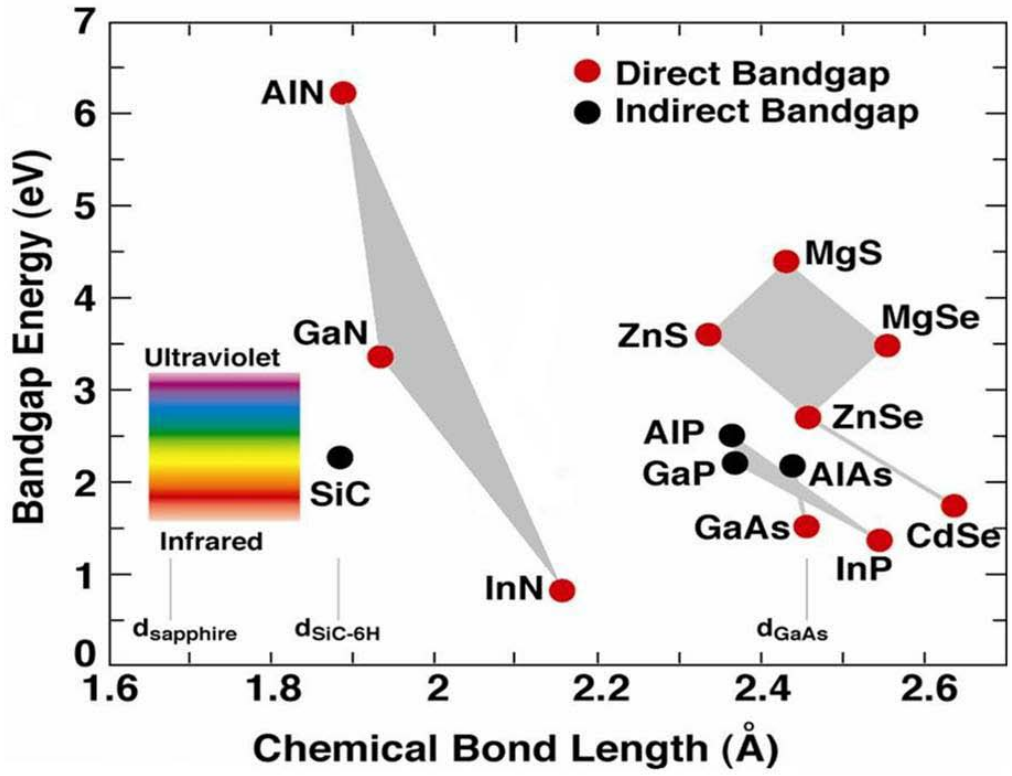

*FIG. 1.2.*Band gap versus chemical bond length for typical compound semi-conductors.[1]

Red to infrared LEDs are produced using III-V materials such as GaAsP,[6] and AlGaAs[7,8]; while green LEDs are produced using GaP doped with nitrogen.[9] But the efficiency is low and the wavelength coverage is limited by direct-indirect band gap transitions. High brightness, high efficiency LEDs emitting from yellow to infrared are fabricated using InAlGaP alloys,[10] however, the lowest emission wavelength is around 570 nm, due to a direct-indirect band gap transition. The III nitrides are the most recently developed materials that have the advantage of high brightness in the ultraviolet to green regime, while retaining a direct band gap within the compositional range.

1.3. III-NITRIDE MATERIAL PROPERTIES

The III-V nitride system includes three binary compounds consisting of aluminum nitride (AlN), gallium nitride (GaN), and indium nitride (InN); three ternary compounds of $Al_xGa_{1-x}N$, $In_xGa_{1-x}N$, and $In_xAl_{1-x}N$; and the quaternary compounds $Al_xIn_yGa_{1-x-y}N$. The band gap coverage range is from 6.2 eV for AlN to approximately 0.7 eV for InN, which allows emission from ultraviolet to infrared, respectively. Some of the physical properties of III-V nitride wurtzite binary compounds are listed in Table 1.1. III-nitrides are present in two forms as cubic zinc blende and hexagonal wurtzite, depending on the growth conditions. The wurtzite structure is more thermodynamically stable than zinc blende under normal conditions. In the zinc blende case, the stacking sequence of the {111} planes is ABCABC, and in the wurtzite case, the stacking sequence perpendicular to the {0001} basal planes is ABABAB. The wurtzite structure has a hexagonal

symmetry corresponding to space group C_{6v}^4(P6$_3$mc). The four-index notation[11] (**a**$_1$, **a**$_2$, **a**$_3$, **c**) is expressed by three equivalent a-axes parallel to the basal planes and a *c*-axis perpendicular to them. Four-axes Miller-Bravais indices better embody the 6-fold in-plane symmetry, which is, planes from same family will have the same form but a rotation between **a**-indices. The wurtzite structure can be visualized as two interpenetrating hexagonal sublattices of cations and anions with a shift along the [0001] axis with each anion surrounded by four cations at the corners of a tetrahedron, and vice versa. The deviation of the cation (anion) position from the center of the anion (cation) tetrahedra (ideal ratio of *c*/*a* is 1.633),[12] introduces spontaneous polarization. The *c*/*a* ratios for III-N semiconductors are also included in Table 1.1. Additionally, a lack of a center of symmetry in the wurtzite structure results in piezo-electric fields when an external strain, such as due to lattice mismatch, is applied on this structure.

Table 1.1.

Basic physical properties of the III-V nitride materials.[12-14]

Physical properties	**AlN**	**GaN**	**InN**
Lattice Constants (300K)			
a (Å)	3.111	3.189	3.538
c (Å)	4.979	5.185	5.703
c/*a* ratio	1.606	1.634	1.618
E_G(eV) (300K)	6.2	3.39	0.7
Thermal Expansion Coefficient (300K)			
a ($\times 10^{-6}K^{-1}$)	4.2	5.59	5.7
c ($\times 10^{-6}K^{-1}$)	5.3	3.17	3.7
Bond Length (Å)	1.89	1.94	2.15
Cohesive Energy per Bond (eV)	2.88	2.24	1.93
Melting Point (°C)	>3000	>2500	>1100
Bulk Modulus (Gpa) (300 K)	210	210±10	140

1.4.BREAKTHROUGH AND CHALLENGES OF III-V NITRIDES

Although III-nitride semiconductors have been known for many years, failure to grow high-quality films due to a large difference in lattice constants and thermal expansion coefficients between the epitaxial film and the substrate have prevented progress in the development of III-V nitrides. High-quality GaN films were first obtained by growing low-temperature AlN[15,16] and GaN[17] buffer layers, which accommodate the lattice mismatch between film and substrate and make two-dimensional nucleation possible.

Another major difficulty in achieving commercial III-nitride devices related to successful n- and p-type doping. It is well know that unintentionally doped GaN film is natively n-type due to the presence of defects and impurities. Magnesium was considered a good candidate as p-type dopant. However, even high concentrations of Mg in GaN did not necessarily lead to good p-type conductivity. The film remained highly-resistive, which was later understood due to unintentional hydrogen atoms passivating Mg acceptors by forming Mg-H complexes.[18] In 1989, Amano *et al.* first achieved p-type conductivity by using low-energy electron beam irradiation (LEEBI) to activate the magnesium.[19] In 1991, Nichia obtained p-type conductivity utilizing post-growth annealing in a nitrogen gas atmosphere.[20] Since the acceptor level of Mg is relatively high at 200 meV above valence band, a doping level of $10^{20}cm^{-3}$ is necessary in order to have a free hole concentration of $10^{18}cm^{-3}$.

Also, high-quality InGaN films used in the active region is crucial for nitride-based LED for visible and UV light emission. Researchers in Nichia Corporation firstly achieved it by using a two-flow MOCVD growth method.[21] Later, blue, green, and yellow LEDs, blue and violet emitting laser diodes became viable successively.[22-24]

1.4.1. THE SEARCH FOR SUITABLE SUBSTRATES

Lacking suitable substrates is one of the major challenges for growing good quality III-V nitride semiconductors. Sapphire[25,26] is commercially available as a single crystal substrate with diameters of 100 mm and above. It acts as a transparent window over the spectral range needed to study GaN optically while confining carrier transport to the epi-layer grown on top due to its electrically insulating properties. The structure of sapphire (Al_2O_3) is a hexagonal closed-packed structure stacked up along the c-direction. The aluminum and oxygen planes alternate in the stacking sequence. The oxygen sub-lattice is a full hexagonal closed packed layer with αβ sequence while the aluminum sub-lattice forms a cubic close packed structure with the vacancies occupying alternating positions in the layered lattice with ABC sequence. A full period would be …AαBβCαAβBαCβ… as shown in Fig. 1.3.

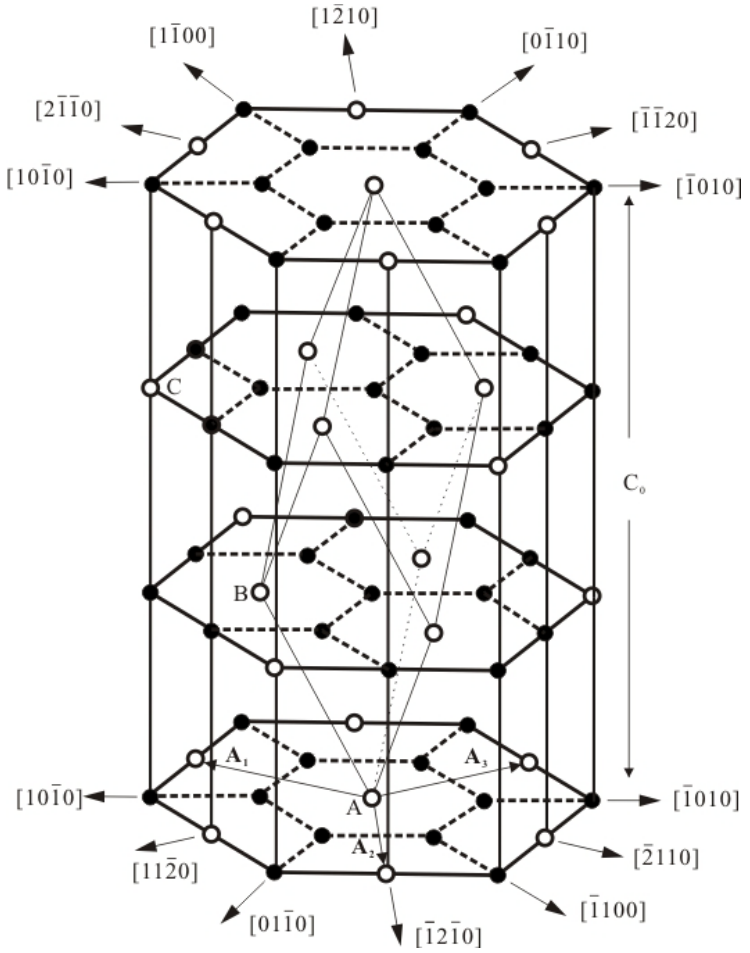

FIG. 1.3. The structure of Al_2O_3 layers showing the aluminum sublattice with vacancy occupying alternating positions. The oxygen sublattice is not shown.

The relative orientation of the GaN film on the c-plane sapphire has an in-plane rotation about 30° between each other. In this configuration, the lattice mismatch is $\frac{a_{epi}-a_{sub}}{a_{sub}}=\frac{\sqrt{3}\times 3.186-4.758}{4.758}=0.16$, which is quite large, and so the GaN epilayers are found to be under biaxial compressive strain.

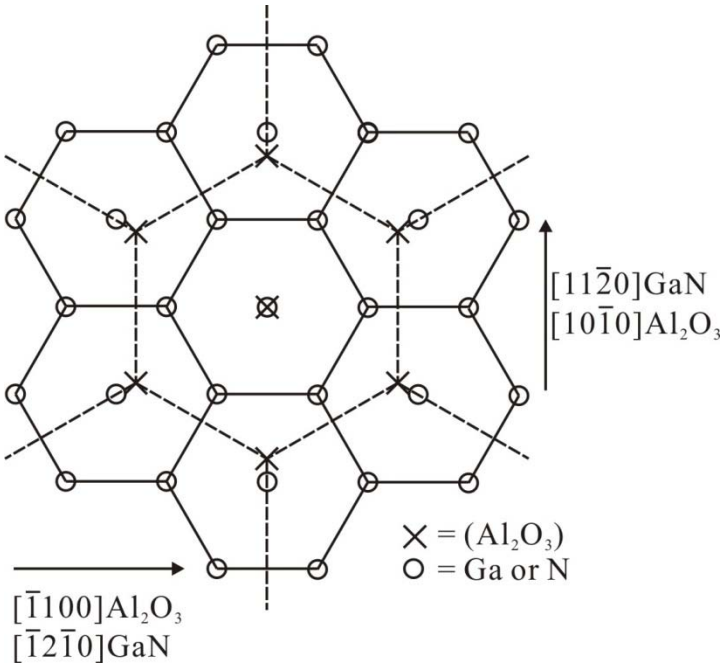

FIG. 1.4. c-plane (0001) GaN grown on *c*-plane (0001) sapphire showing the lattice mismatch.[26]

The large difference in the thermal expansion coefficients and large lattice mismatch produce a high density of dislocations. To overcome lattice mismatch, a buffer layer coupled with substrate nitridation were adopt to grow better quality films. Other available substitutes shown in table 1.2 such as Si, 6H-SiC, ZnO, $LiAlO_2$ and bulk GaN were also used to replace sapphire but with limited success.

Table 1.2.

Physical constants of common substrates used in III-nitride devices.[14]

Materials	Crystal Structure	Lattice Constants(Å)	Thermal expansion Coefficient ($\times 10^{-6}$)	Melting Point(°C)
GaN	Wurtzite	$a = 3.1184$ $c = 5.1852$	$\alpha_a = 5.59$ $\alpha_c = 3.17$	>2500
Sapphire	Rhombohedral	$a = 4.758$ $c = 12.991$	$\alpha_a = 7.5$ $\alpha_c = 8.5$	2300
6H-SiC	Wurtzite	$a = 3.081$ $c = 15.117$	$\alpha_a = 4.2$ $\alpha_c = 4.68$	2700 subl.
ZnO	Wurtzite	$a = 3.250$ $c = 5.207$	$\alpha_a = 6.5$ $\alpha_c = 3.7$	1975
GaAs	Zincblende	5.653	5.73	1240
$MgAl_2O_4$	Spinel	8.083	7.45	2130

1.4.2. INGAN/GAN LATTICE MISMATCH

The quantum well (QW) structure in the active region used in III-V nitrides devices is typically composed of one or multiple slabs of thin lower band gap InGaN film (usually ~ 2 nm) sandwiched between higher band gap GaN confinement (or barrier) layers. Higher indium incorporation is required in order to achieve longer wavelength emission. Whereas, the large lattice mismatch between GaN and InN (10.6%) is always present due to the size difference of In and Ga atoms. Increasing In concentration for longer wavelength emission (towards green and yellow) generates larger lattice mismatch strain at interfaces as compared to that for blue or violet emission, and consequently leads to more adverse effects, like a reduction of electron-hole wave function overlap due to tilt of QW band-edge, a larger band-edge potential fluctuation, and even the

breakdown of the InGaN films,[27] and strain-related compositional pulling effects[28] resulting in gradation in composition.

1.4.3. SPONTANEOUS AND PIEZOELECTRIC FIELDS

As mentioned before, the wurtzite structure can be decomposed into an assembly of imperfect tetrahedra. In each tetrahedron, the charge center of the cations (In, Ga, Al) has a small displacement along the c axis with respect to the effective charge center of the anions (N). Thus, net dipoles appear in each tetrahedral cell and collectively result in a macroscopic spontaneous polarization. The spontaneous polarization in GaN points towards the $[000\bar{1}]$ direction and has a strength of -0.029 C/m^2, as first calculated by Bernardini.[29]

Due to lack of center of symmetry, in-plane external strain introduces an additional internal displacement that adds to the overall dipole moment. This strain-induced polarization is called piezoelectric polarization.

1.4.4. DEFECTS

Another challenge in III-nitrides is the presence of high densities of extended defects, such as threading dislocation (TD) and planar stacking faults (SF). TDs form at the growth interface due to lattice mismatch and strain between the heteroepitaxial film and the underlying substrate. TD densities in c-plane GaN are typically ~10^8 to 10^{10} cm^{-2},[30] while this value goes up to ~ 10^{10} cm^{-2} for non-polar planar films.[31] Some techniques such as epitaxial lateral overgrowth (ELOG) have been adopted to obtain near dislocation-free films.[32]

1.4.5. INGAN INSTABILITY

Another challenging issue for growth of indium-rich InGaN devices emitting at longer wavelengths is compositional instability,[33] leading to phase separation and inhomogeneous compositional fluctuation. The calculated phase diagram for GaN and InN, shown in Fig. 1.5, indicates a miscibility gap at most compositions. The non-uniform distribution of composition due to immiscibility will lower the optical properties with a broader FWHM and reduced emission intensity.[34] On the other hand, it is believed that to some extent inhomogeneous compositional fluctuation acts like quantum-dot-like efficient radiative recombination centers,[35] which increases the efficiency by trapping carriers before they get captured by non-radiative recombination centers like dislocations.

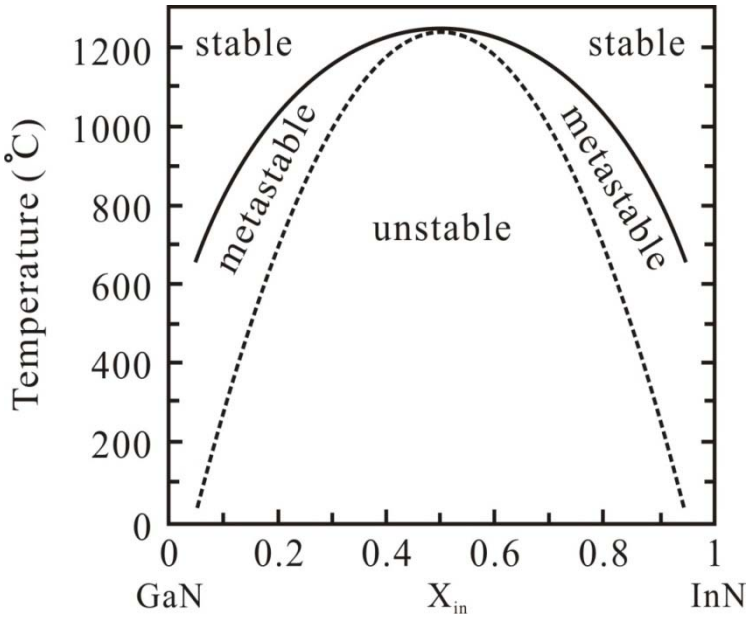

FIG. 1.5. Calculated phase diagram for binary alloys of GaN and InN, showing the binodal (solid), spinodal (dashed) curves, and the critical temperature (~1250°C)[34]. Stable, metastable, and unstable regions are shown.

1.5. ORGANIZATION OF THIS DISSERTATION

This dissertation consist a comprehensive study of optical and microstructural study of laser and light-emitting diodes of InGaN/GaN materials.

Chapter 2 is an introduction to the catholuminescence techniques used in this dissertation. Chapter 3 presents the optical and electrical properties of laser diode structures grown on c-plane sapphire and GaN bulk substrates. Chapter 4 presents the luminescence and microstructural characterization of non-polar m-plane InGaN thick films with different compositions grown on m-plane GaN bulk substrates. Chapter 5 presents the effect of misfit dislocations in luminescence on m-plane InGaN quantum wells.

Chapter 6 presents structural, luminescence, and compositional analysis on quaternary alloy InAlGaN thick films. Finally, Chapter 7 summarizes the relevance of this work and suggests future research directions.

CHAPTER 2

CATHODOLUMINESCENCE TECHNIQUES

2.1. INTRODUCTION TO CATHODOLUMINESCENCE

Cathodoluminescence (CL) is the generation of light that results from electron irradiation. When an electron beam impacts a semiconductor, energy is transferred to the solid, promoting some valence electrons to the conduction band. This generates electron-hole pairs as well as lattice vibrations, x-rays, etc. These electron-hole pairs recombine and emit photons with energy approximately equal to the band gap. The luminescence can be divided into two types.[36] (a) intrinsic, due to electron-hole pair recombination that involves a transition of an electron from the conduction band to the valence band, and, (b) extrinsic, due to carrier recombination via impurity states within the band gap (e.g. donor-, acceptor-bound excitons, donor-acceptor pairs, deep level traps, etc.).

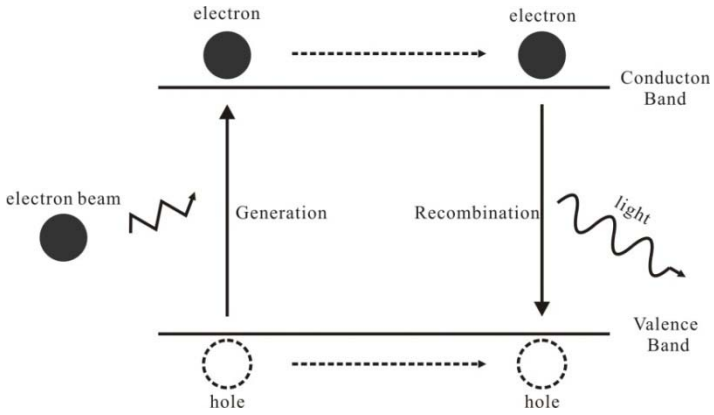

FIG. 2.1. An electron beam incident on a semiconductor generates electron and hole pairs, and their recombination generates a photon with an energy close to the band gap.

Fig. 2.1 is an illustration of the generation of a photon in a semiconductor after electron beam irradiation. There are other ways to achieve the initial excitation besides an electron beam. The convenient classification of photon generation is by the excitation source, e.g, photoluminescence (PL) uses a laser beam as the excitation source, electroluminescence (EL) uses electric fields, etc.

2.2. CHARACTERIZING LIGHT-EMITTING SEMICONDUCTORS BY CATHODOLUMINESCE IN A SCANNING ELECTRON MICROSCOPE

Commonly, CL spectrometers are attached to scanning electron microscopes (SEM) to achieve versatile characterization capabilities. The high spatial resolution in the SEM enables light emission characterization from regions as small as tens of nanometers, up to the millimeter scale, which makes CL suitable for analyzing luminescent details related to fine microstructure features as well as looking at large area emission representing bulk properties.

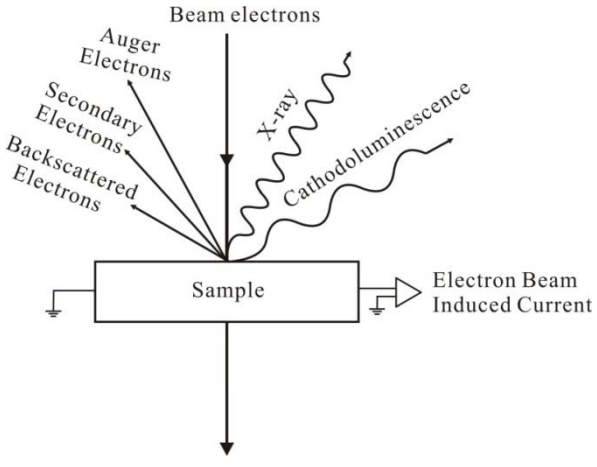

FIG. 2.2. Schematic illustration of interaction characteristics from electron beam irradiation.

Another advantage of CL is that the beam energy in a conventional SEM can be adjusted from approximately 1 to 30 keV, which is suitable for analyzing multilayer structures. Increasing the beam energy can increase the interaction range in the sample and generate electron-hole pairs deeper in the film. A number of elastic and inelastic processes are induced by the electron beam in the SEM, as shown in Fig. 2.2. Absorption of electron beam energy generates electron-hole pairs, as mentioned previously, and also electron beam induced currents (EBIC). High energy absorption leads to X-ray and Auger electron emission. Backscattered electrons (BSE) are primary electrons reflected or backscattered out of the specimen by elastic scattering interactions with the specimen atoms. They typically originate from within 1μm of the sample surface with energies close to that of the incident beam. BSE can provide atomic number contrast, since heavy elements (high atomic number) backscatter electrons more intensely than light elements (low atomic number). Thus, brighter contrast would appear in the image for regions with heavier elements, which is suitable for compositional uniformity analysis.[37] Electrons originating from inelastic scattering are called secondary electrons. These are typically defined by having energies less than 50 eV, and are produced by collisions with the atomic nuclei where significant energy loss occurs or by the ejection of loosely bound electrons from the sample atoms. Since most secondary electrons originate within 50 Å of the specimen surface, they provide topographical contrast with high spatial resolution and depth of field, and can be affected by local electric and magnetic fields.

2.3. INTERACTION OF BEAM ELECTRONS WITH SOLIDS

For CL analysis, it is important to understand the interaction of the electron beam and the specimen. In particular, we need to understand the beam penetration into the specimen as a function of the accelerating voltage. The penetration depth of the electron beam can be analyzed and modeled considering the energy lost during the beam-sample interaction processes.[38-43] The scattering mechanism of the electron beam inside the sample can be divided into elastic and inelastic scattering. Elastic collision with the atomic nuclei can be analyzed using the Rutherford scattering method, whose total cross section σ is given by the formula,[36]

$$\sigma = (5.21\times10^{-21})(\frac{Z}{E})^2 \frac{4\pi}{\delta(\delta+1)}(\frac{E+m_0c^2}{E+2m_0c^2})^2,$$

where Z is the atomic number of the scattering atoms, E is the energy of the electrons in keV, and δ is the screening parameter.

The generation of light in CL is accomplished by inelastic collisions which are described by the Bethe expression for the mean rate of energy loss per segment of distance S that e^- travels in the solid, and has the following form[36]:

$$\frac{dE}{dS} = -2\pi e^4 N_A \frac{\rho Z}{EA}\ln(\frac{1.166E}{J}),$$

where e is the electron charge, N_A is Avogadro's number, Z, ρ, and A are the atomic number, the density, and the atomic weight of the solid, respectively. E is the mean primary electron energy and J is the ionization potential. The Bethe range is defined as the length of a single electron following a random trajectory,

$$R_e = \int_0^{\infty} \frac{1}{(\frac{dE}{dS})} dE \,.$$

The interaction volume derived from the Bethe model is an overestimate since it does not consider elastic scattering effects.

2.3.1. ELECTRON BEAM PENETRATION RANGE

The size of the interaction volume is measured from the surface to the depth where electrons stop and is usually characterized by what is called the electron beam penetration range. An illustration of the interaction volume is shown in Fig. 2.3. Many empirical expressions for the electron beam penetration in solids are available; most of them have the form of the Gruen range,[36] given by,

$$R_e = \frac{k}{\rho} E_b^{\alpha} \,,$$

where k is related to the atomic number of the probed material and a function of energy, α depends on the beam energy and atomic number. Everhart and Hoff modeled and estimated the electron penetration depth:[42]

$$R_e = (\frac{0.0398}{\rho}) E_b^{1.75} (\mu m) \,,$$

where E_b is in keV and ρ is in g/cm^3. This result was relatively accurate with a primary electron beam energy of 5 to 25 keV and atomic numbers $10<Z<15$.

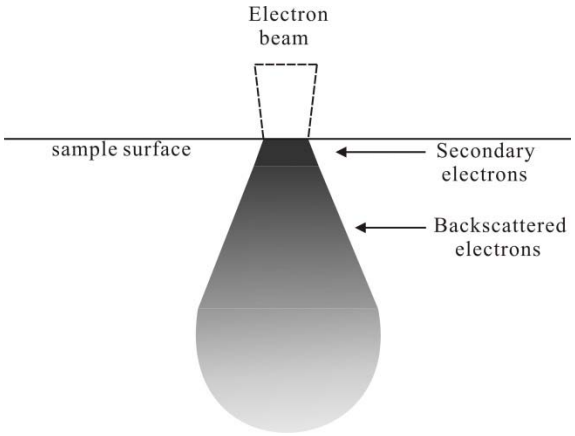

FIG. 2.3. Interaction volume generated by electron bombardment. The approximate range of the secondary and backscattered electrons signals are indicated.

Kanaya and Okayama suggest a more general expression which agrees well with a wider range of atomic numbers,[43]

$$R_e = (\frac{0.0276A}{\rho Z^{0.889}}) E_b^{1.67} (\mu m) ,$$

where A is the atomic weight in g/mol, ρ is in g/cm^3, Z is the atomic number, and E_b is in keV.

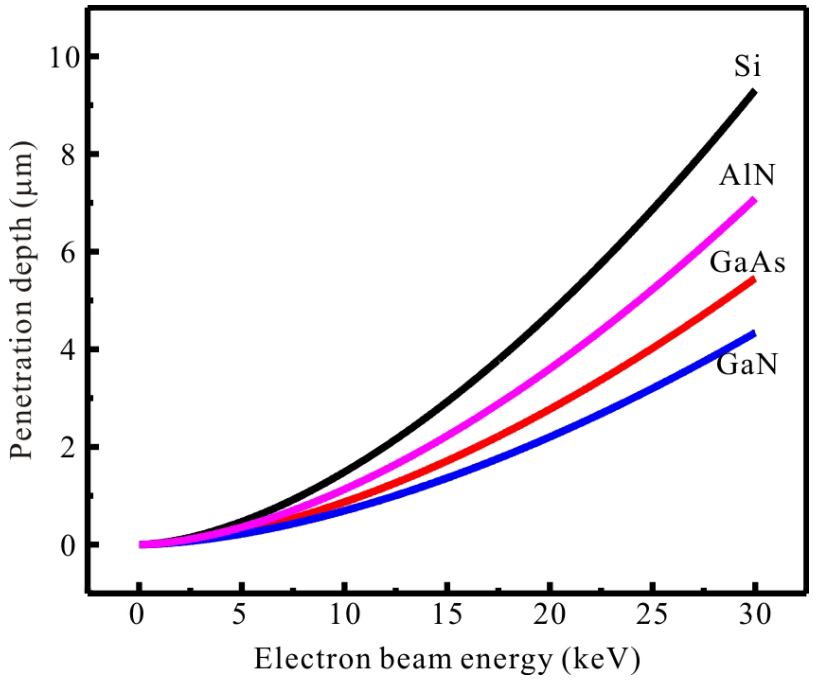

FIG. 2.4. Penetration depth plot for various materials based on the Kanaya and Okayama model.

A plot of the Kanaya and Okayama model for some semiconductor materials is shown in Fig. 2.4.

2.3.2. GENERATION OF ELECTRON AND HOLE PAIRS

In order to have some knowledge about the generation of electron and hole pairs inside the interaction volume excited by the primary electron beam, the generation factor (the number of electron-hole pairs generated per beam electron) is given by

$$G = E_b(1-\gamma)/E_i,$$

where γ represents the fraction of electrons that undergo backscattering. E_i is the ionization energy, which is related to the band gap as $E_i = 2.8E_g + M$, where M is within the range from 0 to 1eV, depending on the material.

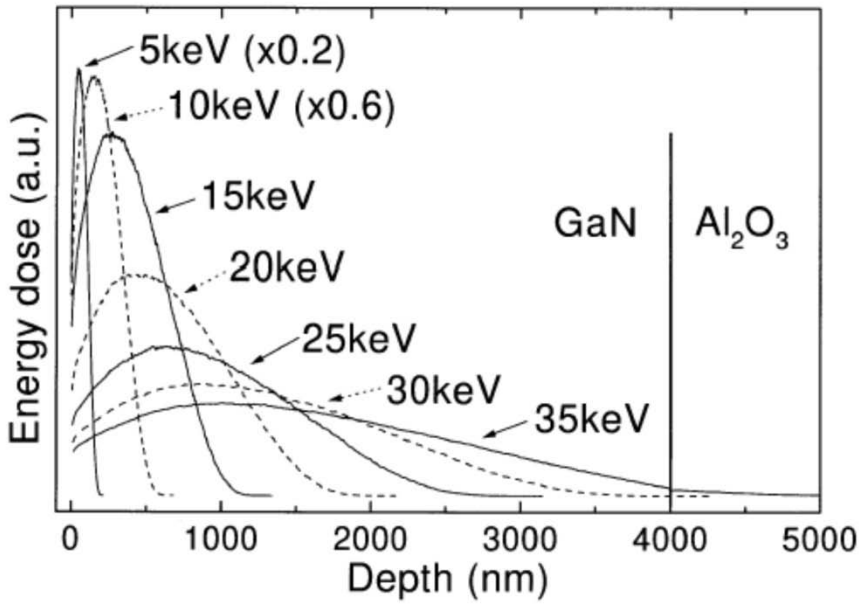

FIG. 2.5. Simulated differential energy loss versus depth for a 4μm-thick GaN on sapphire under different electron-beam accelerating voltages.[44]

For typical conditions, the generation of electron and hole pairs during CL has a range of 10^9 to 10^{12} cm^{-3}. A typical energy loss versus penetration depth for different electron beam energies is shown in Fig. 2.5.

2.4. SETUP OF A CATHODOLUMINESCENCE SYSTEM

The actual CL system used in this dissertation consists of 4 main parts: (1) SEM, (2) parabolic mirror, (3) spectrometer, and (4) photon detector, which in our case is a photomultiplier tube (PMT). The SEM is a JEOL 6300 equipped with a LaB_6 thermionic electron gun. The electron beam tilt and shift can be controlled by the condenser lenses.

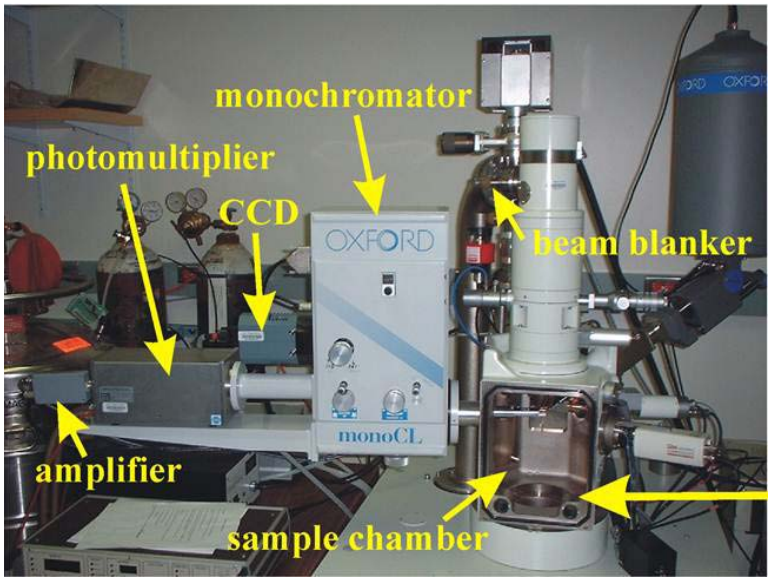

Fig. 2.6. Image of the CL setup used in this dissertation showing the sample chamber, beam blanker, monochromator, CCD camera, photomultiplier, and amplifier.

The electron beam can be focused to a diameter of ~ 4 nm using the condenser lens, objective lens, and an objective aperture. CL measurements are realized by additional equipment attached to the left of the SEM column as shown in Fig. 2.6. We use a commercial CL unit, the MonoCL2, manufactured by Gatan. A movable, parabolic mirror is placed over the specimen to collect light for CL measurements. The mirror contains a pinhole in the center which allows the electron beam probe to pass through. The light emitted from the specimen is focused by the parabolic mirror into a light pipe when the specimen position is adjusted to the focal point of the mirror. The light is transmitted through a slit into the monochromator via a quartz window.

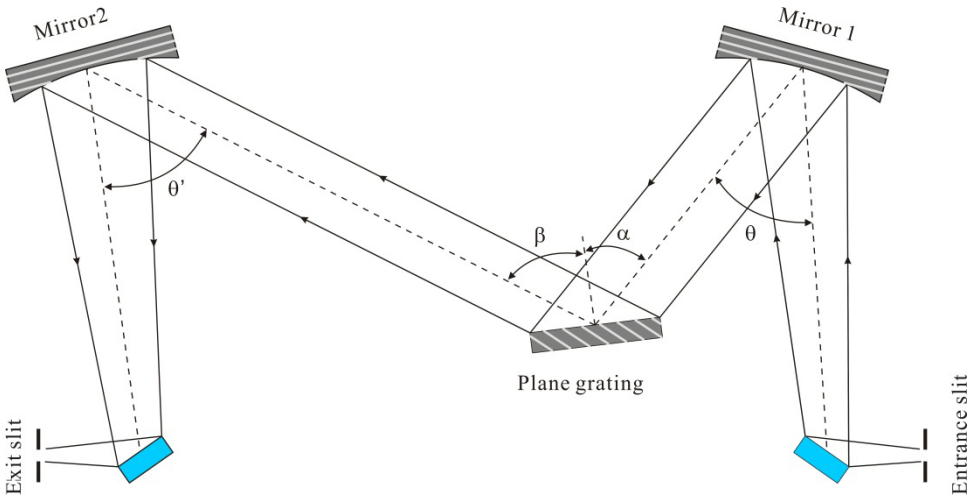

FIG. 2.7. Schematic of Czerny-Turner configuration showing the grating mechanism that sends a selected wavelength to the exit slit. *α, β* are angles of the incident and diffracted light ray with respect to the grating normal.

Fig. 2.7 is the illustration of the spectrometer used with a Czerny-Turner grating configuration. After being collimated by a silver coated mirror (Mirror 1), the light is directed to the diffraction grating where it is dispersed. By rotating the grating with a motor, a specific wavelength light is sent to the silver coated mirror (Mirror 2); it gets focused and exits the spectrometer through a second slit. The expression for diffraction of light of wavelength λ through a grating with a groove spacing d is given by

$$d(\sin\alpha - \sin\beta) = n\lambda ,$$

where α and β are the angles of the incident and diffracted rays with respect to grating normal. Inside the spectrometer, the position of the entrance slit and the exit slit are fixed and the grating rotates to scan different wavelengths. A constant-deviation monochromator mount is used so that the λ changes when rotating the grating, with the light path unchanged. Thus, the deviation angle $2K = \alpha + \beta$ remain constant for certain spectrometer, while the scan angle, $\phi = \frac{\alpha - \beta}{2}$, varies with λ, as we rearrange the grating equation mentioned above,

$$2\cos K \sin\phi = Gn\lambda ,$$

which shows that the selected wavelength is directly related to the sine of the scan angle. $G = 1/d$ is the groove density. The grating in our spectrometer has a groove density of 1200 lines/ mm with a blaze wavelength of 250 nm and a dispersion of 2.7 nm/mm. From the exit slit, the light enters PMT detector. A PMT consists of multiple vacuum tube electrode which emits two or more electrons for each electron striking it, amplifying the signal. For one photon that strikes the

photocathode, 10^6 electrons are typically emitted and collected by the anode, and subsequently analyzed.

2.5. TIME-RESOLVED CATHODOLUMINESCENCE

Time-resolved cathodoluminescence (TRCL) is used to study carrier recombination dynamics by analyzing the light output rise and decay in the sampled semiconductor. A decay lifetime obtained by TRCL is a measure of several recombination processes in the material that include radiative and non-radiative channels.

2.5.1. RADIATIVE AND NON-RADIATIVE RECOMBINATIONS

There are two types of carrier recombination processes in semiconductors: radiative and non-radiative. Radiative recombination is electron-hole pair recombination that results in the emission of a photon. This includes band-to-band transitions, excitonic transitions, and impurity-related emissions. Non-radiative recombination, on the contrary, is the recombination with no light emission. Examples of non-radiative recombination are surface recombination and Auger recombination. Structural defects typically provide non-radiative recombination channels.

The total recombination rate R is inversely proportional to the physically observable lifetime τ, and is the summation of the radiative and non-radiative recombination rates. It can be expressed by the following equation:

$$R = R_{rr} + R_{nr} = \frac{1}{\tau_{rr}} + \frac{1}{\tau_{nr}} = \frac{1}{\tau},$$

where R_{rr} and R_{nr} represent radiative and non-radiative recombination rates, while τ_{rr} and τ_{nr} denote their corresponding lifetimes, respectively. Normally, the radiative and non-radiative lifetimes are inferred from the observable total lifetime τ, and the internal quantum efficiency (IQE), η, by the following relation:

$$\eta = \frac{I(T)}{I(0K)} = \frac{R_{rr}}{R} = \frac{1}{1+\tau_{rr}/\tau_{nr}}.$$

In order to increase IQE, nonradiative recombination needs to be passivated. Theoretically, 100% IQE can be achieved if there are no non-radiative recombination channels involved.

2.5.2. TIME-RESOLVED CATHODOLUMINESCENCE SETUP

To perform time-resolved CL measurements, additional equipment is required and we will discuss it below. In order to achieveTRCL, a pulsed electron beam is required to excite the specimen for fixed intervals of time. The light output decay after excitation can be studied and the lifetime can be extracted. The beam blanker consists of two parallel plates and is located right below the gun area. The pulsed condition is obtained by charging the plates which deflect the electron beam. The frequency range in our system is available from 1 kHz to 1 MHz. A time-correlated single photon counting (TCSPC)[45] is adopted in photon detection, which measures the time from when the pulse is generated to when the first photon is detected. This time length is assigned to a voltage height by a time-to-amplitude converter (TAC). Over many iterations of this process a build-up of intensities versus time channels has been recorded. This is called the transient. An illustration of a typical transient is shown in Fig. 2.8. When the electron beam is

switched on, the luminescence intensity starts to build up (onset), and then saturates (steady state). After the beam is switched off, the luminescence intensity starts to decay with time.

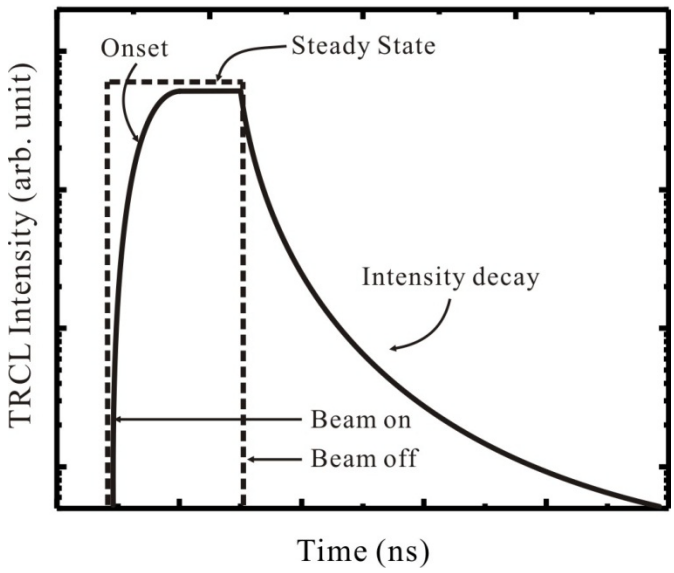

FIG. 2.8. Schematic of the TRCL transient showing the onset, steady state, and the intensity decay.

Luminescence decay versus time is often modeled with an exponential form:

$$I(t) = I_0 \exp^{-\frac{t}{\tau}},$$

where I_0 represents the intensity when the beam is initially switched off, τ represents the lifetime.

CHAPTER 3

OPTIMIZATION OF *C*-PLANE INDIUM GALLIUM NITRIDE-BASED LIGHT-EMITTING STRUCTURE

3.1. INTRODUCTION TO INDIUM GALLIUM NITRIDE EMITTING DEVICES

Group III-nitride semiconductors have attracted much attention for applications into high-brightness light emitting diodes (LEDs) and laser diodes (LDs) in the visible and ultra-violet spectral range. For example, LDs are used for optical storage (Blu-ray DVD) and laser pointers, while LEDs can be used for solid state lighting, back-light display, and medical applications. However, in order to produce high brightness GaN-based LEDs and LDs, there are several issues that need to be considered especially for green light, where InGaN epilayers are used in the active region. The lack of suitable substrate leads to high defect densities in the epilayers. Heteroepitaxy in the InGaN system typically involves significant compositional changes that lead to large lattice mismatch, with a maximum value of above 10% for InN and GaN. In addition, the absence of a center of symmetry in the wurtzite structure, leads to strong spontaneous and piezoelectric fields. A strong internal field will cause spatial separation of the electron and hole wave functions, causing lower recombination efficiencies. This situation worsens towards the green regime which requires higher indium compositions. Also, $In_xGa_{1-x}N$-based quantum wells with high indium content are difficult to grow due to differences in the thermodynamic properties of GaN and

InN which cause inefficiency in indium incorporation, indium inhomogeneity,[46] and/or phase separation.[47,48] The high growth temperatures for p-GaN and post-growth thermal annealing to remove hydrogen passivation effects and to improve p-type conductivity[49,50] have shown to deteriorate the quantum well crystalline quality by segregation of indium inside the quantum wells.[51] There is a tradeoff between good p-type conducting and good quality of active region. Additionally, a good design of the electron blocking layer (EBL)[52-54] is also vital for hole transport. In this chapter, the design of the laser diodes has been varied in order to optimize the layer structure for green laser diodes. We have studied the optical and structural properties of several GaN based laser diodes and light-emitting diodes.

3.2. THE EFFECT OF SUBSTRATES AND P-DOPING LEVELS ON PERFORMANCE OF LASER DIODE STRUCTURES

In this section, laser diode (LD) structures grown on sapphire and bulk GaN with different Mg-doping levels in the p-region are studied in order to investigate the effect of these factors on the LD performances. The samples described in Fig. 3.1, were grown by metal-organic chemical vapor deposition (MOCVD) by the group of Prof. Russell Dupuis at Georgia Institute of Technology. The LD structures include n-type GaN layers grown on a ***c***-plane sapphire and on bulk GaN substrates; n-type cladding layers with 150 periods of $Al_{0.16}Ga_{0.84}N$/GaN (2.5nm/2.5nm) were grown on the former layers followed by a 100 nm thick n-GaN waveguide laye; $In_{0.1}Ga_{0.9}N$ quantum wells were grown at

750^{o}C, separated by undoped GaN QW barrier, with thickness of 3.5 nm and 8.8 nm, respectively. In order to complete the LD structure, p-type layers were grown in the following sequence, a 20 nm Mg-doped $Al_{0.18}Ga_{0.83}N$ electron blocking layer, a 100-nm p-GaN waveguide, a 90-period $Al_{0.17}Ga_{0.83}N$/GaN (2.4nm/2.4nm) p-cladding layer, 30 nm p-GaN hole injection layer and 20 nm p-GaN contact layer. We will refer to samples grown on sapphire as A and C while samples grown on bulk GaN as B and D. Samples A and B contain 4 QWs while samples C and D contain 3. Samples C and D have a Cp_2Mg flow reduced ~ 28% for p-cladding layer and ~50% for the EBL compared to samples A and B. The purpose of this experiment is to compare the effect of different substrates and doping on their optical, structural and electrical properties.

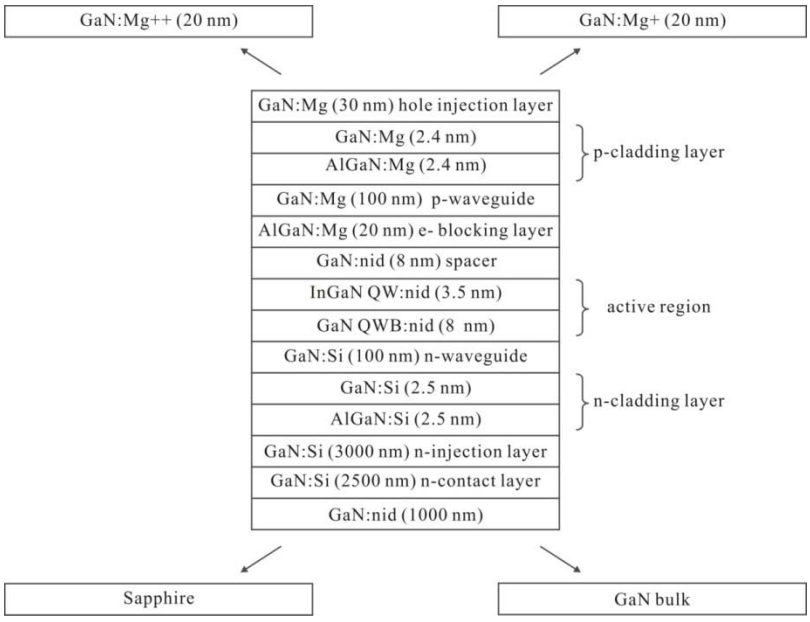

FIG. 3.1. Layers of the LD structure with different substrate and p-contact layer.

Sample A and C use sapphire as substrates while sample B and D adopt bulk GaN as substrates. For sample C and D, the magnesium flow was reduced for the p-contact layer.

3.2.1. MICROSTRUCTURAL CHARACTERIZATION OF VIOLET LASER DIODE STRUCTURES USING TRANSMISSION ELECTRON MICROSCOPY

Cross-section TEM was performed by Mr. Kewei Sun using standard mechanical polishing and argon ion milling techniques. The microstructures of the blue laser diode samples are shown in Fig. 3.2. As we can observe all samples exhibits good contrast and sharp interfaces in the quantum well, EBL, and p- and n-superlattice regions. No threading dislocations are observed in the active region.

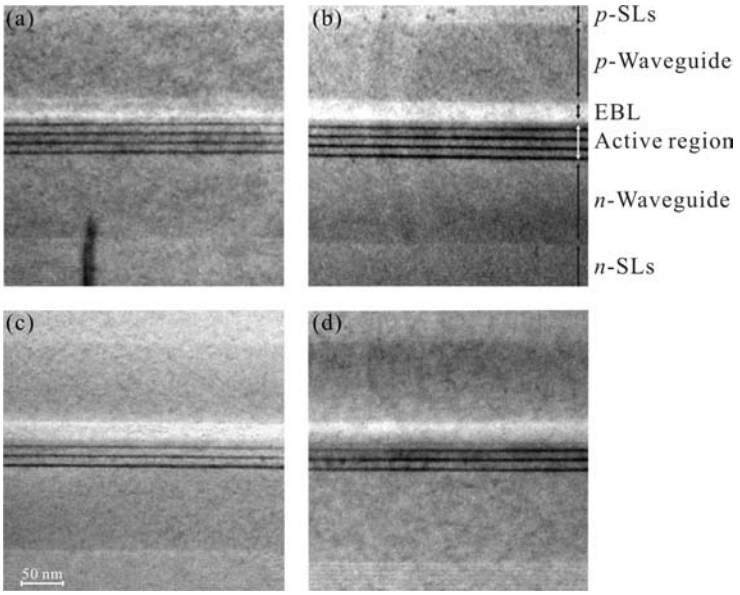

FIG. 3.2. Cross section TEM image of four blue LD structure samples (a) A, (b) B, (c) C, and (d) D showing that p-type layer crystalline quality improves via reducing the Cp_2Mg flow in p-cladding layer and EBL.

The EBL in sample A is not very uniform, and appears to consist of two layers. The upper layer has darker contrast than the bottom layer corresponding to lower aluminum incorporation. By decreasing Cp_2Mg flow in the p-cladding layer and in the EBL, Mg-related precipitates are greatly reduced as shown in samples C and D. Fig. 3.3 shows magnified high-resolution TEM images of the quantum well region. The bottom quantum wells are thicker than the subsequent wells for samples A, B, and C. The quantum well thickness in sample D is quite uniform. Thickness variations in the quantum well region could affect the internal field and thus the quantum confined energy of electron and hole pairs. The choice of substrate does not seem to affect the QW quality.

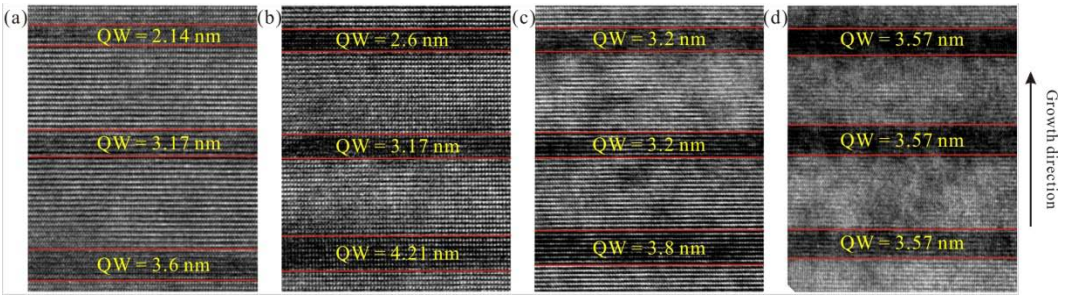

FIG. 3.3. High-resolution TEM images of the QW regions for (a) A, (b) B, (c) C, (d) D. Sample D shows uniform thickness in QWs while other samples exhibit thickness variations.

3.2.2. OPTICAL CHARACTERIZATION OF VIOLET LASER DIODE STRUCTURES VIA CATHODOLUMINESCENCE

In order to analyze the luminescence in the complex multi-junction structure, depth-resolved CL was performed on these four blue LD structures using different accelerating voltages from 5 kV to 20 kV with a fixed beam current at 400 pA. Fig. 3.4 (a) shows: p-AlGaN/GaN superlattice mini-band transition (at $\sim$ 350 nm), p-GaN acceptor bound exciton transition (AX_2 at $\sim$ 365 nm), donor-acceptor pair recombination (DAP at $\sim$ 380 nm) in all four samples taken at 300 K and at low accelerating voltage (5 kV). Samples A and B exhibit stronger donor-acceptor pair luminescence but weaker superlattice transition than samples C and D. The former may be due to excessive magnesium incorporation in the p-region, whereas the latter may be due to poor crystalline quality of the superlattice. The increase of donor-acceptor pair recombinations (see DAP broadening in Fig. 3.4 a) is related to the increase of the magnesium concentration which creates acceptor bands ready for additional transition. When we increase the accelerating voltage to 15 and 20 kV as shown in Fig 3.4 (c) and (d), yellow luminescence was observed and attributed to gallium vacancies in the n-GaN layer. All QW emissions start to merge at an accelerating voltage of 15 kV except for sample D as shown in Fig 3.4 (c). At these accelerating voltages band-to-band transitions appear, which means that the primary electron beam has reached n-type region of the LD structure.

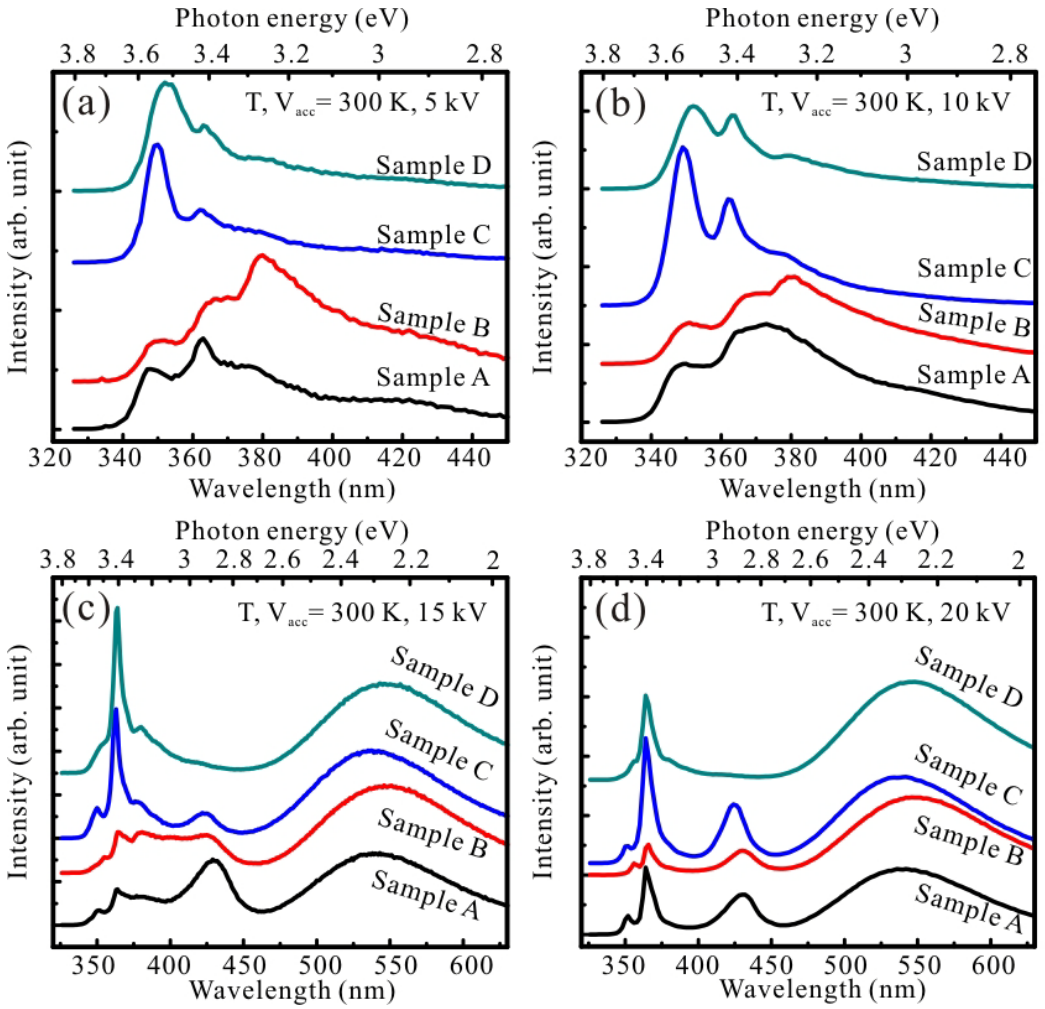

FIG. 3.4. Depth-resolved CL spectra of samples A, B, C, D with different accelerating voltage (a) 5 kV, (b) 10 kV, (c) 15 kV and (d) 20 kV. The spectra were taken at 300 K.

Fig 3.4 (d) with a 20 kV accelerating voltage exhibits the superlattice miniband transition, GaN band edge emission, and yellow luminescence have the same corresponding wavelengths for samples A and C, and samples B and D, respectively. Since samples A and C have been grown on sapphire, we suggest that the blue-shift of samples A and C with respect to samples B and D may be

due to the thermal strain generated by the sapphire substrates. Compressive strain, exerted on GaN underlayer, will compress the basal lattice constants increase the band gap. This strain-induced wavelength shift is a bulk effect which is different from the strain induced QCSE effect, as a consequence, all peaks shift similarly.

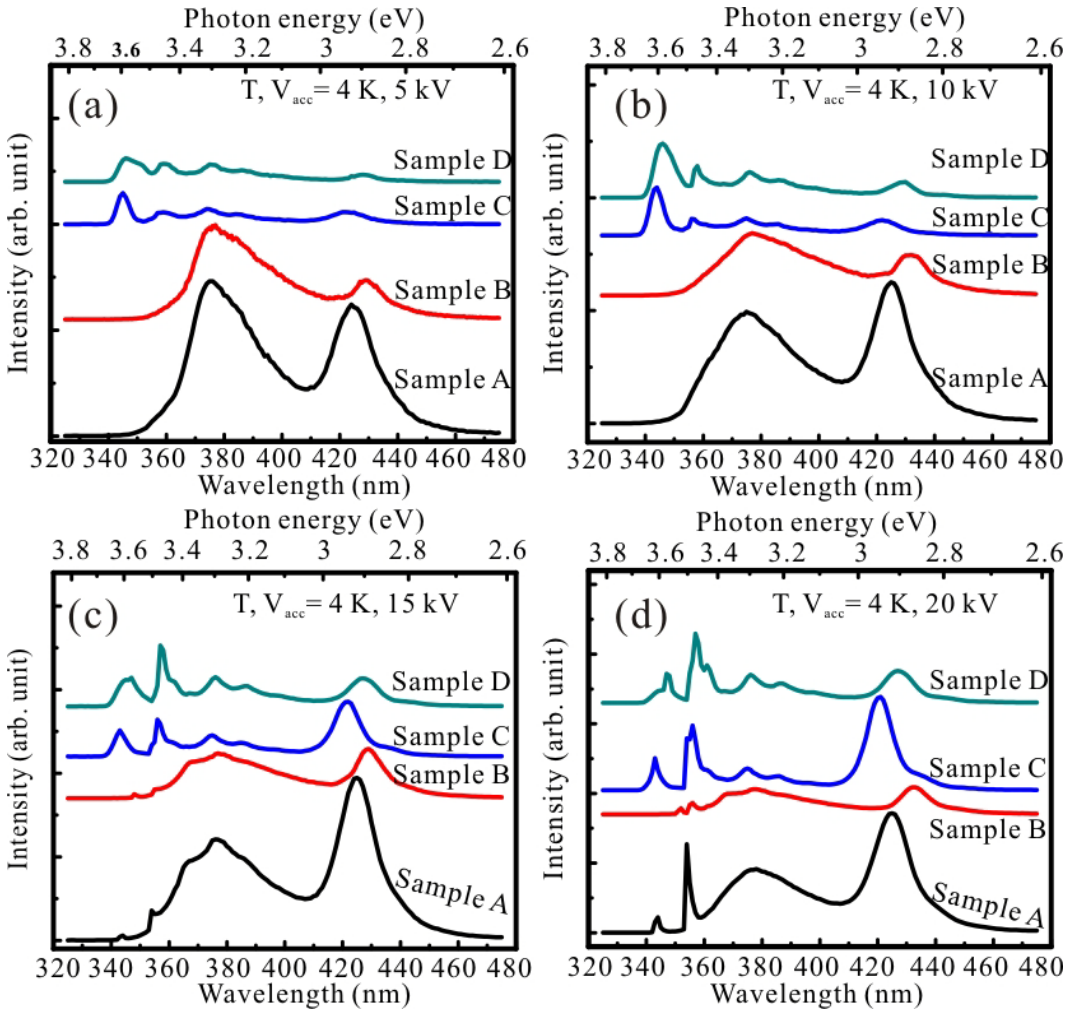

FIG. 3.5. Depth-resolved CL spectra of samples A, B, C, D, taken at 4 K with accelerating voltages of (a) 5 kV, (b) 10 kV, (c) 15 kV and (d) 20 kV.

CL spectra taken at low temperature shown in Fig. 3.5, We observe that the QW emission is blue-shifted in samples A and C compared to B and D. This

could be due to the fact that the substrate makes it harder for indium to incorporate in the QWs, thus samples A and C have less indium concentrations and also non-uniform thicknesses in the QWs. Although the QW intensity in sample A is much stronger than sample B, lasing was realized on sample B (not shown here). CL is related to optical properties, which could be affected by microstructure. For example, defects such as non-radiative recombination centers will reduce efficiency; and compositional inhomogeneity will broaden the peak. But CL cannot reveal electronic properties such as p-conductivity which could be crucial to the electronically pumped devices. Fig. 3.6 shows the time-resolved CL spectra of the QW emission for sample C and D at 4 K. Due to the non-exponential decay behavior of the time evolution curves, we estimate the lifetime as when the intensity decreases from a maximum to 1/e of its value. The CL effective lifetime obtained from sample C is 130 ns, and from sample D it is 98 ns. The strain induced by the sapphire substrate may increase the piezoelectric field, lowering the overlap between electrons and holes, thus decreasing the recombination rate.

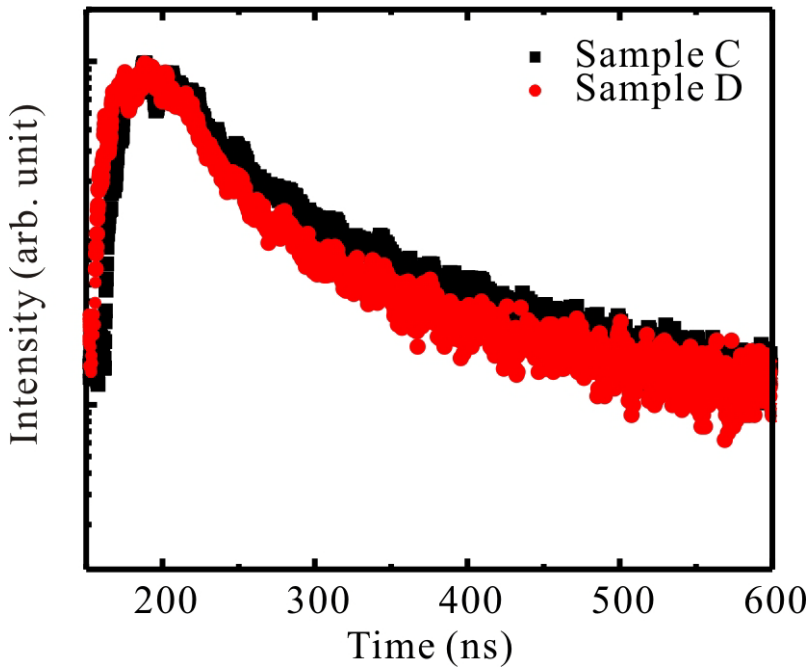

FIG. 3.6. Time-resolved CL transients for sample C and D at 4 K showing that sample D has a relative faster decay time.

3.3. THE EFFECT OF InGaN WAVEGUIDE ON PERFORMANCE OF BLUE-GREEN LASER DIODE STRUCTURES

Two of the blue-green LD structures, described in Fig. 3.7, were grown by low pressure metal-organic chemical vapor deposition (MOCVD) using a Thomas Swan reactor system, at Georgia Institute of Technology. These LD structures consist of two GaN layers grown on ***c***-plane sapphire or bulk GaN substrate. Subsequently, n-type cladding layers with 150 periods of $Al_{0.16}Ga_{0.84}N$/GaN (2.4nm/2.4nm) were grown on the former layers followed by a 100 nm n-GaN waveguide. Then, two $In_{0.18}Ga_{0.82}N$ QWs were grown at 750^{o}C, separated by a silicon–doped GaN QW barrier, with a thickness of 2.8 nm and 8.8 nm, respectively. In order to complete the structure, p-type layers were grown

sequentially: a 20 nm Mg-doped $Al_{0.18}Ga_{0.83}N$ electron blocking layer, a 100 nm p-GaN waveguide, a $Al_{0.17}Ga_{0.83}N$/GaN (2.4nm/2.4nm) p-cladding layer, a 30 nm p-GaN hole injection layer, and a 20 nm p-GaN contact layer. Two 80 nm undoped InGaN were inserted waveguides on both p-side and n-side of one of the LD structure and will be referred as sample F. The other sample without InGaN waveguides will be labeled as sample E. Silicon doping in the active region has several benefits. It enhances carrier injection by providing more free carriers;[55] Si doping can help change the dislocation density by reducing or suppressing the propagation of dislocations, and, it may also help relax compressive strains in the QWs.[56]

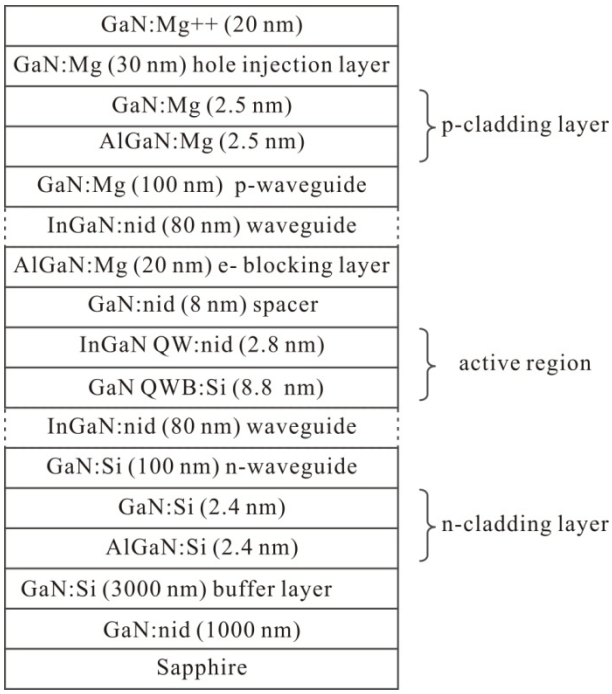

FIG. 3.7. Blue-green LD structure showing the layer sequence of p-contact layers, p-cladding layers, electron-blocking layer, active region, n-cladding layer, and GaN buffer layer grown on sapphire.

3.3.1. MICROSTRUCTURAL CHARATERIZATION OF BLUE-GREEN LASER DIODE STRUCTURES

Cross-section TEM was performed by Mr. Kewei Sun using standard mechanical polishing and argon ion milling techniques. The microstructures of green laser diodes E and F are shown in Fig. 3.8. As we can observe both samples exhibits good quantum well, EBL, p- and n-superlattice contrasts. The dislocation density in sample E and F is 2×10^{9} cm^{-2}, and 5×10^{8} cm^{-2}, respectively. Non-uniform strain fields can be observed in QW regions in sample E while uniform contrast can be observed in the structure of sample F.

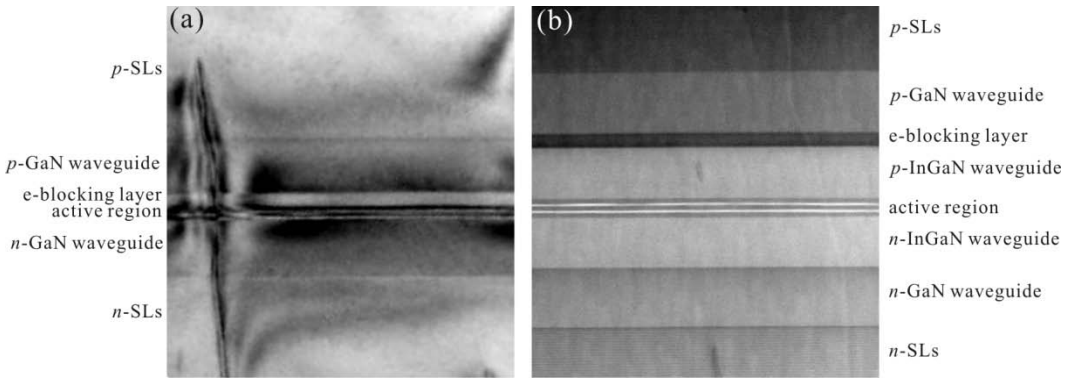

FIG. 3.8. (a) Cross section TEM image of sample E. (b) Dark field (DF) STEM image showing the additional *p, n* - InGaN waveguides surrounding the active region in sample F.

3.3.2. OPTICAL CHARACTERIZATION OF BLUE-GREEN LASER DIODE STRUCTURES

Depth-resolved CL was performed on these green laser diodes in order to distinguish the luminescence properties from different quantum wells (shown in Fig. 3.9). The electron beam currents were fixed at 0.4 nA. For sample E, with accelerating voltage lower than 11 kV, only one asymmetrical QW emission can be observed centered at 482 nm. When the beam accelerating voltage is increased above 15 kV, another shorter wavelength peak centered at 475 nm could be resolved and becomes dominant. We suggest that these double emission result from the two quantum wells. The top QW emits at longer wavelength (482 nm) since we use lower accelerating voltage at first (8 kV) while the bottom QW luminescence at shorter wavelength (475 nm). However, for sample F, nearly no variation in QW emission wavelength occurred when increasing the accelerating voltage. The presence of waveguide surrounding the active region may

homogenize the indium incorporation due to reduced strain in the QWs and thus improving the stability of the QW emissions.

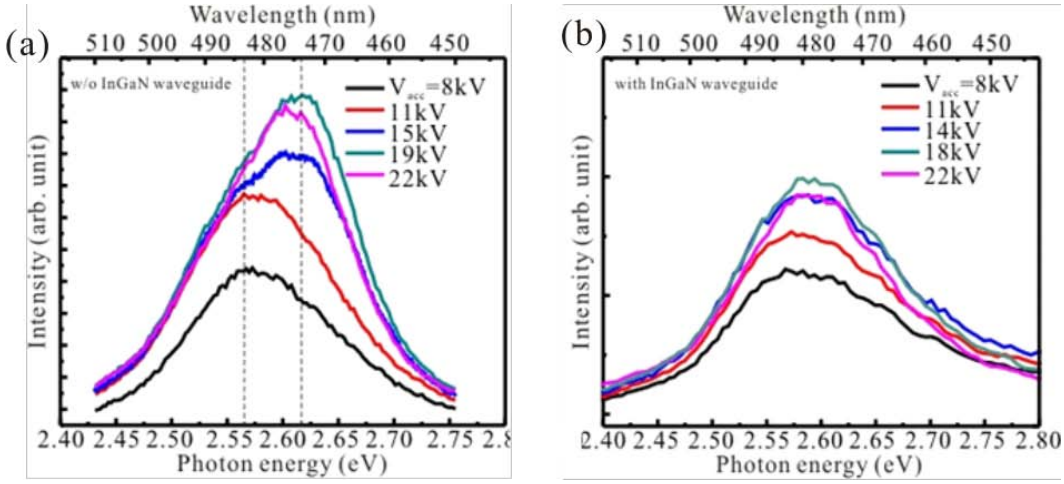

FIG. 3.9. Depth-resolved CL spectra on sample (a) E, (b) F with different accelerating voltages.

Since the QW emissions for these samples are asymmetrical, we fit them with two Gaussian curves as shown in Fig. 3.10. The Gaussian curve with red solid line and that with blue solid line are labeled, peak *A* and peak *B*, respectively. For sample E, at low accelerating voltage (8-11 kV), peak *A* centered at ~2.57 eV is much stronger intensities than peak *B* centered at ~2.65 eV. This implies peak *A* is probably from the top QW while peak *B* is from the bottom QW since low accelerating voltage (8-11 kV) is not sufficient to excite all the active region and the top QW would trap more diffusive carriers thus have higher intensities. When accelerating voltage is increased to 15 kV and higher, peak *B* dominates the total emission instead of peak A. Secondary carrier yield is nearly the same between QWs since the QW located deep inside the LD structure plus the separation between QWs is only a few nanometers considering the energy loss curve is

almost flat in that region. If there is only electron-hole pair generation solely caused by energy dose without considering diffusion, then the intensity ratio between peak A and peak B should stay about the same with increasing accelerating voltage as we mentioned previously. Actually the experimental fact shows a turnover in the intensity ratio of peak A and B with increasing accelerating voltage. This phenomenon demonstrates that diffusion of carrier plays a noticeable role in radiative recombination inside QWs. The back-diffusion of the secondary carriers to the bottom QW needs to be considered for higher accelerating voltage (15-22 kV) which accounts for the increase of the intensity of peak B. We also noticed that these two peaks red shift with increasing accelerating voltage.

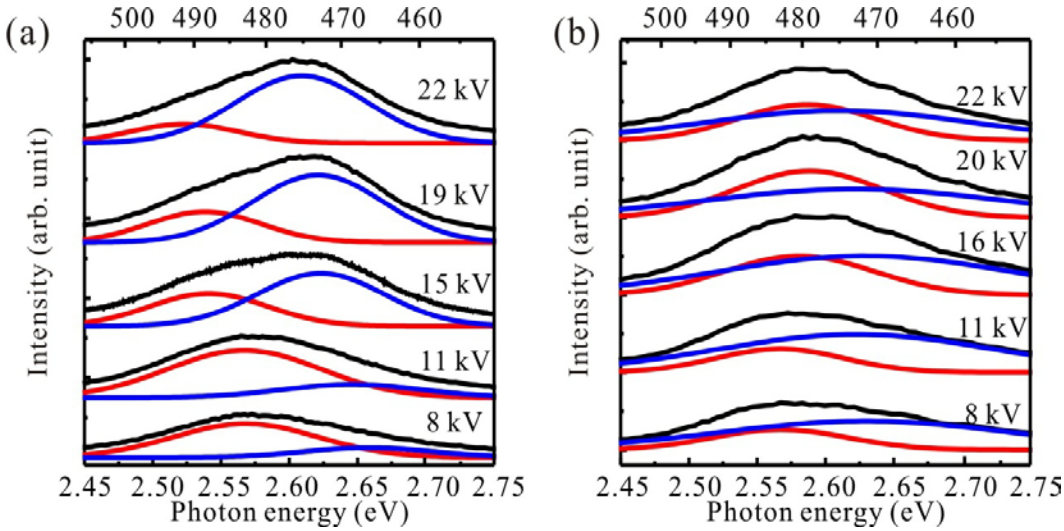

FIG. 3.10. The QW emission fitting with two Gaussian curves for sample (a) E, and (b) F with various electron beam accelerating voltages.

Since that we kept the electron beam current the same while increasing accelerating voltage which is equal to increasing excitation volume, the current densities subsequently decrease. Decreasing current densities in the active region would weaken the screening of QCSE thus leads to a red-shift of both peaks. For sample F, since an InGaN waveguide is inserted right before the growth of QWs, we believe that the misfit strain inside the QWs is alleviated by the inserted InGaN waveguide thus the QCSE effect is reduced for the QW emission. We observe that the luminescence does not shift as much as the samples without InGaN waveguides.

3.4. CONCLUSION

In summary, a comparative study has been performed in order to optimize the InGaN emitting structure with modifying parameters such as substrate materials and insertion of InGaN waveguides. For sapphire substrates, the thermal strains still remain in GaN epilayer, shifting the emission wavelengths. The LD structures grown on sapphire have higher emission intensities than those grown on GaN bulk substrates. The insertion of an InGaN waveguide stabilizes the QW emission evidenced by constant peak position under increasing electron beam accelerating voltage.

CHAPTER 4

STUDY OF STRUCTURAL AND OPTICAL PROPERTIES ON M-PLANE InGaN FILMS WITH VARIED INDIUM-CONCENTRATION

4.1. INTRODUCTION TO NONPOLAR GALLIUM NITRIDE GROWTH

Recently, considerable interests emerge in the growth of gallium nitride along nonpolar and semi-polar direction in order to avoid the spontaneous and strain-induced piezoelectric fields inherent to *c*-plane growth, which introduce severe effects and limitations on material and device. Some limitations in the *c*-plane growth are, (a) the efficiency degradation due to reduction of overlap between electrons and holes, (b) the wavelength instability with injection current, and (c) the limitation on the width of quantum well. The geometry configuration for polar $\{0001\}$ and nonpolar $\{1\bar{1}00\}/\{11\bar{2}0\}$ growth is shown in Fig. 4.1. Besides, the nonpolar growth has a polarized luminescence property due to the anisotropic in-plane strain.[57,58]

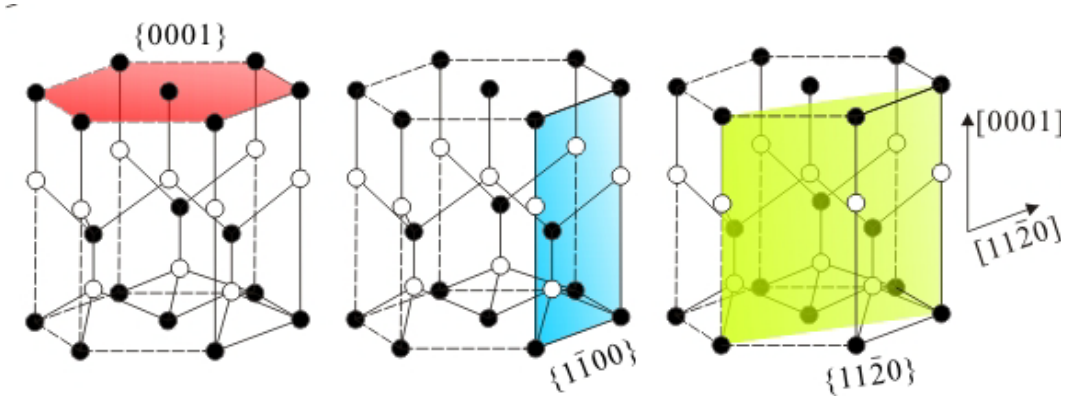

FIG. 4.1. The geometry configuration of polar *c* $\{0001\}$ and nonpolar *m* $\{1\bar{1}00\}$ and *a* $\{11\bar{2}0\}$ planes.

However, the nonpolar growth has been proven to be difficult. *A*-plane GaN[59] films can be grown on r-sapphire[60] while the candidate hetero-epitaxial substrates for *m*-plane GaN[61] are m-plane SiC[62], m-plane ZnO[63], and γ-$LiAlO_2$[64,65]. Growth of *m*-plane GaN has a strong tendency to generate high densities of dislocations and stacking faults of different kinds when grown on foreign substrates. The films typically contain 10^9 – 10^{10} cm^{-2} threading dislocations and ~10^5 cm^{-1} basal plane stacking faults.[66,67] Epitaxial lateral overgrowth (ELOG)[59,61,66,67] has proven very successful in reducing extended defect densities, to a much lower density of threading dislocations (~$10^5 cm^{-2}$) and stacking faults (~$10^3 cm^{-1}$). In contrast, the free-standing substrate made by growing thick (0001) *c*-GaN crystal by hydride vapor phase epitaxy (HVPE)[68], and then slicing in *a*- and *m*-direction, gives better epilayer quality but limited size of the nonpolar GaN substrate and high cost.[69,70] For *a*-plane growth, atomic flat surface can be achieved over relatively large area despite high densities of defects. However, in the case of *m*-plane growth, the surface morphology remains undulated even for very low extended defects. Also, the surface morphology and crystalline quality is highly sensitive to the miscut angle of the substrate.[71,72]

4.1.2. INDIUM INCORPORATION IN M-PLANE InGaN FILMS GROWN ON FREE-STANDING GAN BULK

Lately, high quality *m*-plane light-emitting diodes and laser diodes have been demonstrated with low defect density free-standing GaN substrate. However concerns still remain that striated, undulated substrate surfaces and the bowing of

the original *c*-plane GaN grown on sapphire, would cause inhomogeneous indium incorporation in the film.[73,74]

In this chapter, we provide an in-depth study of structural and optical properties of *m*-plane InGaN films on free-standing GaN substrate. Two samples of approximately 150-nm-thick *m*-plane $In_xGa_{1-x}N$ thin films were grown by metal-organic chemical vapor deposition (MOCVD) on a ~8×15-mm^2-area, 325-μm-thick free-standing GaN substrate provided by Dr. Toshiya Yokogawa from Panasonic Corporation. The substrate was sliced on *m*-plane from approximately 1-cm-thick *c*-plane GaN grown by halide vapor phase deposition (HVPE). The TD and SF densities were ~ 10^6 cm^{-2} and 10^3 cm^{-1} as confirmed by TEM. One sample has been grown with relatively low indium incorporation while the other with higher indium concentration.

4.2. MICROSTRUCTURE CHARACTERIZATION AND INDIUM COMPOSITION VIA RECIPROCAL SPACE MAPPING

The indium concentration and strain relaxation of the heterostructure is analyzed by Reciprocal Space Mapping (RSM) in an X-ray diffractometer.[75-77] The anisotropic in-plane lattice and thermal mismatch between the film and the substrate along the [0001] and the $[11\bar{2}0]$ directions lead to anisotropic in-plane strain. Thus, no less than two strain components are needed in order to evaluate the strain status of the material. When characterizing *m*-plane InGaN material, a $(2\bar{2}02)$ diffraction spot reveals strain condition of *m*-plane layer along *c*-direction since this diffraction has a *c*-component. In the same manner, a $(2\bar{3}10)$ will

indicate the strain relaxation of *m*-plane epi-layer along *a*-axis. The three main strain components ε_{ii} in each direction can be expressed as:

$$\varepsilon_{xx} = \frac{a_s - a_r}{a_r},\ \varepsilon_{yy} = \frac{m_s - m_r}{m_r},\ \varepsilon_{zz} = \frac{c_s - c_r}{c_r},$$

the directions of the *x*-, *y*-, *z*- correspond to the crystallographic orientations of *a*-, *m*-, and *c*-axis, while the subscript '*s*', '*r*' represents strained and relaxed epi-layer, respectively. All the shear strain components vanish and a relation among the three main strain components can be simplified as following by considering elastic assumptions.

$$\varepsilon_{yy} = -\frac{c_{12}}{c_{11}}\varepsilon_{xx} - \frac{c_{13}}{c_{11}}\varepsilon_{zz}, \text{ for m-plane material}$$

By analyzing the in-plane and out-of-plane strained lattice parameters of the epi-layer, we can infer the relaxed lattice parameter using the equations above, thus the strain states and indium molar fraction. The RSMs of sample with low indium content at the diffraction spots $(2\bar{2}02)$ and $(2\bar{3}10)$ are shown in Fig. 4.2. From Fig. 4.2 we observed that the InGaN epilayer is coherently grown on the *m*-plane GaN substrates on both *c*- and *a*-directions.

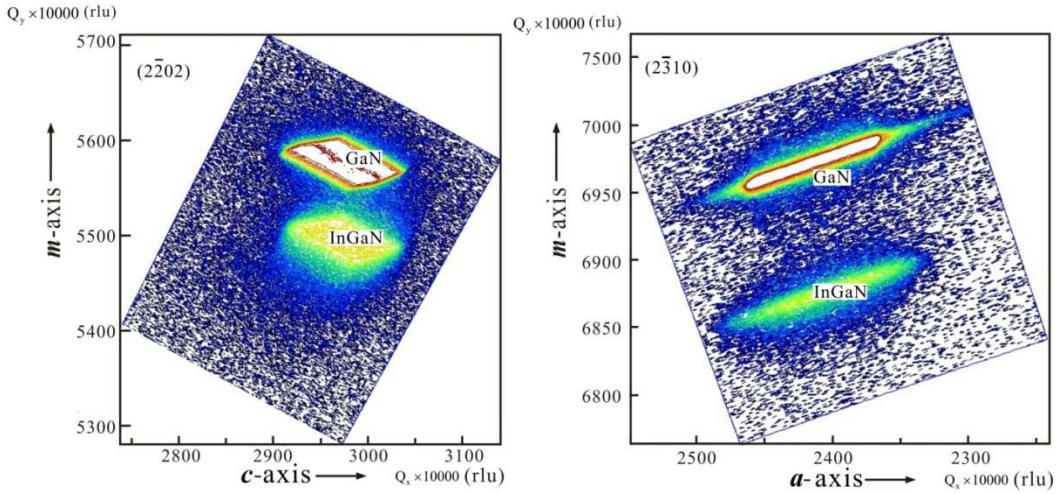

FIG. 4.2. The RSMs of X-ray intensities from sample with low indium content-$In_xGa_{1-x}N$ grown on *m*-plane GaN under $(2\bar{2}02)$, and $(2\bar{3}10)$ diffraction conditions, showing the strained flim along *c*-axis, and *a*-axis, respectively.

The strains are estimated to be ε_m = 0.57% (tensile), ε_a = -0.87% (compressive), ε_c = -0.86% (compressive) and the indium molar fraction in the $In_xGa_{1-x}N$ film is calculated to be [In] ~0.077. The in-plane strains along *c*- and *a*-axis do not have a prominent difference probably due to low [In] concentration.

The strain relaxation for the sample with higher indium molar fraction is also revealed via RSM in Fig. 4.3. These mappings show that the InGaN signals can be divided into two parts, a main peak and a significant tail as shown in diffraction spots $(2\bar{2}02)$, and $(2\bar{3}10)$.

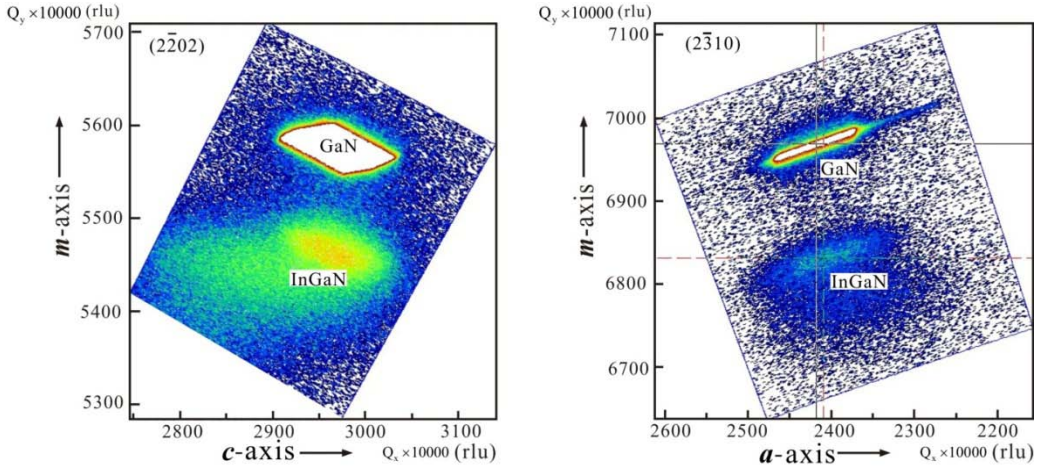

FIG. 4.3. The RSMs of X-ray intensities from sample with high indium content– $In_yGa_{1-y}N$ grown on *m*-plane GaN under $(2\bar{2}02)$, and $(2\bar{3}10)$ diffraction conditions, showing the strain relaxation along *c*-axis, and *a*-axis, respectively.

The main InGaN signal is almost coherent in the *c*-direction with the constraint from *m*-plane GaN substrate around $(2\bar{2}02)$ reflection, while it partially relaxes in the *a*- direction. The lattice parameter of InGaN main peak along *c*-direction is about 0.5181 nm, which is the same as that of bulk GaN (0.5185 nm) within error bar. The results imply that the introduction of misfit dislocations with a Burgers vector component of [0001] is not energetically favorable as compared to that with a component of $[11\bar{2}0]$. The strains for the main InGaN signal are estimated to be ε_m = 0.72% (tensile), ε_a = -0.88% (compressive), ε_c = -1.37% (compressive), and the indium molar fraction is about [In] ~11.8%. The increasing indium incorporation in the InGaN film obviously aggravates the strains which introduce the extended defects such as misfit dislocations for the

relaxation mechanism. The strong tail signal of the InGaN is also analyzed and the indium molar fraction is about [In] ~20.5%.

4.3. THE MICROSTRUCTURE AND DEFECT ANALYSIS BY TRANSMISSION ELECTRON MICROSCOPY

In order to elucidate the effects of increasing indium incorporation on the structural properties of *m*-plane InGaN, we analyzed the samples by transmission electron microscope (TEM). TEM samples were prepared in cross section using standard mechanical polishing and ion milling techniques by Mr. Kewei Sun. The crystal defect structure was studied with a field emission TEM operating at 200 kV. Fig. 4.4 exhibits the structural properties for the sample with [In] = 8%. Fig 4.4 (a) shows the InGaN/GaN interface in the [0001] projection, under $\mathbf{g} = [11\bar{2}0]$. We can clearly observe the arrays of interfacial dislocations accompanied with inclined threading dislocations, which become out of contrast under $\mathbf{g} = [1\bar{1}00]$, indicating that these dislocations have pure Burgers vector $\mathbf{b} = 1/3[11\bar{2}0]$. For a fully relaxed InGaN film with an indium content *x*~8%, the lattice mismatch is about 0.89% along the *a*-direction, corresponding to an average misfit dislocation separation of 32nm. From our observation, the separation varies from tens to several hundreds of nanometers, which may indicate that the InGaN film is locally relaxed, but still highly strained in a longer range.

In $[11\bar{2}0]$ projection as shown in Fig 4.4 (c), No stacking faults were observed suggesting that the film is still strained along c direction although it suffers a compressive strain about 0.86%. Additionally we observe inclined

stripes at an angle of ~ 60 degrees with respect to the growth direction. This inclined features lie close to the $(1\bar{1}01)$ planes. These planes are known to be the most thermodynamically stable planes in GaN. In our case they may act as active slip planes for dislocations to move. The surface of the film, as shown in Fig. 4.4 (d), seems to be undulated possibly due to the inclined features. The lines above the interface in Fig. 4.4 (b) may be originated from the intercept of these inclined features with the (0001) plane.

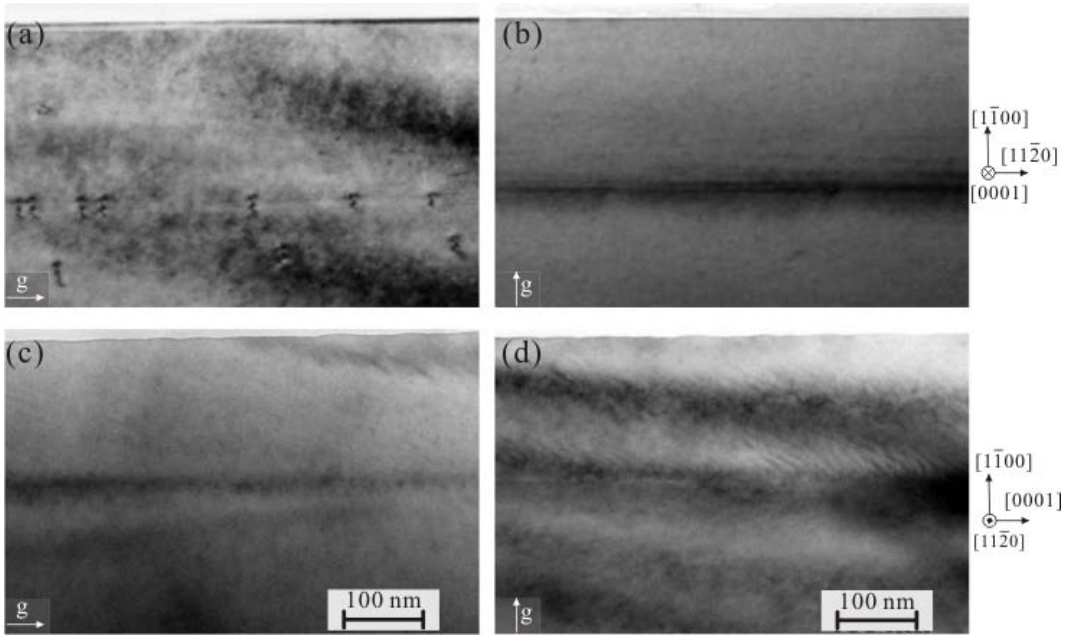

FIG. 4.4. Diffraction contrast of cross-section TEM images of low [In] thin film sample A showing the presence of defects; The images taken under [0001] projection were with (a) $\mathbf{g} = [11\bar{2}0]$, and (b) $\mathbf{g} = [1\bar{1}00]$ conditions while those taken under $[11\bar{2}0]$ projection were with (c) $\mathbf{g} = [0001]$, and (d) $[1\bar{1}00]$ conditions.

Fig. 4.5 shows the TEM images for the sample with 12/21% indium content. , The surface is quite rough. The thin film decomposes in two distinct layers which

are observed in all four images. Under [0001] projection (Fig. 4.5 (a) and (b)), the bottom layer, which is about 100-nm-thick right above GaN substrate, is free of defect. The interface between the bottom layer and the top layer is somewhat undulated.

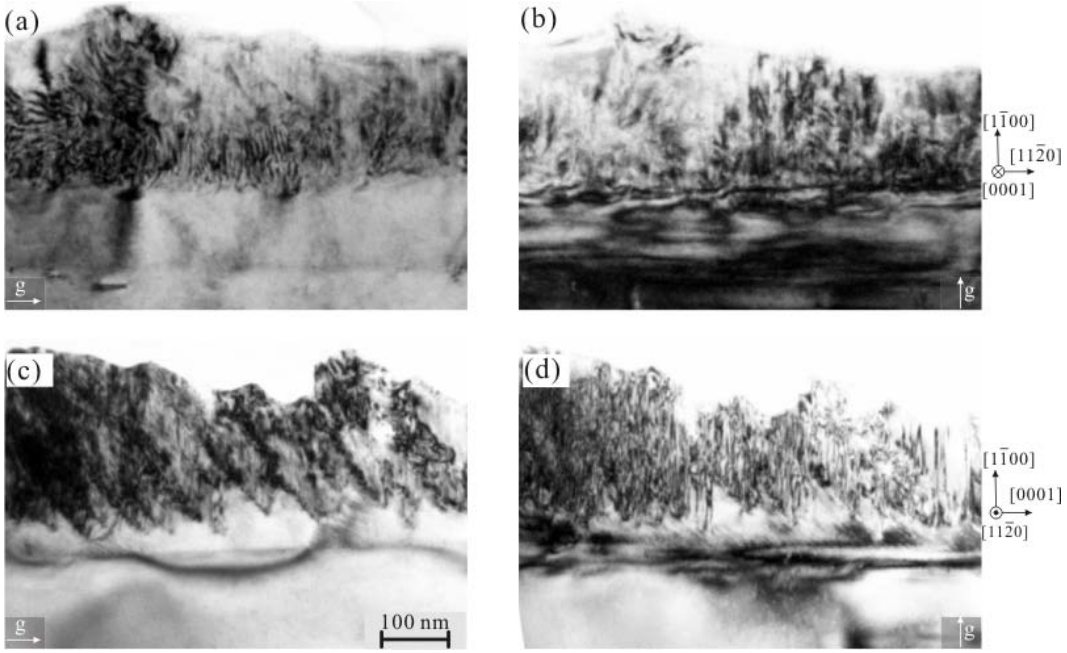

FIG. 4.5. Diffraction contrast of cross-section TEM images of high [In] thin film sample B showing two distinct layers; The images taken under [0001] projection were with (a) $\mathbf{g} = [11\bar{2}0]$,and (b) $\mathbf{g} = [1\bar{1}00]$conditions while those taken under $[11\bar{2}0]$projection were with (c) $\mathbf{g} = [0001]$, and (d) $\mathbf{g} = [1\bar{1}00]$conditions.

The material cannot hold the strain right after the interface and high densities of defects are generated such as dislocations whose edge and screw components can be observed in $[11\bar{2}0]$and $[1\bar{1}00]$diffraction conditions. Moreover, under $[11\bar{2}0]$projection, as shown in Fig. 4.5 (c) and (d), the bottom layer forms

serrated facets and the basal stacking faults (BSF) originated on the walls of the inclined facets. We suggest that the inclined facets are formed due to different growth rates along polar +*c* and –*c* direction. After reaching a certain critical thickness (100 nm for our case), the material relaxes itself by generating basal stacking faults in *c*-direction and misfit dislocations in *a*-direction. The inclined facets will effectively lower the formation energy of basal stacking faults thus most stacking faults initiated from the inclined facets since energy favorable.

4.4. SURFACE MORPHOLOGY AND CATHODOLUMINESCENCE OF THE THIN FILMS

Surface morphology of the *m*-plane InGaN thin films are studied by atomic force microscope (AFM), SEM, and CL in order to investigate and correlate surface features with defects in the InGaN films. CL measurements were performed in a scanning electron microscope equipped with a commercial spectrometer and a photomultiplier tube, using an electron beam current of 0.4 nA. Depth-resolved CL was performed on the [In] = 8% sample with beam accelerating voltage ranging from 5 to 13 kV, as shown in Fig. 4.6 (a). Only one InGaN band-edge emission peak is observed, located at about 395 nm (3.139 eV) which does not shift with increasing accelerating voltages, suggesting that homogeneous indium incorporation occurs along the growth direction. Using a bowing parameter of b=2.00, and the equation,

$$E_{InGaN}^{CL}(x) = (1-x)E_{GaN} + xE_{InN} - bx(1-x),$$

the indium molar fraction is about 8%, which is consistent with the value given by RSM. The surface morphology is investigated via AFM and SEM and is shown in Figs. 4.6 (b) and (c). Scratches of ~ 5 μm long are observed along [11$\bar{2}$0] direction.

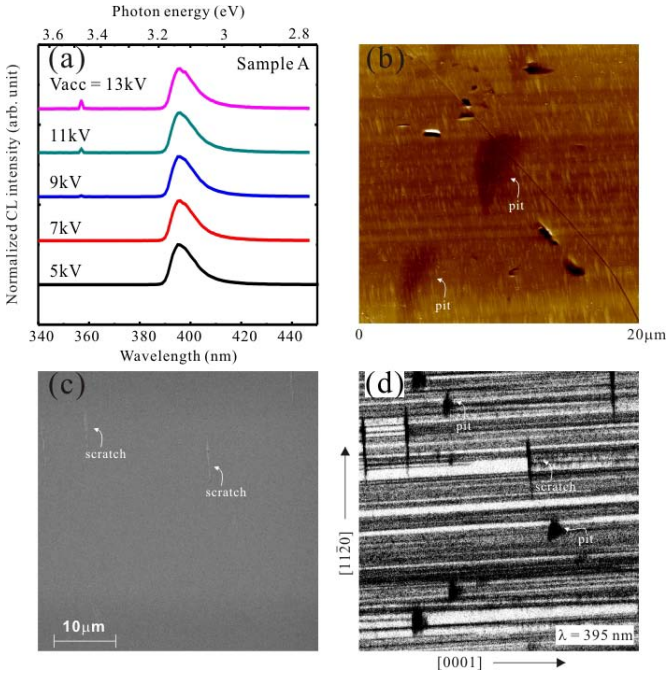

FIG. 4.6. Cathodoluminescence and surface morphology of sample with [In] = 8%. (a). Depth-resolved CL spectra with accelerating voltage in the range between 5 and 13 kV. (b). AFM image reflects the topography of the sample surface in a 20×20 μm^2 area. (c). The SEM image shows the scratches along [11-20] direction in a 50×50 μm^2 area. (d). Monochromatic CL mapping shows the horizontal bands with widths varying from 300 nm to 1200 nm.

The CL imagingwas carried out to investigate spatial variation of the light emission at monochromatic wavelength λ = 395 nm, as shown in Fig. 4.6 (d). Interestingly, the light emission is not spatially uniform with bright bands

propagating along *c*-direction perpendicular to the scratches. These bands have widths varying from 300 nm to 1200 nm. The scratch could be due to a difference in lateral growth rate along the *c* and -*c* direction, which leaves an un-coalescence region (i.e. scratch) on the surface. Also some triangular dark pits are observed in the monochromatic CL image, which are correlated to surface defects as shown in Fig. 4.6 (b).

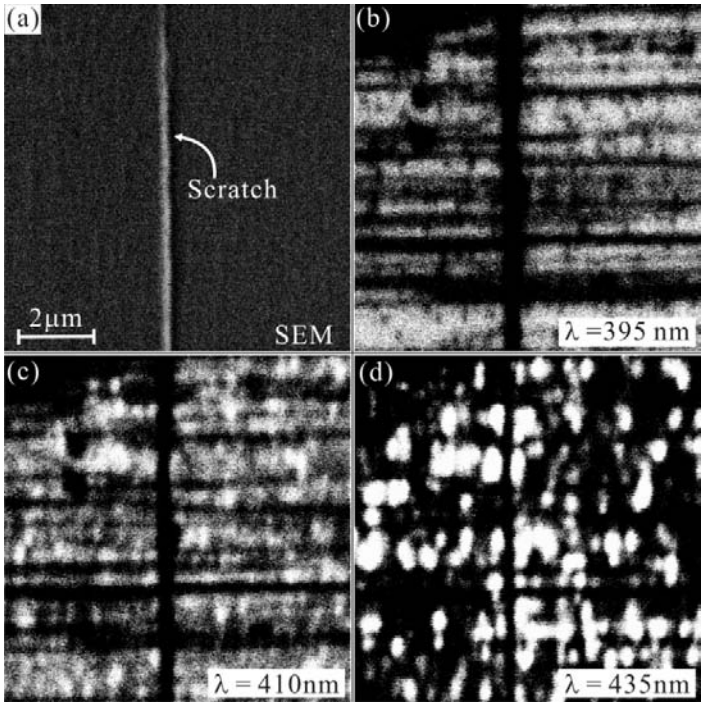

FIG. 4.7. Spatial distribution of luminescence (a) SEM image with a scratch at the center. (b) Peak emission showing stripe luminescence (c) low energy shoulder emission (λ = 410 nm) showing stripe with dot luminescence (d) further lower energy shoulder emission (λ = 435 nm) showing dot luminescence.

The magnified SEM and monochromatic CL images are shown in Fig. 4.7. With increasing the monitored wavelength from peak (395 nm) to lower energy shoulder (435 nm), the pattern gradually changes from stripe luminescence to dot

luminescence. In order to understand the luminescence features on the surfaces, a close-up at the surface topography via AFM is shown in Fig. 4.8. Fig. 4.8 (a) shows an AFM image of the clean surface without the pits. The surfaces consist of oval-shaped features which have an average dimension of ~ 1μm in length and ~100 nm in width. The height difference between the center and the edge of a oval cell is about 4 nm. All the oval cells pile up along the *c*-direction. Figs. 4.8 (b) and (c) show the regions with a pit in the center (the dark area) taken in a 10×10 μm^2. The depth of the pit is as shallow as 5 nm with respect to the normal growth region. There is a very low density of oval cell grown inside the valley.

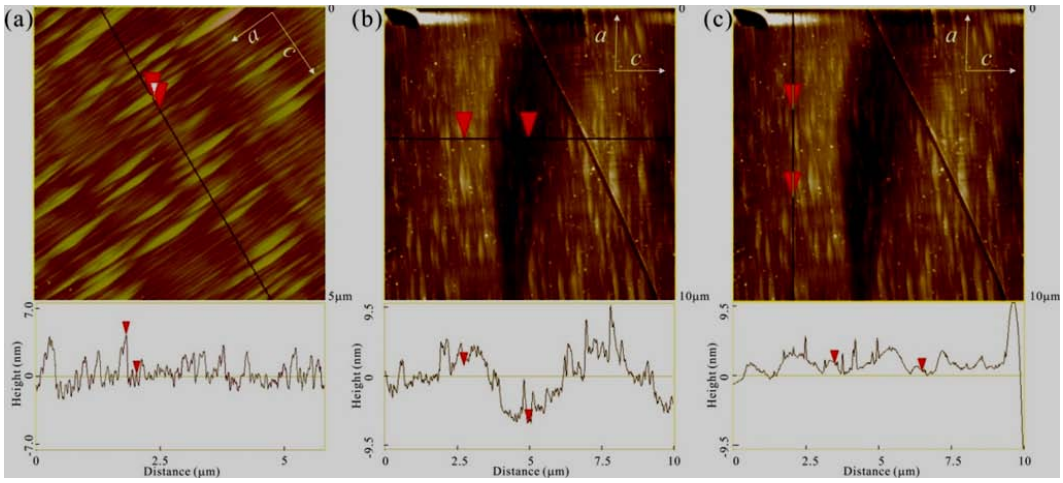

FIG. 4.8. Close-up look at the surface topography using AFM. (a) AFM image taken at a 5×5 μm^2 area. (b), (c). AFM image taken at a 10×10 μm^2 area with horizontal (b) and vertical (c) height scan.

We believe the bright bands of the CL image of the main peak correspond to the column of oval-shaped features due to the similarity in dimensions, while the dot luminescence features are attributed to the single oval cell. The inhomogeneous light emission pattern could be due to the surface morphology which limits the light extraction or the inhomogeneous crystalline qualities in different regions.

The optical and topographic properties of the sample with 12/21% indium content were analyzed in the same manner. In Fig. 4.9. (a), An emission at 2.31eV (537nm) is observed at 3 kV. As the electron beam energy is increased, a second emission at 2.90 eV (427 nm) and the GaN donor-bound excition are observed. This means there are two layers with different indium content: low indium content layer closer to the GaN substrate, followed by a high indium content layer grown on top. The existence of two sublayers is consistent with the RSM and TEM

results. The layer with low indium content is estimated to be ~ 13.2% while the one with high indium content is about 28.1%. Fig. 4.9 (b) shows the AFM image of the top surface of this sample.

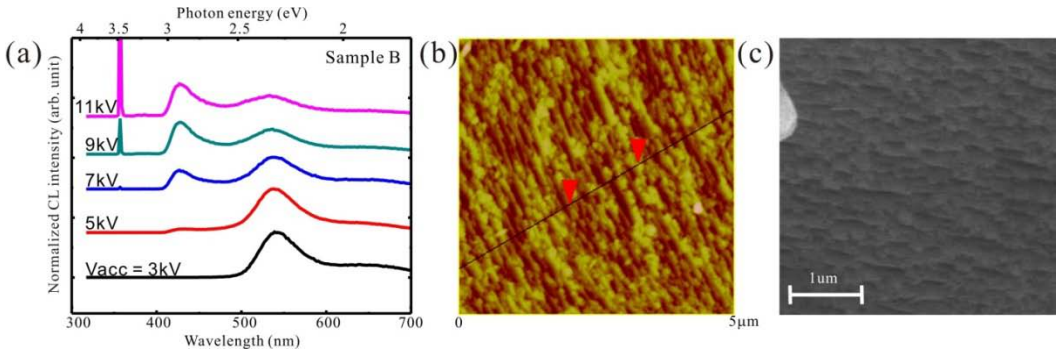

FIG. 4.9. Cathodoluminescence and surface morphology of sample B. (a) Depth-resolved CL spectra with accelerating voltage in the range between 3 and 11 kV. (b) AFM image reflects the topography of the sample surface in a 5×5 μm^2 area. (c) The SEM image in a 4×4 μm^2 area.

The surface is much rougher than that of sample with 8% indium content due to higher indium incorporation. The root mean square (RMS) roughness is about 15.7 nm as compared to 1.3 nm of sample with 8% indium content. The prominent undulation of the sample surface was observed by SEM shown in Fig. 4.9 (c). CL images taken at different photon energies, as shown in Fig. 4.10, reveal several interesting features: emission of the low indium content layer is not spatially uniform with stripe and dot luminescence. This trend is similar to the sample with 8% indium content which is also highly strained film. However, the high indium content layer has a uniform emission pattern..

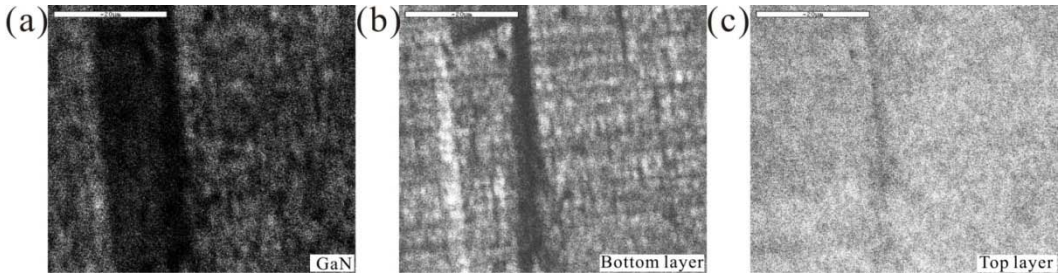

FIG. 4.10. Monochromatic CL mapping at (a) GaN band-edge emission (b) bottom InGaN emission (c) top InGaN emission.

4.5. TEMPERATURE DEPENDENCE OF LUMINESCENCE AND RECOMBINATION DYNAMICS

To investigate the temperature dependence of InGaN luminescence behavior, the CL spectra at a temperature range from 4 to 300 K were performed. For the sample with 8% indium content, as shown in Fig. 4.11 (a), only one asymmetric emission peak is observed at 4 K. For the sample with 12/21% indium content, shown in Fig. 4.11 (b), the bottom sublayer corresponding to 12% indium content also exhibits an asymmetric shape in peak emission. We believe that the asymmetric shaped peak emissions come from the specific regions different from the highly strained matrix (like the oval cells). The top sublayer corresponding to 21% indium content has higher internal quantum efficiency (IQE) as compared with the bottom sublayer. This is probably due to a better carrier confinement caused by indium fluctuation in top sublayer with higher indium content.

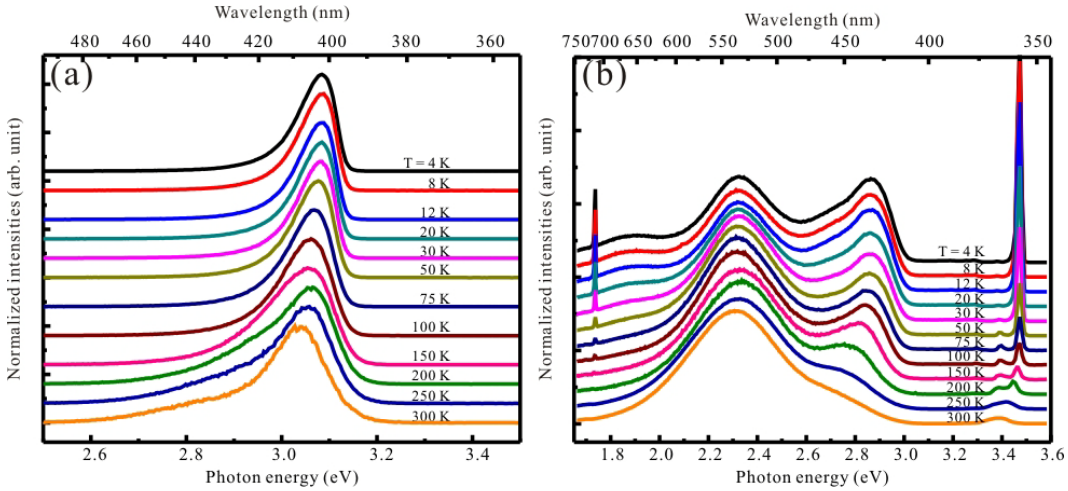

FIG. 4.11. The temperature dependence of luminescence of the samples (a) 8% indium content, (b) 12/21% indium content.

Carrier excitation and recombination dynamics of the *m*-plane films were studied by time-resolved CL (TRCL). Transients were obtained by blanking the electron beam with a square pulse, with a width of 100 ns at a frequency of 1 MHz. The TRCL transients are shown in Fig. 4.12.

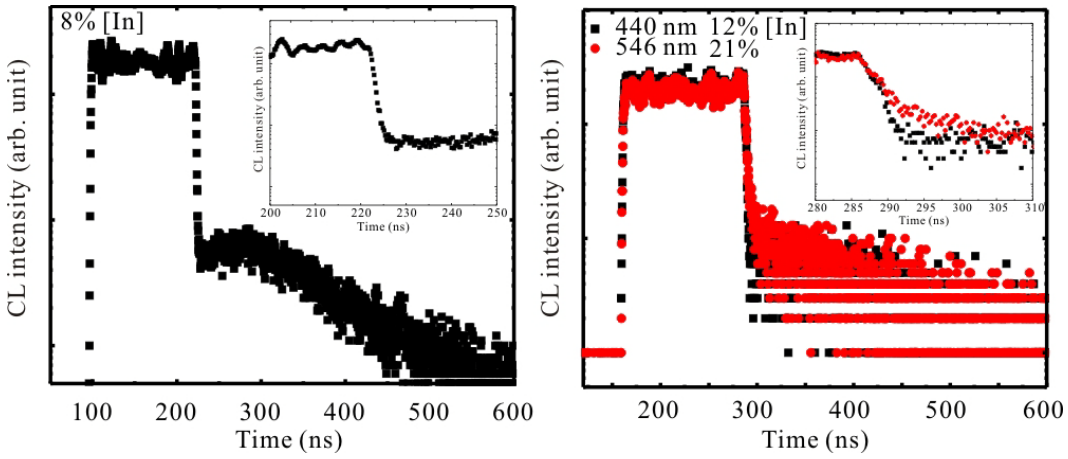

FIG. 4.12. The TRCL transient of (a) the sample with 8% indium content (b) the sample with 12/21% indium content at 4.5 K. The inset is the magnified region showing the decay.

The recombination lifetime of sample with 8% indium content is 1.14 ns. The recombination lifetime of the sample with 12/21% indium content is 1.86 ns and 2.48 ns for the 12% and 21% indium content layer, respectively. It is noticed that recombination lifetime increases with increased indium composition in the film. This could be due to a decrease of the oscillator strength.

4.6. CONCLUSION

In conclusion, the properties of two *m*-plane InGaN thin films grown by metal-organic chemical vapor deposition on free-standing *m*-GaN were investigated via CL, AFM, RSM and TEM. The sample with 8% indium content is fully strained on the substrate with few interfacial misfit dislocations observed. CL and AFM images correlate the oval features on the surface with the inclined stripes in TEM images. For the sample with high indium content, a smooth thin film (bottom sublayer), containing large stress due to lattice mismatch between InGaN and GaN, was initially grown on GaN substrate. The indium mole fraction is limited to 12% caused by the lattice mismatch strain. The serrated growth features are due to a difference in lateral growth rate along $+c$ and $-c$ direction. The serrated facets are very effective in lowering the formation energy of defects such as stacking faults and misfit dislocations. A highly defective film (top sublayer) with high indium content of ~ 21% was grown thereafter. The increase in indium mole fraction caused a reduction in the large stress in the film, which is known as “compositional pulling effect”. It is worth noted that the indium compositional change is abrupt at the interface

between top and bottom sublayer for this *m*-plane InGaN film. Moreover, the peak emission exhibits an asymmetric shape as observed in CL spectra for highly strained samples with 8% and 12% indium content. The main peak originated from the strained matrix while the lower energy tail is attributed to some oval-shaped cells evidenced by CL monochromatic images. However, the peak exhibits a symmetric shape and a spatially uniform emission for highly relaxed sample with 21% indium content. Also, for highly strained samples with 8% and 12% indium content, the efficiencies are lower than that for highly relaxed sample with 21% indium content. This is explained by the better confinement with higher indium content. Finally, it is found that the carrier lifetime increases with increased indium content which is due to the decrease of oscillator strength.

CHAPTER 5

OPTICAL AND STRUCTURAL EVIDENCES FOR THE EXISTENCE OF IN-PLANE PIEZOELECTRIC FIELDS IN *M*-PLANE QUANTUM WELLS

ABSTRACT

The optical and structural properties of blue light-emitting diode structures grown on free-standing *m*-plane GaN have been studied using cathodoluminescence and transmission electron microscopy. An inhomogeneous spatial distribution in the InGaN quantum well emission has been observed with two distinct peaks present at 428 and 460 nm at room temperature. The inhomogeneous emission is associated with the presence of dislocations that originate at the InGaN layers. It is proposed that the difference in peak energy positions at room temperature is due to *in-plane* piezoelectric fields within the dislocated regions. The longer-wavelength peak exhibits a continuous blueshift with increasing injection current, which is attributed to enhanced screening of the piezoelectric fields.

---

[*]Contents in this chapter were published as: Y. Huang, K. W. Sun, A. M. Fischer, Q. Y. Wei, R. Juday, F. A. Ponce, R. Kato and T. Yokogawa, *Effect of misfit dislocations on luminescence in m-plane InGaN quantum wells*, Appl. Phys. Lett. **98**, 261914 (2011).

5.1. INTRODUCTION*

Solid-state lighting for full color displays has attracted much attention during the past two decades. Light-emitting diodes (LEDs) and laser diodes (LDs) emitting in the red portion of the electromagnetic spectrum are made mainly of AlInGaP materials[78] while blue and green light emitting devices are made of InGaN-based materials. Blue LEDs[79] and LDs[80] with high quantum efficiency are now commercially available. Devices operating in the green wavelength range have met some fundamental limitations associated with the growth of higher indium content InGaN in the active region. These are thought to be related to a low stability of indium-rich quantum wells that result in composition fluctuations; high defect densities that degrade the crystal quality; and piezoelectric fields due to the large lattice mismatch between InN and GaN. Much effort has been made to overcome these obstacles. Recently, green lasers have been successfully produced on conventional free-standing *c*-plane GaN substrates, operating at wavelengths from 500 to 515 nm.[81,82]

This was achieved by improving the growth conditions to alleviate the instability of In-rich InGaN which is thought to be the key limiting factor. On the other hand, much concern exists about the increasing piezoelectric fields due to the absence of a center of symmetry in the wurtzite lattice and a large lattice mismatch, which are thought to hamper the radiative recombination efficiency resulting from the quantum-confined Stark effect (QCSE).[83,84] A preferred approach to reduce or nullify the QCSE is to rotate the crystal growth direction so

that the net polarization field lies parallel to the thin-film plane. This can be accomplished by growth on $\{11\bar{2}0\}$ *a*-plane[85-87] or on $\{1\bar{1}00\}$ *m*-plane substrates.[88-90] Such non-polar device structures are expected to have no internal fields in the quantum well (QW) region. Green lasers on *m*-plane freestanding GaN substrates have been recently reported with a lasing wavelength of 499.8 nm.[91] However, the appearance of a double peak emission in the luminescence of InGaN QWs grown on the *m*-plane configuration has been observed but not understood. Our report in this chapter on a structural and optical study indicates that in-plane PE fields are introduced by lattice mismatch relaxation that breaks the continuity of the quantum wells, resulting in regions with red-shifted emission.

5.2. EXPERIMENTAL DETAILS

Our study focuses on LED structures grown by metal-organic chemical vapor deposition provided by Dr. Toshiya Yokogawa from Panasonic Corporation. A 2.5 µm-thick silicon-doped GaN film was deposited on a ~400 µm-thick undoped, free-standing, $(1\bar{1}00)$ *m*-plane GaN substrate. Subsequently, three periods of 15 nm-thick $In_{0.15}Ga_{0.85}N$ quantum well layers with 30 nm-thick GaN barrier layers were grown. After insertion of an AlGaN electron blocking layer, the LED structure was completed with a 320 nm-thick magnesium-doped GaN layer.

The spatial variation of the light emitting properties was studied using cathodoluminescence (CL) in a scanning electron microscope equipped with a commercial spectrometer and a photomultiplier tube. In this study, we use a JOEL 6300 SEM equipped with a LaB_6 electron gun, with electron beam current

set at 0.4 nA, , an accelerating voltage at 7 kV, and magnifications between 2000*X* and 5000*X*. Temperature as low as 4 K is achieved by using a transfer tube and a helium pump to circulate liquid helium to cool the sample stage. An adjustable heater with a temperature monitor enabled us to control the temperature in the range of 4 K to 300 K. Monochromatic CL imaging is realized by correlating the position of the focused electron beam and the luminescence intensity recorded by the light detector.

The thin-film microstructure was studied with a Philips CM200 transmission electron microscopy (TEM). The instrument is equipped with a field emission gun operated at 200 kV. Bright field images were taken under various diffraction conditions. TEM samples were prepared in cross section using standard wedge polishing followed by a 3.5 keV ion milling techniques held at liquid-nitrogen temperature. These TEM studies were performed by Mr. Kewei Sun.

5.3. SURFACE MORPHOLOGY AND STRUCTURAL INFORMATION

A secondary electron image showing the sample surface morphology is shown in Fig. 5.1(a). Trenches are observed on the surface with a depth of ~ 200nm, and they appear uniformly distributed along the *a*-direction. The separation between trenches may be a result of surface misorientation with respect to the crystallographic plane (miscut angle). The elongated plateau regions between neighboring trenches are relatively smooth with a root-mean-square roughness of 8 nm. Depth-resolved CL spectra at 300 K were obtained by varying the accelerating voltage in the 5 to 19 kV range with a constant beam power of 1.5 microwatts, and are shown in Fig. 5.1(b). Acceptor-bound excitons (ABE) at 365 nm (3.40 eV) and donor-acceptor pairs (DAP) at 381 nm (3.25 eV) were observed in the emission spectra from the p-type region. The *m*-plane QW luminescence is characterized by the appearance of a pair of peaks. The ratio of the peak intensities does not vary with beam accelerating voltage in this range, which rules out the possibility that these two peaks originate from different QWs.

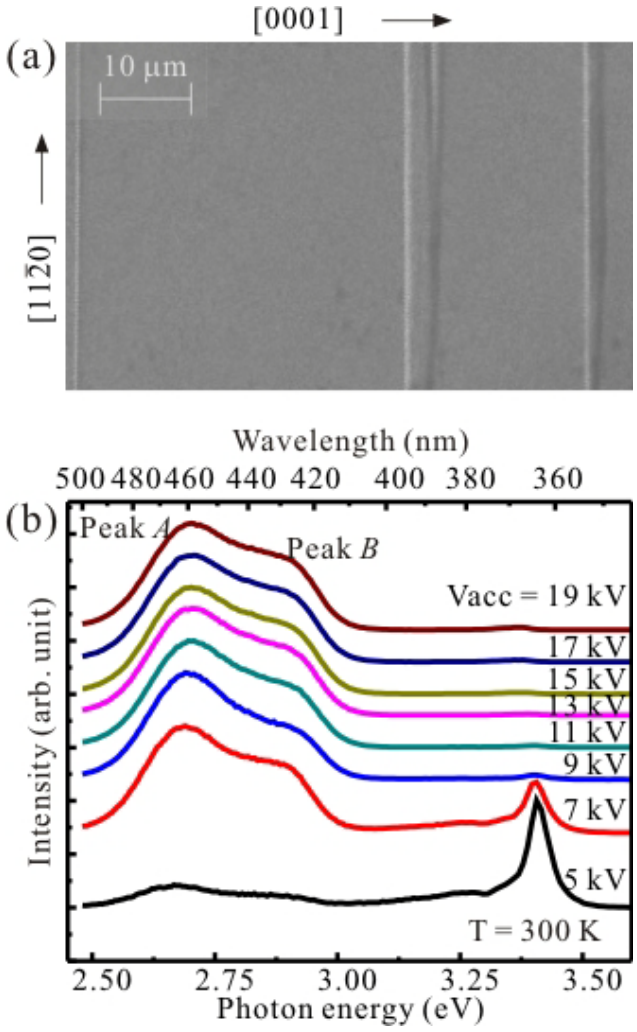

FIG. 5.1. (a) SEM image of the top surface of the InGaN quantum well sample showing the surface morphology. (b) Depth-resolved CL spectra taken at room temperature (300 K) illustrating that the intensity ratio of peak *A* and peak *B* does not vary with beam accelerating voltage in the range of 5 kV to 19 kV.

Strain relaxation along *c* and *a* directions, and the composition of the quantum wells, are revealed in the reciprocal space maps (RSM) around diffraction spots $(2\bar{2}02)$ and $(2\bar{3}10)$ shown in Fig. 5.2. The InGaN QWs are fully strained to fit the GaN underlayer in both directions. The InN molar content in

quantum wells is determined from RSM to be ~ 15%. Using a bowing parameter of 2, we estimate an energy gap of 2.894 eV (437 nm), which is consistent with the spectra shown in Fig. 5.1 (b)

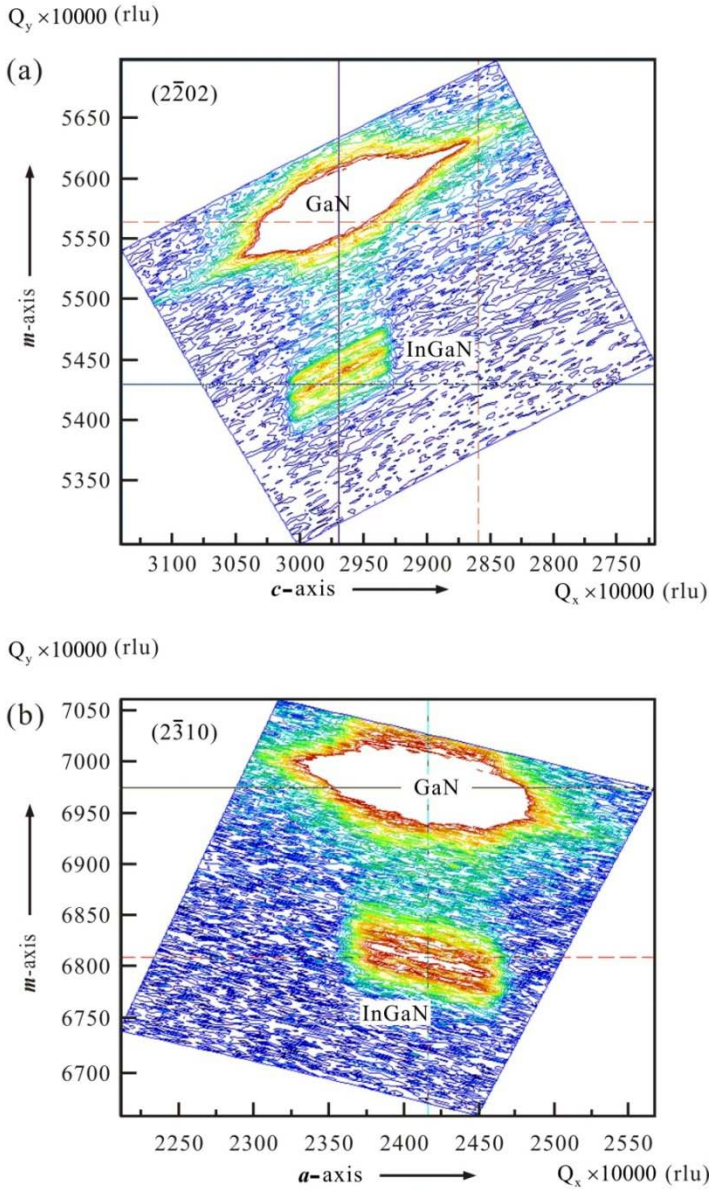

FIG. 5.2. Reciprocal space mapping (RSM) around (a) (2$\bar{2}$02) and (b) (2$\bar{3}$10) diffraction peaks showing that the QWs are pseudomorphic to the GaN substrate.

5.4. INHOMOGENEOUS SPATIAL DISTRIBUTION OF LUMINESCENCE

The area-average CL spectrum in Fig. 5.3(a) can be well fitted with two Gaussian functions centered at 460 nm (peak *A*) and 428 nm (peak *B*) with full width at half-maxima (FWHM) of 200 and 160 meV, respectively. These large FWHM values may reflect compositional disorder. In order to understand the origin of these two peaks (peak *A* and peak *B*), the monochromatic CL mapping in Fig. 5.3(b) was performed at the peak *B* emission wavelength (λ= 428 nm). An inhomogeneous spatial distribution in the light emission was observed on the *m*-plane, with horizontal stripes along the [0001] direction, and alternating contrast along the $[11\bar{2}0]$ direction. The spot-mode spectra in Fig. 5.3(a), corresponding to spots 1 (S1) and 2 (S2) in Fig. 5.3(b), indicate that the peak *A* and peak *B* emissions are localized. This bimodal emission is responsible for the horizontal stripes.

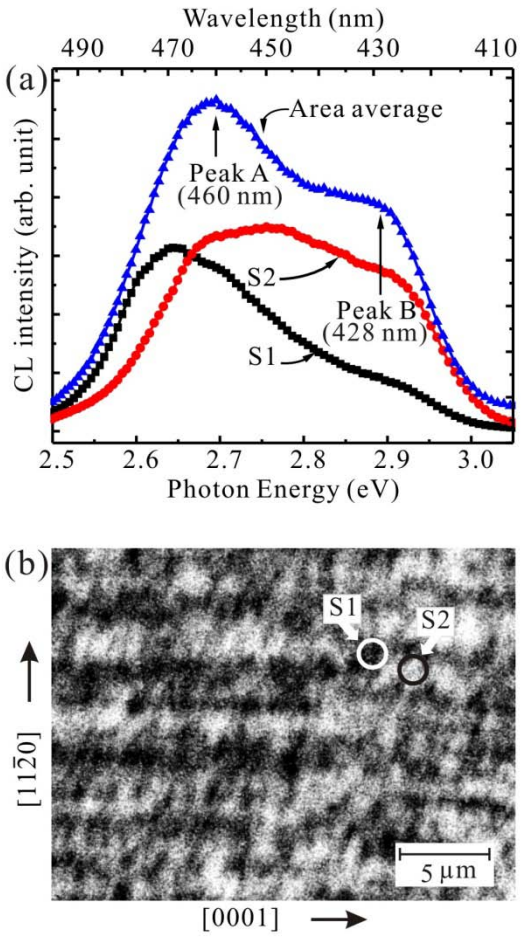

FIG. 5.3. Luminescence characteristics of the *m*-plane InGaN/GaN QW structure. (a) CL spectra taken at room temperature showing two emission peaks in an area-average spectrum of 500 μm^2, and at specific positions (spot mode) S1 and S2 in (b). (b) Monochromatic CL image taken in plan-view at the peak *B* emission (λ = 428 nm), at room temperature.

5.5. MICROSTRUCTURE DEFECT ANALYSIS ON THE QUANTUM WELL REGION AND P-LAYER USING TRANSMISSION ELECTRON MICROSCOPE

Cross-section TEM was performed by Mr. Kewei Sun using standard mechanical polishing and argon ion milling techniques. Basal-plane stacking faults and inclined dislocation pairs originating at the InGaN layers were observed by TEM.

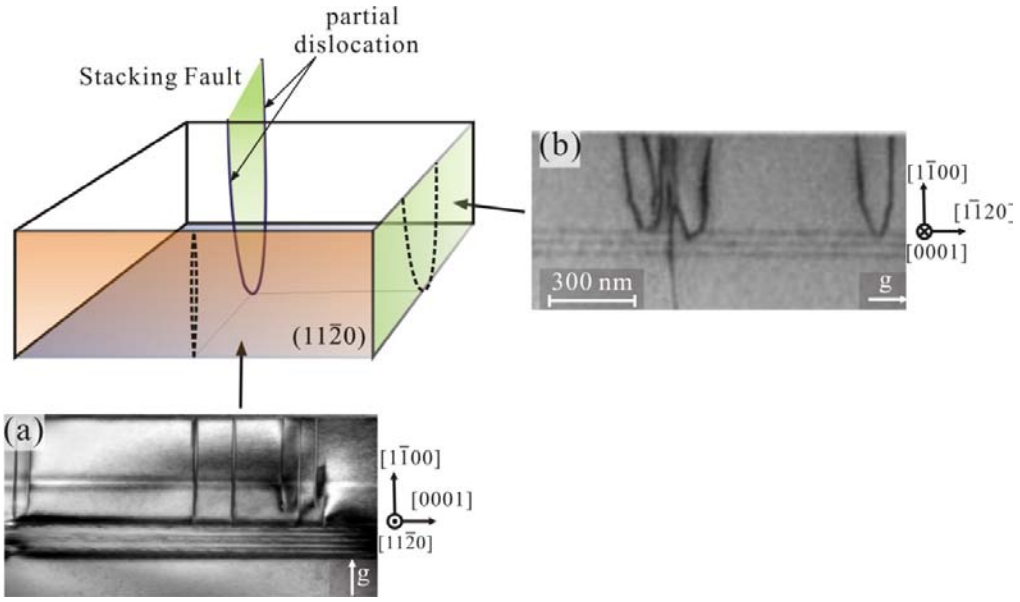

FIG. 5.4. Cross-section TEM images of the region containing the QWs and the top surface, showing the presence of basal-plane stacking faults and their bounding partial dislocations; (a) $[11\bar{2}0]$ projection with $\mathbf{g} = [1\bar{1}00]$. (b) [0001] projection with $\mathbf{g} = [11\bar{2}0]$ showing dislocation half loops bounding I_1 stacking faults, which are observed edge-on in (a).

By applying diffraction-contrast ***g.b*** analysis to the $[11\bar{2}0]$ and [0001] projection images in Fig. 5.4, it can be concluded that the inclined dislocation dipoles are of the Frank-Shockley type, bounding I_1 type basal plane stacking faults with a lattice displacement of $1/6[2\bar{2}03]$.[92, 93]

The distance between the dislocated regions in Fig. 5.4(b) is ~ 800 nm, which is similar to the width of the bright regions in Fig. 5.3(b). We therefore propose that the bright stripes are related to dislocation region while dark stripes are related to dislocation-free region.

5.6. TEMPERATURE DEPENDENCE OF DOUBLE-PEAK INGAN QUANTUM WELL EMISSION

The temperature dependence of the double-peak InGaN QW emission spectra in the range from 4 to 300 K is shown in Fig. 5.5(a). The spectra were taken with an electron beam current of 0.4 nA. In the lower temperature regime (4 – 100 K), the shape of the QW emission line is asymmetric; while at temperatures above 200 K, well defined and separated double emissions are observed (the peaks *A* and *B*). We speculate that these peaks exist at every temperature point measured, but behave differently with thermal excitation. To check on this idea, we closely fitted the QW emissions with two Gaussian functions, with a standard deviation $\sigma_E \sim \pm 0.001$ eV. The temperature dependence of the fitting Gaussian functions has been tracked by following their intensity, center position, and FWHM values, and it is shown in Fig. 5.5(b). The peak energies of *A* and *B* obtained from such fitting and plotted in Fig. 5.5(c), show a wide difference in energy shifts. Peak *A*

exhibits a red shift of ~190 meV from 4 to 300 K, which is about 120 meV more than the typical band gap energy shift with temperature.

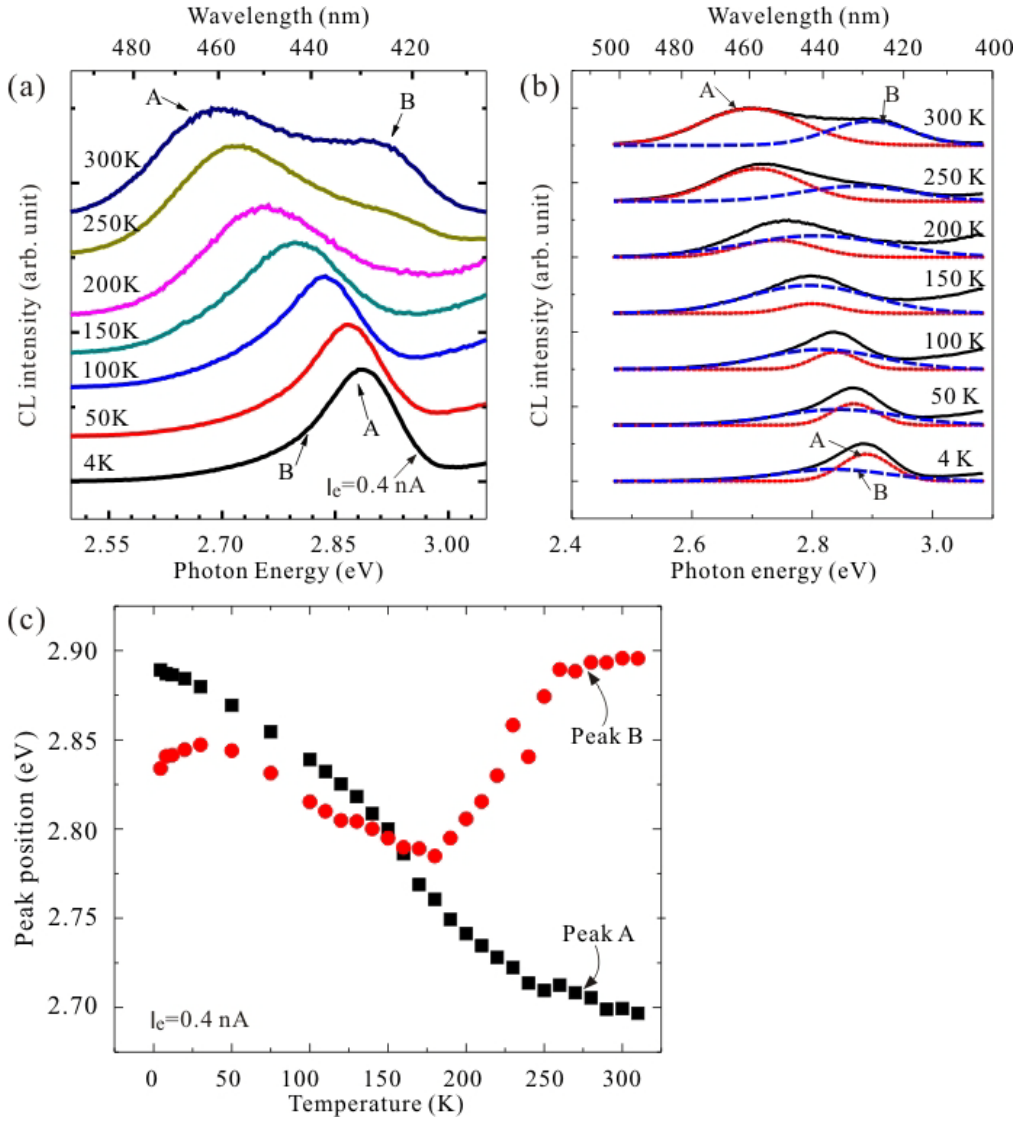

FIG. 5.5. Temperature dependence of the CL emission of *m*-plane InGaN quantum well structures. (a) CL spectra taken over the temperature range from 4 to 300 K. (b) Temperature evolution of peak *A* and peak *B* (the black solid line represents experimental data, the red dotted line is Gaussian curve A, the blue dash line is Gaussian curve *B*). The fitting is accurate and strongly supports the

interpretation of the existence of two separate peaks. (c) Temperature behavior of the *A* and *B* peak energies.

In contrast, Peak *B* shows an S-shape behavior (blue-red-blue shift). The first blue shift could be due to thermal oscillations at local potential minima, while the subsequent red shift could be due to carrier re-localization inside the QWs, and the following blue shift beginning at 150 K could be due to band tail filling.[94,95]

5.7. MISFIT DISLOCATION-INDUCED IN-PLANE PIEZOELECTRIC FIELDS MODEL

We next explore the relationship between luminescence and microstructure. We propose that the presence of dislocation loops threading from the QWs, illustrated in Fig. 5.6, breaks the continuity of the QW layer and introduces non-uniform strain fields, ranging from full-strain in the defect-free areas to nearly-relaxed regions near the dislocation segments at the QW interface. This strain non-uniformity along the *c*-axis results in PE fields and a pronounced QCSE in the plane of the QWs inside the dislocated region.[96]

At low temperatures, carriers are highly confined at local potential minima and are not sensitive to PE fields, thus the radiative recombination is direct and localized. At temperatures above 150 K, carriers are activated from localized centers and drift under the influence of the PE fields, thus the radiative recombination is mostly sidewise in Fig. 5.6, which would account for the additional red shift in peak *A*.

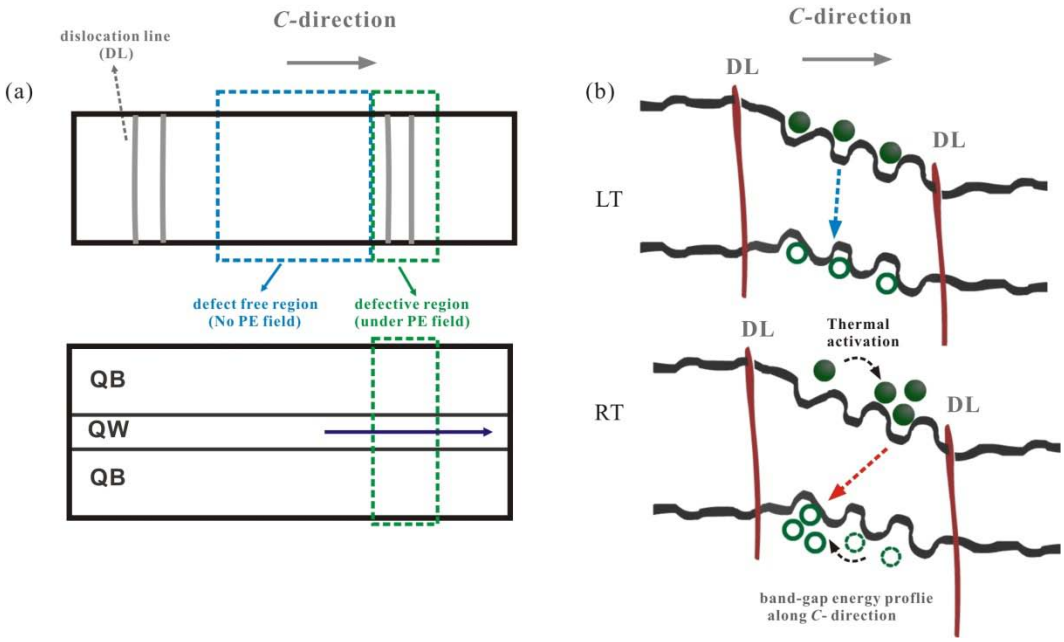

FIG. 5.6. (a) Schematic diagram illustrating how dislocation lines (DLs) break the material symmetry and generate PE fields inside quantum wells (left). (b) Band structure in the dislocated region where PE fields are present at low temperature (up right) and room temperature (bottom right).

5.8. SCREENING PIEZOELECTRIC FIELDS BY INCREASING ELECTRON BEAM CURRENT

It is known that high electron beam currents can screen the PE fields, which results in a blue shift. In order to verify the existence of PE fields, we look at the effect of electron beam current on the luminescence. CL spectra were obtained with increasing electron beam currents at various temperatures. The results are shown in Fig. 5.7.

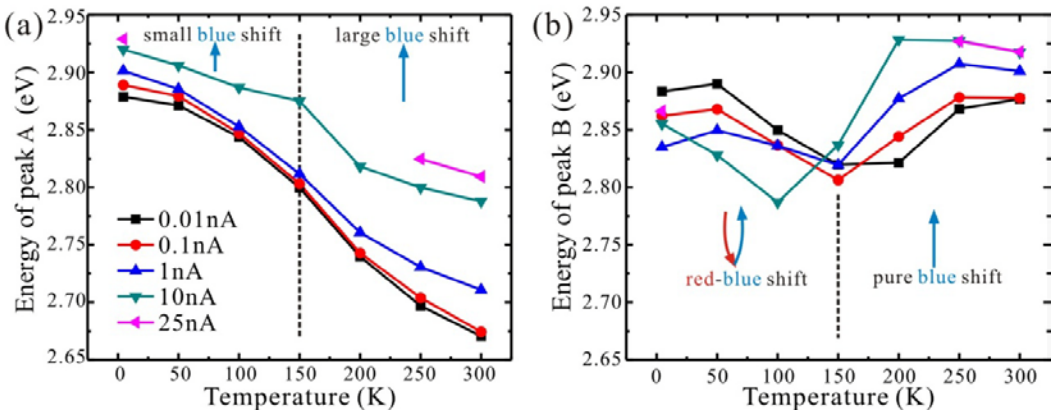

FIG. 5.7. Carrier injection effect on the CL spectra as a function of temperature. Peak energy values of *A* (a) and *B* (b) as a function of temperature for electron beam current from 0.01 nA to 25 nA.

Peak *A* blue shifts with increasing electron beam current due to free carrier screening by *in-plane* piezoelectric fields. This effect is enhanced at higher temperatures (150 – 300 K) as more free carriers are excited. On the other hand, the *in-plane* piezoelectric field is negligible in the dislocation-free regions due to the larger dimensions. We propose that peak *B* stems from the dislocation-free regions. Its S-shape behavior indicates the presence of indium fluctuation in the QWs. The observed peak energy is an average of the emissions from shallow and deep localization centers. When we increase the beam current at low temperatures (4 – 100 K), we expect that at first more carriers recombine at the deep localization centers with lower emission energy (red shift), and then the trend reverses to a blue shift due to band filling. At high temperatures (150 - 300 K), the shallow localization centers are not active due to band filling of the deep centers, which results in monotonic blue shift.[97]

5.9. ARRHENIUS PLOTS OF THE INTEGRATED CL INTENSITY FROM THE QUANTUM WELL EMISSIONS

Fig. 5.8 shows Arrhenius plots of the integrated CL intensity from the QW emission peaks *A* and *B* over the temperature range under investigation. We use the following equation for quantitative description of the CL intensities

$$I(T) = I_0 / [1 + \alpha \exp(-E_\alpha / kT)].$$

The best fitting gives activation energies of 18 meV and 89 meV for peak *A* and *B*, respectively. The coefficient α represents the strength of the luminescence-quenching mechanism. Variations in the quenching mechanism with temperature are due to thermal emission of carriers out of a confining potential, exhibiting a characteristic activation energy. In the case of peak *A*, originating from the dislocated region, the carriers easily escape the localized centers under the influence of PE field, and thus the activation energy of peak *A* is smaller than peak *B*.

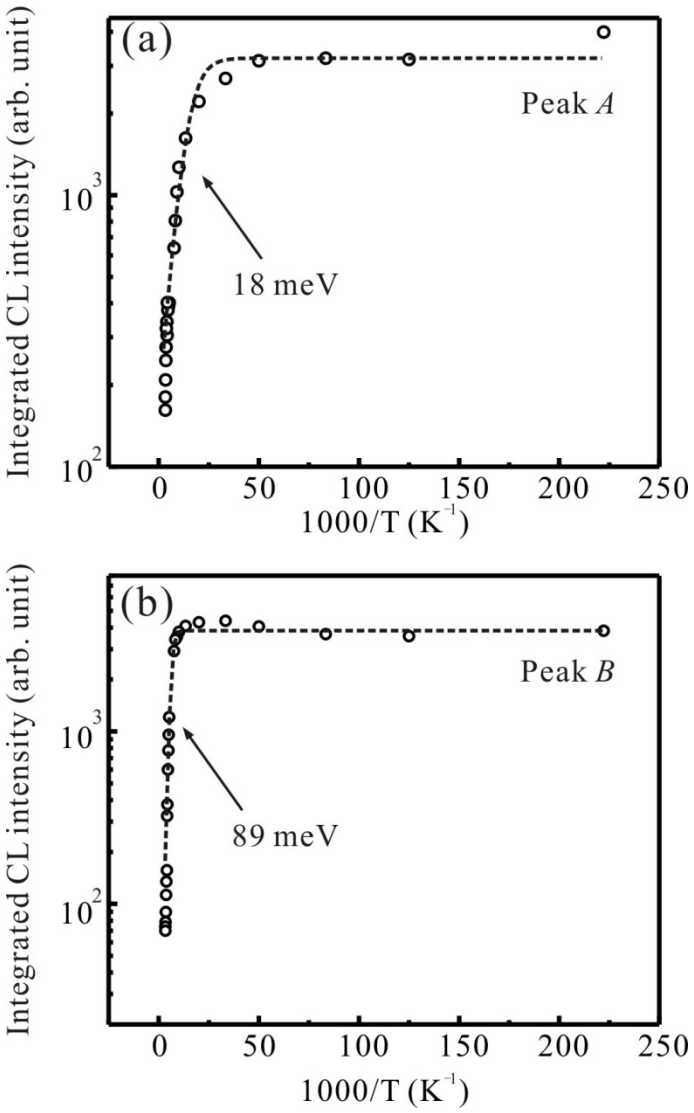

FIG. 5.8. Temperature dependence of the luminescence intensities of (a) peak *A* and (b) peak *B*. Dash lines correspond to least-square fit using equation (1).

5.10. CARRIER RECOMBINATION DYNAMICS INSIDE QUANTUM WELLS

The carrier excitation and recombination dynamics of the QW emissions were studied by time-resolved CL (TRCL) for temperatures between 4 and 300 K. Transients were obtained by blanking the electron beam with a square pulse, with a width of 100 ns at a frequency of 1 MHz. The temperature dependence of the time resolved CL transients is shown in Fig. 5.9(a). After the electron beam is switched on at t = 100 ns, the sampled region gets optically exited and the CL intensity builds up. At t = 200 ns, the electron beam is switched off and the de-excitation process is recorded. The observed TRCL de-excitation consists of two components corresponding to a fast decay and a slow decay. At temperatures above 200 K, the slow decay disappears and a single decay is observed. We introduce an effective lifetime in order to compare the recombination dynamics in this temperature range. The effective lifetime is obtained by fitting the QW emission decay with a single exponential decay. From the CL lifetimes (τ_{CL}) and integrated intensities, the radiative (τ_{rad}) and the non-radiative lifetimes (τ_{nonrad}) were derived on the basis of the following equations:

$$\eta = I(T) \Big/ I(4K) = (\frac{1}{\tau_{rad}}) / (\frac{1}{\tau_{CL}}),$$

$$\frac{1}{\tau_{CL}} = \frac{1}{\tau_{rad}} + \frac{1}{\tau_{nonrad}},$$

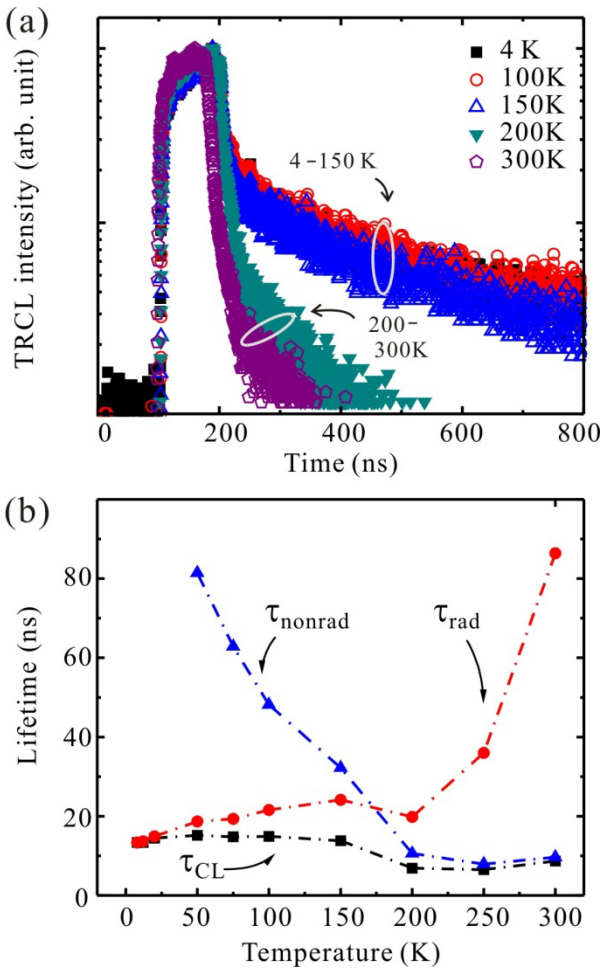

Fig. 5.9. Recombination dynamics of the quantum well emission. (a) Temperature-dependent time-resolved CL spectra taken in the 4 to 300 K range. A transition in the carrier recombination lifetime happens above 150 K. (b) CL lifetime τ_{CL}, radiative lifetime τ_r, and non-radiative lifetime τ_{nr} were deduced from the temperature-dependent TRCL data and integrated CL intensity.

The temperature dependence of the CL lifetime (τ_{CL}), the radiative lifetime (τ_{rad}), and the non-radiative lifetime (τ_{nonrad}) are shown in Fig. 5.9(b). An effective tool to evaluate the dimensionality of confinement is to measure the temperature dependence of the radiative lifetimes of excitons, which is of the form

$$\tau_{rad} \sim T^{d/2}$$

The radiative lifetime is observed to be independent of temperature in the 4 - 150 K range which agrees with excitons confined in the quasi-zero-dimension (0-D) potential,[98,99] an indication of excitons localized in the QW. Above 200 K, the radiative lifetime increases proportional to temperature. This linear behavior supports that excitons confined in the localized centers are thermalized to extended states confined inside a QW. At low temperatures, a noticeable portion of carriers experience the QCSE in the dislocated regions, where the electron and hole wave function overlap is reduced, resulting in a slow recombination process. Radiative and non-radiative recombination paths compete in the temperature range between 150 and 200 K. Above 200 K, carriers may be captured near the dislocations and undergo non-radiative recombination.

5.11. CONCLUSION

In conclusion, we have correlated the optical and structural properties of a blue LED structure grown on *m*-plane free-standing GaN. We observe an inhomogeneous QW emission with two distinct peaks at 462 (peak *A*) and 428 nm (peak *B*) at room temperature, which we associate with dislocated and dislocation-

free regions, respectively. The difference in peak energy positions may be explained by the presence of PE fields within the dislocated region and by the absence of these fields in the dislocation-free regions. The energy position of peak *A* exhibits a blue-shift with increasing electron beam current, which can be associated with screening of the PE fields. A slow recombination process, associated with the dislocated regions, becomes less favorable at higher temperatures, which may be due to thermal activation of carriers that were trapped in the vicinity of the dislocations.

REFERENCE

[78] C. P. Kuo, R. M. Fletcher, T. D. Osentowski, M. C. Lardizabal, M. G. Craford, and V. M. Robbins, Appl. Phys. Lett. **57**, 2937 (1990).

[79] S. Nakamura, T. Mukai, and M. Senoh, Appl. Phys. Lett. **64**, 1687 (1994).

[80] S. Nakamura, M. Senoh, S. Nagahama, N. Iwasa, T. Yamada, T. Matsushita, Y. Sugimoto, and H. Kiyoku, Appl. Phys. Lett. 69, 4056 (1996)

[81] D. Queren, A. Avramescu, G. Brüderl, A. Breidenassel, M. Schillgalies, S. Lutgen, and U. Strauß, Appl. Phys. Lett. **94**, 081119 (2009).

[82] T. Miyoshi, S. Masui, T. Okada, T. Yanamoto, T. Kozaki, S. Nagahama, and T. Mukai, Appl. Phys. Express **2**, 062201 (2009).

[83] F. Bernardini, V. Fiorentini, and D. Vanderbilt, Phys. Rev. B **56**, R10024 (1997).

[84] J. S. Im, H. Kollmer, J. Off, A. Sohmer, F. Scholz, and A. Hangleiter, Phys. Rev. B **57**, R9435 (1998).

[85] M. D. Craven, S. H. Lim, F. Wu, J. S. Speck, and S. P. DenBaars, Appl. Phys. Lett. **81**, 469 (2002).

[86] C. Q. Chen, V. Adivarahan, J. W. Yang, M. Shatalov, E. Kuokstis, and M. A. Khan, Jpn. J. Appl. Phys. **42**, L1039 (2003).

[87] R. Liu, A. Bell, F. A. Ponce, C. Q. Chen, J. W. Yang, and M. A. Khan, Appl. Phys. Lett. **86**, 021908 (2005).

[88] P. Waltereit, O. Brandt, M. Ramsteiner, A. Trampert, H. T. Grahn, J. Menniger, M. Reiche, R. Uecker, P. Reiche, and K. H. Ploog, Phys. Stat. Sol. A **180**, 133 (2000).

[89] M. C. Schmidt, K. C. Kim, H. Sato, N. Fellows, H. Masui, S. Nakamura, S. P. Denbaars, and J. S. Speck, Jpn. J. Appl. Phys. **46**, L126 (2007).

[90] T. Detchprohm, M. Zhu, Y. Li, L. Zhao, S. You, C. Wetzel, E. A. Preble, T. Paskova, and D. Hanser, Appl. Phys. Lett. **96**, 051101 (2010).

[91] K. Okamoto, J. Kashiwagi, T. Tanaka, and M. Kubota, Appl. Phys. Lett. **94**, 071105 (2009).

[92] A. M. Fischer, Z. H. Wu, K. W. Sun, Q. Y. Wei, Y. Huang, R. Senda, D. Iida, M. Iwaya, H. Amano, and F. A. Ponce, Appl. Phys. Express **2**, 041002 (2009).

[93] J. P. Hirth and J. Lothe: *Theory of Dislocations* (Krieger, Florida, 1982) p. 355.

[94] P. G. Eliseev, P. Perlin, J. Lee, and M. Osiński, Appl. Phys. Lett. **71**, 569 (1997).

[95] A. Bell, S. Srinivasan, C. Plumlee, H. Omiya, F. A. Ponce, J. Christen, S. Tanaka, A. Fujioka, and Y. Nakagawa, J. Appl. Phys. **95**, 4670 (2004).

[96] Q. Y. Wei, T. Li, Z. H. Wu, and F. A. Ponce, Phys. Stat. Sol. A **207**, 2226 (2010).

[97] S. Chichibu, T. Sota, K. Wada, and S. Nakamura, J. Vac. Sci. Technol. B **16**, 2204 (1998).

[98] T. Li, A. M. Fischer, Q. Y. Wei, F. A. Ponce, T. Detchprohm, and C. Wetzel, Appl. Phys. Lett. **96**, 031906 (2010).

[99] Y. Narukawa, Y. Kawakami, S. Fujita, and S. Nakamura, Phys. Rev. B **59,** 10283 (1999).

CHAPTER 6

INDIUM INCORPORATION IN AlInGaN ALLOYS

6.1. INTRODUCTION

Technological progress in growing AlGaN materials has led to the development of light-emitting devices operating in the ultraviolet range.[100-102] These devices have attracted much attention for several applications, such as water purification, biological agent detection, and solar blind communications.[103] AlGaN is a desirable candidate for the light-emitting device active region since it has a direct band gap between 3.4 and 6.2 eV. However, the device efficiency decreases for high aluminum contents. This is thought to be due to: (a) difficulty in growing high quality Al-rich AlGaN films; (b) lower carrier confinement with an energy gap increase of the well;[103] (c) poor *p*-type conductivity[104] in AlGaN alloys; and (d) unintended parasitic absorption followed by radiative emission between 300 and 400 nm whose origin still remains unclear. The longer wavelength emission can also result from the recombination of overflowing electrons with holes via Mg-related deep acceptor levels in the p-AlGaN layer,[105-108] or from deep-level transitions in the n-type AlGaN layer.[109,110] These parasitic emissions not only turn out to be competing channels against quantum well recombination, but also have a photon recycling effect. Since the parasitic emission is lower in energy than the quantum well emission, photon recycling further lowers the external quantum efficiency. Thus, a better understanding of the origin of these parasitic emissions is needed in order to suppress them. It is

also believed that the absence of alloy clustering in the AlGaN system lowers the radiative efficiency.[111] In this chapter, we also report on the effect of indium incorporation in the InAlGaN system.

6.2. InAlGaN FILMS

6.2.1. EXPERIMENTAL DETAILS

InAlGaN films, described in Fig. 6.1, were grown by metal-organic chemical vapor deposition (MOCVD) by Prof. Russell Dupuis' group at Georgia Institute of Technology. Their thickness range from 50 to 90 nm, and they were grown on 1 μm-thick (a) undoped GaN, or (b) undoped AlN underlayers. The growth conditions and information of these samples are listed in Table 6.1.

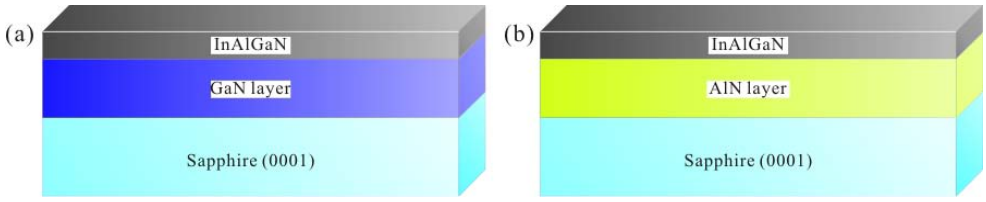

FIG. 6.1. Layers of the InAlGaN film structures with different substrates. (a) Sample S1 uses GaN as substrates while (b) the other samples use bulk GaN as substrates.

Table 6.1. *Growth characteristics and parameters for AlInGaN films S1 to S6.*

Sample No.	Substrate	Grow. Temp (°C)	Presure (Torr)
S1	GaN	--	250
S2	AlN	--	250
S3	AlN	842	250
S4	AlN	832	250
S5	AlN	812	250
S6	AlN	795	250

The InAlGaN films were grown at a pressure of 250 Torr, at growth temperatures from 842 ºC to 795 ºC, with lower temperatures incorporating more indium.

6.2.2. DETERMINATION OF ELEMENTAL COMPOSITION

Rutherford backscattering spectroscopy (RBS) was used to determine the actual elemental concentration in the InAlGaN films. The RBS results are shown in Fig. 6.2. The indium, aluminum, gallium, and nitrogen signals can be resolved from the RBS spectra. By carefully fitting the data based on scattering theory, the element concentration of the InAlGaN films were obtained and are shown in Fig. 6.3. We now focus on the effect of the choice of underlayer on the alloy composition in InAlGaN films. Using the element compositions from the RBS data and Vegard's law, the lattice parameter *a* of the S1 and S2 InAlGaN films is 0.3164 nm and 0.3156 nm, respectively. The basal plane strain of the InAlGaN film grown on GaN, sample S1, is -0.7%. The negative sign means that the film is under tensile stress. On the other hand, the basal strain for the InAlGaN films grown on AlN, sample S2, is 1.4%, the positive sign means the InAlGaN film is under compressive stress. The difference in basal strain on the InAlGaN film does not significantly affect the indium incorporation, as both samples contain the same [In] ~ 1%. However, the [Ga]/[Al] incorporation ratio seems to be affected by the strain. Under tensile stress, more gallium is incorporated into the InAlGaN film in order to relief the strain. In the same manner, under compressive strain, more aluminum is incorporated into the InAlGaN film in order to relief the strain.

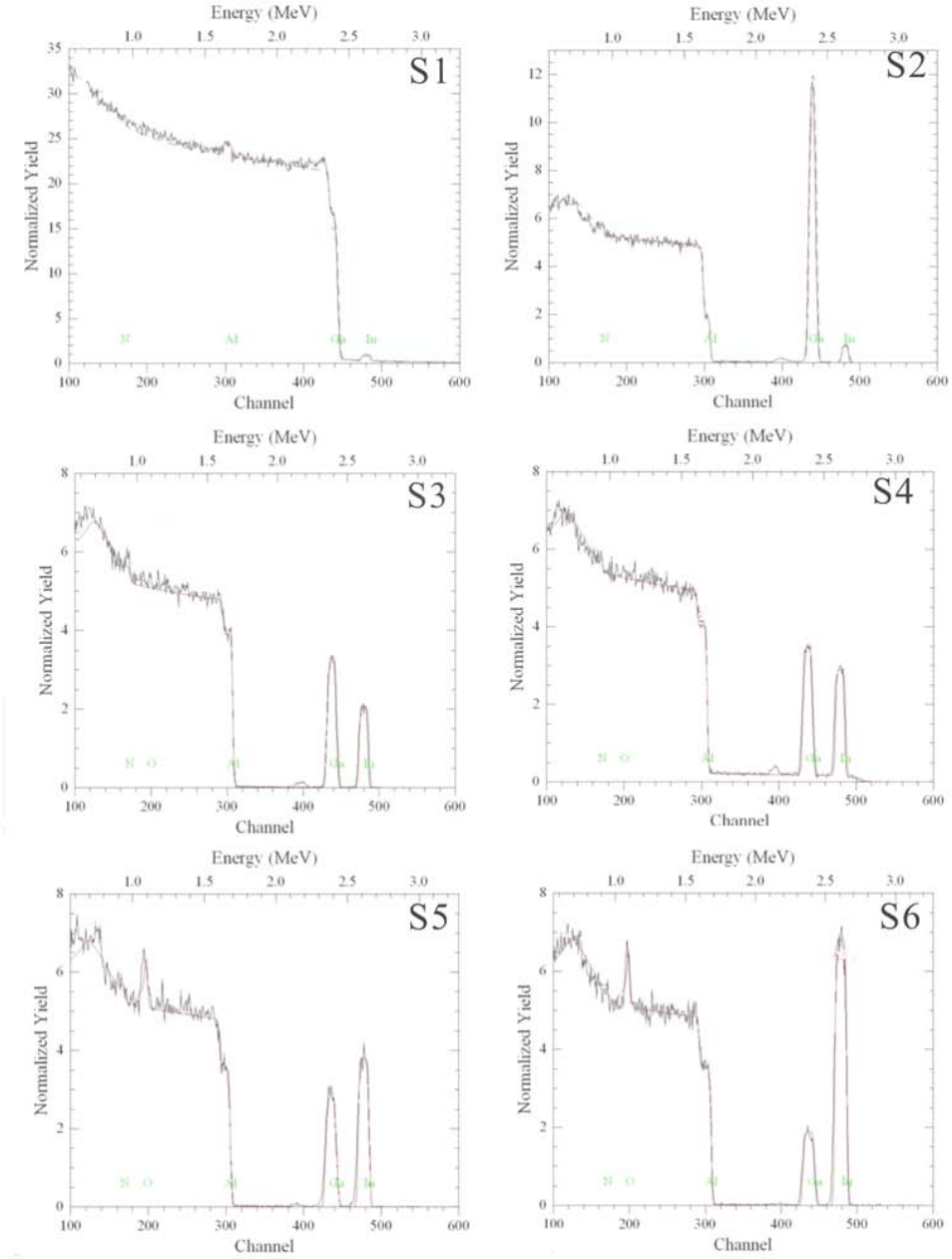

Fig. 6.2. Rutherford backscattering spectroscopy data of InAlGaN epitaxial films.

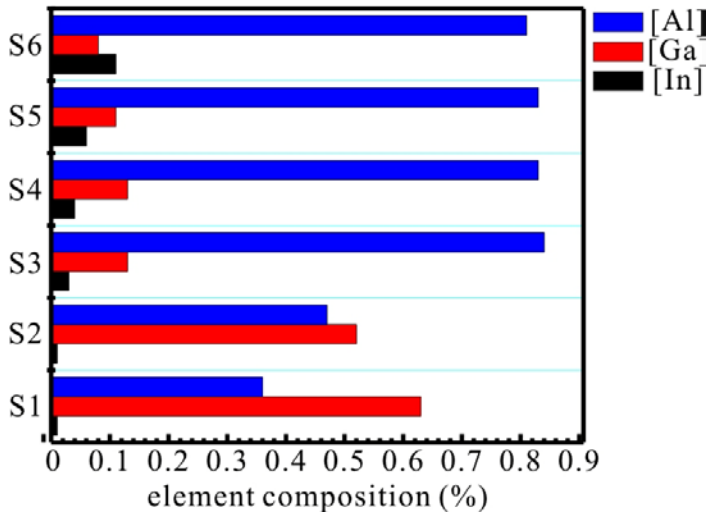

Fig. 6.3. The [In], [Ga] and [Al] element composition measured by RBS.

We will now discuss the effect of growth temperature on the alloy composition in InAlGaN films grown on AlN. We observe that the gallium (and indium) concentrations decrease (increase) by lowering the growth temperature, while the aluminum concentration remains constant. The RBS shows that [In] increases from 3 to 11%, while [Ga] decreases from 13 to 8%. The dependence between indium and gallium incorporation may be due to their relatively lower formation energies with nitrogen than that of AlN.

6.2.3. OPTICAL AND STRUCTURAL PROPERTIES

Next, we explore the luminescence properties of the InAlGaN films by cathodoluminescence. In Fig. 6.4, S1 exhibits a peak located at 309 nm (~ 4.01 eV), assigned to InAlGaN band-edge emission with FWHMs of 80 and 180 meV at 4 and 300 K, respectively. The broadening could be due to potential fluctuation or to the increase in non-radiative recombination. S2 shows a peak located at 272 nm (~ 4.55 eV) at 4 K and is assigned to the InAlGaN band-edge emission. The

InAlGaN band-edge emission is higher than S1 since more aluminum is incorporated into the film. The FWHMs of S2 are 170 and 230 meV at 4 and 300 K, respectively. Sample S2 exhibits larger FWHM values than S1, due to lower crystal quality, as will be discussed later in this section. We have compared the theoretical and experimental values of the band gap for S1 and S2. The band gap can be approximated by using the following equation for quaternary alloys:

$$E_g^{InAlGaN}(x,y,z) = E_g^{InN}x + E_g^{AlN}y + E_g^{GaN}z - b_{InAlN}xy - b_{InGaN}xz - b_{AlGaN}yz\,,$$

where E_g^{InN}, E_g^{AlN}, and E_g^{GaN} are the binary band gaps, and b_{InAlN}, b_{InGaN}, and b_{AlGaN} are the bowing parameters for the ternary InAlN, InGaN, and AlGaN alloys. We have used the bowing parameters found in Vurgaftman and Meyer's work.[112] The band gap energy is calculated to be 4.286 eV for S1 and 4.575 eV for S2.

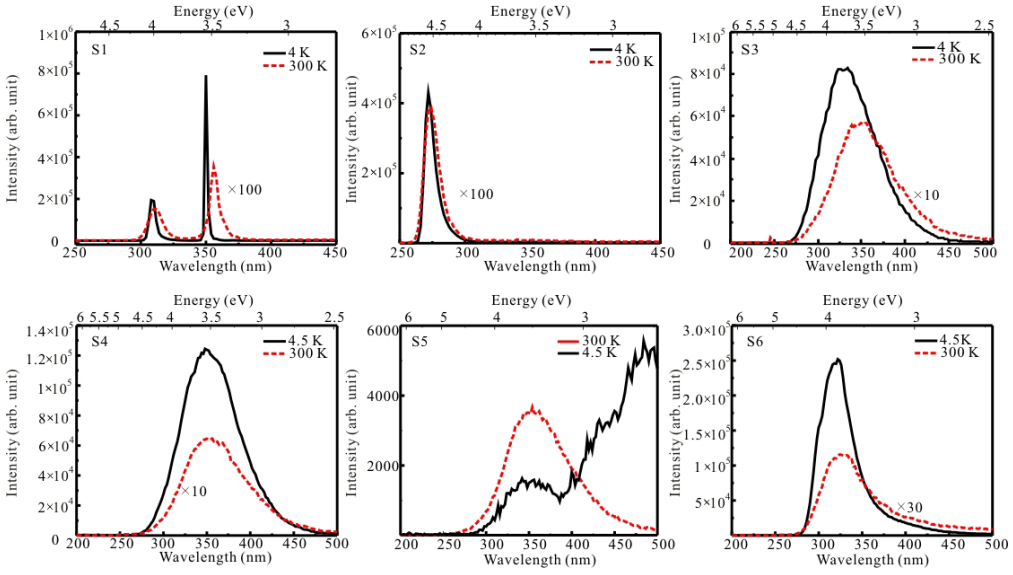

Fig. 6.4. CL spectra of samples S1, S2, S3, S4, S5 and S6, taken at liquid helium temperature (continuous line) and at room temperature (dotted line).

The luminescence properties of the films vary with element composition, as expected. The emission energies and FWHMs of all samples are plotted in Fig. 6.5. The FWHMs for all the quaternary alloys are very high (above 500 meV) perhaps due to large composition fluctuations. The emission energies are also much red-shifted from samples S1 and S2.

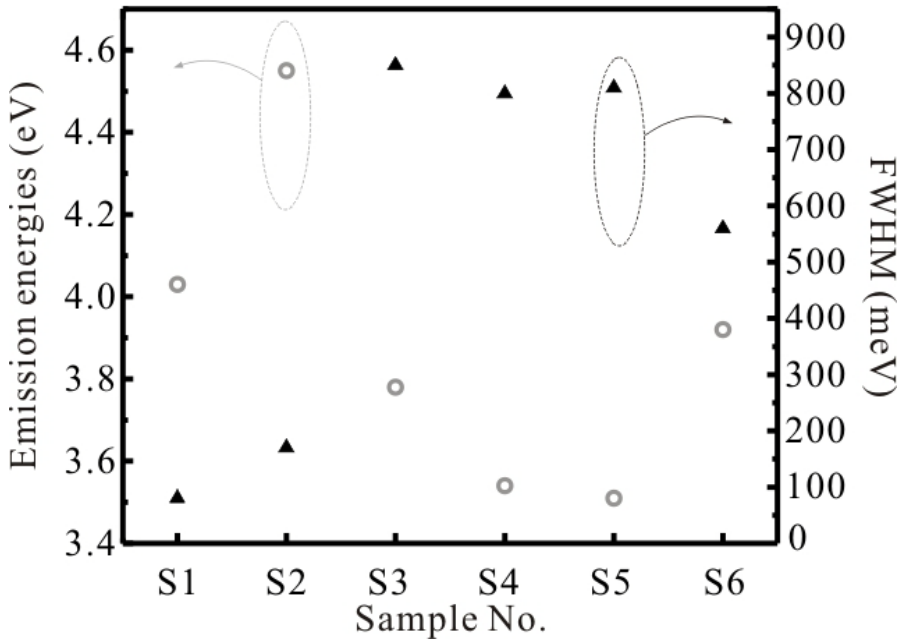

Fig. 6.5. CL emission energy and FWHM for sample S1, S2, S3, S4, S5, and S6.

We also notice that sample S6 has the highest indium and lowest gallium concentrations, among all samples. This sample should have the lowest energy emission, however, it luminescence at 3.92 eV, the highest energy among all quaternary materials and also the smallest FWHM. Thus, we infer that relatively high content of indium tend to relax the mismatch strain, and produce better luminescence.

Next we probe the microstructure of these InAlGaN films via TEM. The structure images of samples S1 and S2 are shown in Fig. 6.6.

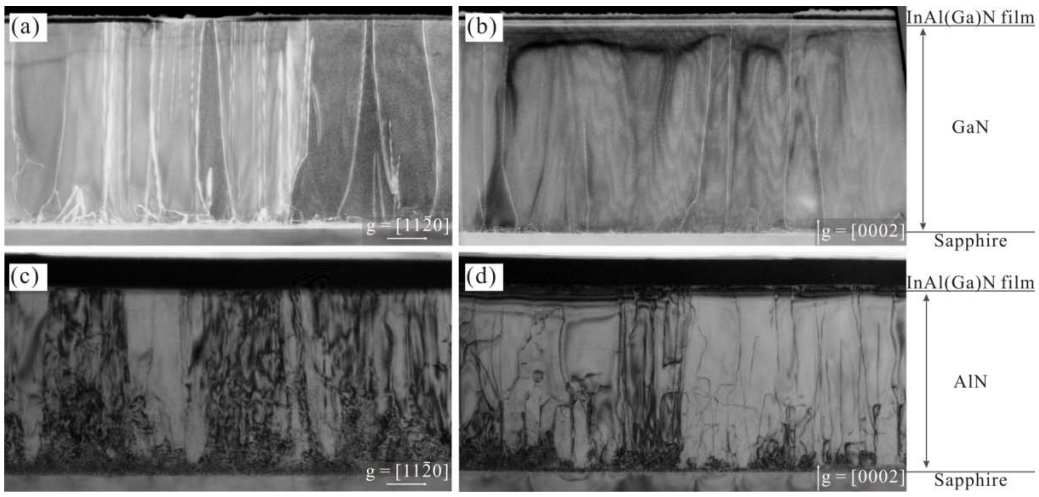

Fig. 6.6. TEM images show the micro-structure of sample S1 at (a) **g** = $[11\bar{2}0]$, and (b) **g** = [0002] conditions, and of sample S2 at (c) **g** = $[11\bar{2}0]$, and (d) **g** = [0002] conditions.

For sample S1, the GaN-on-sapphire layer onto which the InAlN film was grown exhibited a low dislocation density. Edge and mixed dislocations are dominant in the GaN layer, while screw dislocations are barely observed. For sample S2, the AlN under layers have a much higher defect density compared to the GaN under layer. The high density of dislocations in the AlN bulk layer could extend to the InAlGaN layer, compromising the crystal quality of the latter.

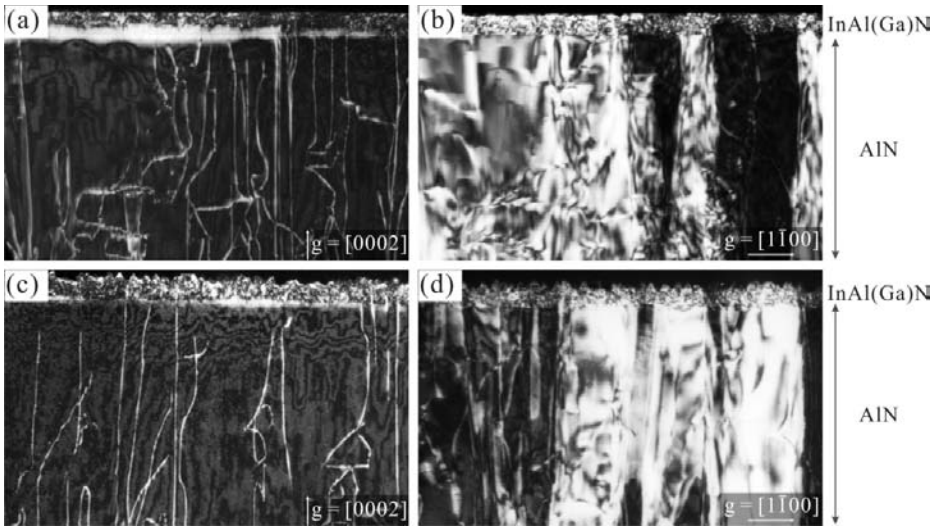

Fig. 6.7. TEM images showing the microstructure of sample S5 under (a) g = [0002], and (b) g = $[1\bar{1}00]$ conditions, and sample S6 under (c) g = [0002], and (d) g = $[1\bar{1}00]$ conditions.

For sample S5, a high density of dislocations is replicated from the AlN buffer layers through the film, as shown in Fig. 6.7. The film tends to have a planar growth mode, but the film surface is quite rough with V-pits observed. Threading dislocations with edge components tend to terminate at the interface between InAlGaN and AlN buffer layer. For sample S6, the InAlGaN film with an [In] ~ 11% exhibits a three-dimensional growth mode (Stranski-Krastanov mode), possibly due to the large lattice mismatch between InAlGaN film and AlN substrate.

6.3. CONCLUSIONS

The optical, structural, and compositional information of InAlGaN quaternary thin films grown on AlN or GaN substrate were studied by

cathodoluminescence, TEM, and RBS, respectively. The growth temperature is observed to have an effect on indium incorporation into the film. The [Ga]/[Al] incorporation ratio seems to be affected by the strain.

CHAPTER 7

SUMMARY AND FUTURE RESEARCH DIRECTIONS

7.1. SUMMARY

In this dissertation, we have investigated the optical and structural properties of polar and non-polar III nitrides. We first report the comparative study performed to optimize the conventional *c*-plane InGaN emitting structures with modifying parameters such as different substrates, insertion of InGaN waveguides, Si-doped quantum barriers, and different EBLs and the corresponding effects. Second, the strain relaxations, structural properties of non-polar *m*-plane InGaN films grown on free-standing GaN bulk were studied by RSM and TEM. It is observed the InGaN materials strain to GaN substrate when the Indium composition is low, while start to partially relax along *a*-direction rather than *c*-axis due to energy formation of a misfit dislocation. The luminescence and the recombination dynamics study indicate the localization mechanism in In-rich regions. Third, we analyzed the optical and structural properties of the non-polar *m*-plane InGaN LED structure. It is found that the lattice mismatch relaxation could introduce in-plane piezoelectric fields which would severely affect the luminescence. Finally, we explored the compositional, structural, and luminescent information of InAl(Ga)N quaternary films grown by MOCVD. The indium composition is found to be related to the growth temperature.

7.2. OPTIMIZATION OF *C*-PLANE INDIUM GALLIUM NITRIDE BASED LIGHT-EMITTING STRUCTURE (CHAPTER 3)

We have studied the optical properties of *c*-plane grown light-emitting InGaN structures with variations of parameters for optimization. For sapphire substrates, the residue strains still exist in GaN epilayer and blue-shift the emission wavelengths. The LD structures grown on sapphire have higher emission intensities than those grown on GaN bulk substrates for these provided LD structures. The insertion of an InGaN waveguide stabilize the QW emission with nearly no wavelength shift with increasing electron beam accelerating voltage. Moreover, the QW emission of the LED structure without EBL is much red-shifted from those with EBLs.

7.3. STUDY OF STRUCTURAL AND OPTICAL PROPERTIES ON *M*-PLANE INGAN FILMS WITH VARIED INDIUM CONCENTRATION (CHAPTER 4)

We have explored the properties of *m*-plane InGaN thin films grown by metal-organic chemical vapor deposition on free-standing *m*-plane GaN using CL and TEM. For the low indium samples, the film is fully strained on the substrate with few interfacial misfit dislocations are observed. For the high indium sample, the film is divided into two layers; the lower layer was fully strained along the *c*-axis but partially relaxed along the *a*-axis due to anisotropic strain and formation energy of a misfit dislocation. The upper layer was partially relaxed via stacking faults generated at the boundary of seriated shaped islands of the lower layer.

Cathodoluminescence also confirms a two layer growth by the observation of a square-like feature in lower layer emission wavelength but uniform in upper layer emission. It is also observed a slower radiative carrier recombination with increasing indium content.

7.4. OPTICAL AND STRUCTURAL EVIDENCES FOR THE EXISTENCE OF IN-PLANE PIEZOELECTRIC FIELDS IN *M*-PLANE QUANTUM WELLS (CHAPTER 5)

We have correlated the optical and structural properties of a blue LED structure grown on *m*-plane free-standing GaN. We observe an inhomogeneous QW emission with two distinct peaks at 462 (peak *A*) and 428 nm (peak *B*) at room temperature, which we associate with dislocated and dislocation-free regions, respectively. The difference in peak energy positions may be explained by the presence of PE fields within the dislocated region and by the absence of these fields in the dislocation-free regions. The energy position of peak *A* exhibits a blue-shift with increasing electron beam current, which can be associated with screening of the PE fields. A slow recombination process, associated with the dislocated regions becomes less favorable at higher temperatures, which may be due to thermal activation of carriers that were trapped in the vicinity of dislocations.

7.5. INDIUM INCORPORATION IN InAlGaN ALLOYS (CHAPTER 6)

We have investigated the optical, structural and compositional information of InAlGaN quaternary thin films grown on AlN or GaN substrate by cathodoluminescence, TEM and RBS, respectively. The growth temperature is found to affect indium incorporation into the film.

7.6. SUGGESTED FUTURE RESEARCH DIRECTIONS

Large lattice mismatch between GaN and InN is the main challenge in the production of longer-wavelength light-emitting devices. The piezoelectric fields cause parallel tilted bands while a graded indium composition will cause a uniformly varying bandgap. The combination of strain and bandgap can lead to a carefully designed graded quantum well that can counteract the effect of the piezoelectric field and maximize the overlap between electron and hole wavefuntions which would increase the radiative recombination significantly. This idea is expanded in Fig. 7.1.

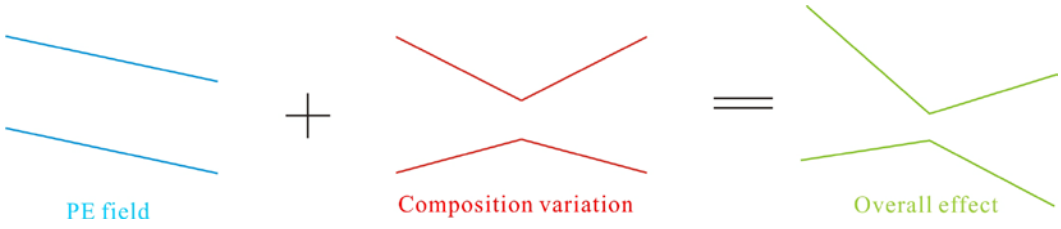

Fig. 7.1. Effect of combining PE fields and In composition variation to increase the radiative recombination efficiency.

The piezoelectric fields in the InGaN layers, due to the compressive strain by the GaN underlayer, tilt the electronic bands as shown in the left part of the figure. By increasing the indium incorporation and then decreasing it during growth, the band gap will first decrease and then increase to create a dip in the center regions of the layer as shown in the middle part of the figure. The overall effect of the two, piezoelectric fields and compositional variations, will produce tilted triangular-shaped conduction and valence band. The lowest point of conduction band is aligned to the highest point of valence band, thus the separation of the electron and hole wavefunctions are greatly reduced and the QCSE effect can be minimized. The idea mentioned above is a rough one. In order to get more symmetric conduction and valence band, detailed calculation will be needed to control the band gap engineering with piezoelectric fields taken into account.

REFERENCES

[1] F. A. Ponce and D. P. Bour, Nature (London) **386**, 351 (1997).

[2] D. L. Klipstein, The Great Internet Light Bulb Book, Part I, http://freespace.virgin.net/tom.baldwin/bulbguide.html (1996).

[3] J. M. Phillps, M. E. Coltrin, M. H. Crawford, A. J. Fischer, M. R. Krames, R. Mueller-Mach, G. O. Mueller, Y. Ohno, L. E. S. Rohwer, J. A. Simmons, and J. Y. Tsao, Laser & Photon. Rev, **4**, 307 (2007).

[4] J. A. Simmons, M. E. Coltrin, and J. Y. Tsao, Beyond the vacuum tube: lighting solutions for the 21st century, Optics and Photonics News (2007).

[5] R. Haitz and J. Y. Tsao, Phys. Stat. Solid. A **208**, 17 (2011).

[6] Jr. N. Holonyak and S. F. Bevacqua, Appl. Phys. Lett. **1**, 82 (1962).

[7] H. Rupprecht, J. M. Woodall, and G. D. Pettit, Appl. Phys. Lett. **11**, 81 (1967).

[8] H. Kressel and J. K. Bulter, *Semiconductor Lasers and Heterojunction LEDs* (Academic Press, New York)p. 608.

[9] D. G. Thomas, J. J. Hopfield, and C. J. Frosch, Phys. Rev. Lett. **15**, 857 (1965).

[10] C. P. Kuo, R. M. Fletcher, T. D. Osentowski, C. M. Lardizabel, M. G. Craford, and V. M. Robbins, Appl. Phys. Lett. **57**, 2937 (1990).

[11] F. C. Frank, *On Miller-Bravais Indices and four-dimensional Vectors*, Acta, Cryst. **18**, 862 (1965).

[12] O. Ambacher, J. Majewski, C. Miskys, A. Link, M. Hermann, M. Eickhoff, M. Stutzmann, F. Bernardini, V. Fiorentini, V. Tilak, B. Schaff, and L. F. Eastman, J. Phys.: Condens. Matter **14** 3399 (2002).

[13] F. A. Ponce, *Introduction to Nitride Semiconductor Blue Lasers and Light Emitting Diodes*, edited by S. Nakamura and S. F. Chichibu (Taylor and Francis Ltd., London, 2000), Chapter 4.

[14] D. Chandrasekhar, D. J. Smith, S. Strite, M. E. Lin, and H. Morkoc, J. Cryst. Growth, 152. 135 (1995).

[15] S. Yoshida, S. Misawa, and S. Gonda, Appl. Phys. Lett. **42**, 427 (1983).

[16] H. Amano, N. Sawaki, I. Akasaki, and Y. Toyoda, Appl. Phys. Lett.**48**, 353 (1986).

[17] S. Nakamura, Jpn. J. Appl. Phys. **30**, L1705 (1991).

[18] J. A. Vechten, J. D. Zook, and R. D. Horning, Jpn. J. Appl. Phys., Part 1 **31**, 3662 (1992).

[19] H. Amano, M. Kito, K. Hiramatsu, and I. Akasaki, Jpn. J. Appl. Phys. **28**, L2112 (1989).

[20] S. Nakamura, T. Mukai, M. Senoh, and N. Iwasa, Jpn. J. Appl. Phys. **31**, L139 (1992).

[21] S. Nakamura and T. Mukai, Jpn. J. Appl. Phys. **31**, L1457 (1992).

[22] S. Nakamura, T. Mukai,and M. Senoh, J. Appl. Phys. **76**, 8189 (1994).

[23] T. Mukai, S. Narimatsu, and S. Nakamura, Jpn. J. Appl. Phys. **37**, L479 (1998).

[24] S. Nakamura, M. Senoh, S. Nagahama, N. Iwasa, T. Yamada, T. Matsushita, H. Kiyoku, and Y. Sugimoto, Jpn. J. Appl. Phys. **35**, L74 (1996).

[25] I .Akasaki, H. Amano, Y. Koide, K. Hiramatsu, and N. Sawaki, J. Cryst. Growth **98**, 209 (1989).

[26] W. A. Melton and J. I. Pankove, J. Cryst. Growth **178**, 168 (1997).

[27] S. Nakamura, Science **281**, 956 (1998).

[28] S. Pereira, M. R. Correia, E. Pereira, K. P. O'Donnell, C. Trager-Cowan, and F. Sweeney, Phys. Rev. B **64**, 205311 (2001).

[29] F. Bernardini, V. Fiorentini, and D. Vanderbilt, Phys. Rev. B **56**, 10024 (1997).

[30] S. D. Lester, F. A. Ponce, M. G. Craford, and D. A. Steigerwald, Appl. Phys. Lett. **66**, 1249 (1995).

[31] M. D. Craven, S. H. Lim, F. Wu, J. S. Speck, and S. P. DenBaars, Appl. Phys. Lett. **81**, 469 (2002).

[32] T. S. Zheleva, O. H. Nam, M. D. Bremser, and R. F. Davis, Appl. Phys. Lett. **71**, 2472 (1997).

[33] I. Ho and G. B. Stringfellow, Appl. Phys. Lett. **69**, 2701 (1996).

[34] F. B. Naranjo, M. A. Sanchez-Garcia, F. Calle, and E. Calleja, Appl. Phys. Lett.**80**, 231 (2002).

[35] S. Chichibu, T. Azuhata, T. Sota, and S. Nakumara, Appl. Phys. Lett 69, 4188 (1996).

[36] B. G. Yacobi and D. B. Holt, Cathodoluminescence Microscopy of Inorganic Solids (Plenum Press, New York, 1990).

[37] J. I. Goldstein, D. E. Newbury, P. Echlin, D. C. Joy, C. Fiori, and E. Lifshin, Scanning Electron Microscopy and X-ray Microanalysis, 1stedn. (Plenum Press, New York, 1981).

[38] T. E. Everhart, J. Appl. Phys. **31**, 1483 (1960).

[39] G. D. Archard, J. Appl. Phys. **32**, 1505 (1961).

[40] G. D. Archard and T. Mulvey, Brit. J. Appl. Phys. **14**, 626 (1963).

[41] C. A. Klein, J. Appl. Phys. **39**, 2029 (1968).

[42] T. E. Everhart and P. H. Hoff, J. Appl. Phys. **42**, 5837 (1971).

[43] K. Kanaya and S. Okayama, J. Phys. D: Appl. Phys. **5**, 43 (1972).

[44] K. Fleischer, M. Toth, M. R. Phillips, and J. Zou, Appl. Phys. Lett. **74**, 1114 (1999).

[45] W. Becker, Advanced Time-Correlated Single Photon Counting Techniques (Springer, Berlin, 2005).

[46] S. F. Chichibu, A. C. Abare, M. S. Minsky, S. Keller, S. B. Fleischer, J. E. Bowers, E. Hu, U. K. MIshra, L. A. Coldren, and S. P. DenBaars, Appl. Phys. Lett. **73**, 2006 (1998).

[47] A. Wakahara, T. Tokuda, X. Z. Dang, S. Noda, and A. Sasaki, Appl. Phys. Lett. **71**, 906 (1997).

[48] I. H. Ho and G. B. Stringfellow, J. Cryst. Growth **178**, 1 (1997).

[49] D. H. Youn, M. Lachab, M. Hao, T. Sugahara, H. Takenaka, Y. Naoi, and S. Sakai, Jpn. J. Appl. Phys. **38**, 631 (1999).

[50] S. Nakamura, T. Mukai, M. Senoh, and N. Iwasa, Jpn. J. Appl. Phys. **31**, L139 (1992).

[51] T. S. Jeong, J. H. Kim, M. S. Han, K. Y. Lim, and C. J. Youn, J. Cryst. Growth **280**, 357 (2005).

[52] J. P. Liu, J. H. Ryou, R. D. Dupuis, J. Han, G. D. Shen, and H. B. Wang, Appl. Phys. Lett. **93**, 021102 (2008).

[53] S. Choi, H. J. Kim, S. S. Kim, J. P. Liu, J. Kim, J. H. Ryou, R. D. Dupuis, A. M. Fischer, and F. A. Ponce, Appl. Phys. Lett. **96**, 221105, (2010).

[54] A. M. Fischer, K. W. Sun, R. Juday, F. A. Ponce, J. H. Ryou, H. J. Kim, S. Choi, S. S. Kim, and R. D. Dupuis, Appl. Phys. Express **3**, 031003 (2010).

[55] S. Ruvimov, Z. L. Weber, T. Suski, J. W. Ager III, J. Washburn, J. Krueger, C. Kisielowski, E. R. Weber, H. Amano, and I. Akasaki, Appl. Phys. Lett. **69**, 990 (1996).

[56] K. C. Zeng, J. Y. Lin, and H. X. Jiang, A. Salvador, G. Popovici, H. Tang, W. Kim, and H. Morkoc, Appl. Phys. Lett. **71**, 1368 (1997).

[57] M. Kubota, K. Okamoto, T. Tanaka, and H. Ohta, Appl. Phys. Lett. **92**, 011920 (2008).

[58] H. Masui, H. Yamada, K. Iso, S. Nakamura, and S. P. DenBaars, J. Phys. D: Appl. Phys. **41** 225104 (2008).

[59] B. M. Imer, F. Wu, S. P. DenBaars, and J. S. Speck, Appl. Phys. Lett. **88**, 061908 (2006).

[60] A. Chitnis, C. Chen, V. Adivarahan, M. Shatalov, E. Kuokstis, V. Mandavilli, J. Yang, and M. Asif Khan, Appl. Phys. Lett. **84**, 3663 (2004).

[61] O. Brandt, Y. J. Sun, L. Däweritz, and K. H. Ploog, Phys. Rev. B **69**, 165326 (2004).

[62] Q. Sun, S. Y. Kwon, Z. Ren, J. Han, T. Onuma, S. F. Chichibu, and S. Wang, Appl. Phys. Lett. **92**, 051112 (2008).

[63] C. D. Lee, R. M. Feenstra, J. E. Northrup, L. Lymperakis, and J. Neugebauer, Appl. Phys. Lett. **82**, 1793 (2003).

[64] K. Xu, J. Xu, P. Z. Deng, Y. Z. Zhou, G. Q. Zhou, R. S. Qiu, Z. J. Fang, J. Cryst. Growth **193**, 127 (1998).

[65] K. R. Wang, M. Ramsteiner, C. Mauder, Q. Wan, T. Hentschel, H. T. Grahn, H. Kalisch, M. Heuken, R. H. Jansen, and A. Trampert, Appl. Phys. Lett. **96**, 231914 (2010).

[66] D. Iida, A. Miura, Y. Okadome, Y. Tsuchiya, T. Kawashima, T. Nagai, M. Iwaya, S. Kamiyama, H. Amano, and I. Akasaki, Phys. Status Solidi A **204**, 2005 (2007).

[67] T. Kawashima, T. Nagai, D. Iida, A. Miura, Y. Okadome, Y. Tsuchiya, M. Iwaya, S. Kamiyama, H. Amano, and I. Akasaki, Phys. Status Solidi B **244**, 1848 (2007).

[68] H. P. Maruska and J. J. Tietjen, Appl. Phys. Lett. **15**, 327 (1969).

[69] C. Q. Chen, M. E. Gaevski, W. H. Sun, E. Kuokstis, J. P. Zhang, R. S. Fareed, H. M. Wang, J. W. Yang, G. Simin, M. A. Khan, H. P. Maruska, D. W. Hill, M. M. C. Chou, and B. Chai, Appl. Phys. Lett. **81**, 3194 (2002).

[70] K. Fujito, K. Kiyomi, T. Mochizuki, H. Oota, H. Namita, S. Nagao, and I. Fujimura, Phys. Status Solidi A **205**, 1056 (2008).

[71] A. Hirai, Z. Jia, M. C. Schmidt, R. M. Farrell, S. P. DenBaars, S. Nakamura, J. S. Speck, and K. Fujito, Appl. Phys. Lett**. 91**, 191906 (2007).

[72] H. Yamada, K. Iso, H. Masui, M. Saito, K. Fujito, S. P. Denbaars, S. Nakamura, J. Cryst. Growth **310**, 4968 (2008).

[73] A. Chakraborty, S. Keller, C. Meier, B. A. Haskell, S. Keller, P. Waltereit, S. P. DenBaars, S. Nakamura, J. S. Speck, and U. K. Mishra, Appl. Phys. Lett. **86**, 031901 (2005).

[74] T. Onuma, T. Koyama, A. Chakraborty, M. McLaurin, B. A. Haskell, P. T. Fini, S. Keller, S. P. DenBaars, J. S. Speck, S. Nakamura, U. K. Mishra, T. Sota, and S. F. Chichibu, J. Vac. Sci. Technol. B **25**, 1524 (2007).

[75] A. Kobayashi, S. Kawano, Y. Kawaguchi, J. Ohta, and H. Fujioka, Appl. Phys. Lett. **90**, 041908 (2007).

[76] A. Miura, T. Nagai, R. Senda, T. Kawashima, M. Iwaya, S. Kamiyama, H. Amano, I. Akasaki, J. Cryst. Growth **310**, 3308 (2008).

[77] T. Paskova, Phys. Status Solidi B **245**, 1011 (2008).

[78] C. P. Kuo, R. M. Fletcher, T. D. Osentowski, M. C. Lardizabal, M. G. Craford, and V. M. Robbins, Appl. Phys. Lett. **57**, 2937 (1990).

[79] S. Nakamura, T. Mukai, and M. Senoh, Appl. Phys. Lett. **64**, 1687 (1994).

[80] S. Nakamura, M. Senoh, S. Nagahama, N. Iwasa, T. Yamada, T. Matsushita, Y. Sugimoto, and H. Kiyoku, Appl. Phys. Lett. 69, 4056 (1996)

[81] D. Queren, A. Avramescu, G. Brüderl, A. Breidenassel, M. Schillgalies, S. Lutgen, and U. Strauß, Appl. Phys. Lett. **94**, 081119 (2009).

[82] T. Miyoshi, S. Masui, T. Okada, T. Yanamoto, T. Kozaki, S. Nagahama, and T. Mukai, Appl. Phys. Express **2**, 062201 (2009).

[83] F. Bernardini, V. Fiorentini, and D. Vanderbilt, Phys. Rev. B **56**, R10024 (1997).

[84] J. S. Im, H. Kollmer, J. Off, A. Sohmer, F. Scholz, and A. Hangleiter, Phys. Rev. B **57**, R9435 (1998).

[85] M. D. Craven, S. H. Lim, F. Wu, J. S. Speck, and S. P. DenBaars, Appl. Phys. Lett. **81**, 469 (2002).

[86] C. Q. Chen, V. Adivarahan, J. W. Yang, M. Shatalov, E. Kuokstis, and M. A. Khan, Jpn. J. Appl. Phys. **42**, L1039 (2003).

[87] R. Liu, A. Bell, F. A. Ponce, C. Q. Chen, J. W. Yang, and M. A. Khan, Appl. Phys. Lett. **86**, 021908 (2005).

[88] P. Waltereit, O. Brandt, M. Ramsteiner, A. Trampert, H. T. Grahn, J. Menniger, M. Reiche, R. Uecker, P. Reiche, and K. H. Ploog, Phys. Stat. Sol. A **180**, 133 (2000).

[89] M. C. Schmidt, K. C. Kim, H. Sato, N. Fellows, H. Masui, S. Nakamura, S. P. Denbaars, and J. S. Speck, Jpn. J. Appl. Phys. **46**, L126 (2007).

[90] T. Detchprohm, M. Zhu, Y. Li, L. Zhao, S. You, C. Wetzel, E. A. Preble, T. Paskova, and D. Hanser, Appl. Phys. Lett. **96**, 051101 (2010).

[91] K. Okamoto, J. Kashiwagi, T. Tanaka, and M. Kubota, Appl. Phys. Lett. **94**, 071105 (2009).

[92] A. M. Fischer, Z. H. Wu, K. W. Sun, Q. Y. Wei, Y. Huang, R. Senda, D. Iida, M. Iwaya, H. Amano, and F. A. Ponce, Appl. Phys. Express **2**, 041002 (2009).

[93] J. P. Hirth and J. Lothe: *Theory of Dislocations* (Krieger, Florida, 1982) p. 355.

[94] P. G. Eliseev, P. Perlin, J. Lee, and M. Osiński, Appl. Phys. Lett. **71**, 569 (1997).

[95] A. Bell, S. Srinivasan, C. Plumlee, H. Omiya, F. A. Ponce, J. Christen, S. Tanaka, A. Fujioka, and Y. Nakagawa, J. Appl. Phys. **95**, 4670 (2004).

[96] Q. Y. Wei, T. Li, Z. H. Wu, and F. A. Ponce, Phys. Stat. Sol. A **207**, 2226 (2010).

[97] S. Chichibu, T. Sota, K. Wada, and S. Nakamura, J. Vac. Sci. Technol. B **16**, 2204 (1998).

[98] T. Li, A. M. Fischer, Q. Y. Wei, F. A. Ponce, T. Detchprohm, and C. Wetzel, Appl. Phys. Lett. **96**, 031906 (2010).

[99] Y. Narukawa, Y. Kawakami, S. Fujita, and S. Nakamura, Phys. Rev. B **59,** 10283 (1999).

[100] J. Han, M. H. Crawford, R. J. Shul, J. J. Figiel, M. Banas, L. Zhang, Y. K. Song, H. Zhou, and A. V. Nurmikko, Appl. Phys. Lett. **73**, 1688 (1998).

[101] A. Kinoshita, H. Hirayama, M. Ainoya, Y. Aoyagi, and A. Hirata, Appl. Phys. Lett. **77**, 175 (2000).

[102] H. Hirayama, J. Appl. Phys. **97**, 091101 (2005).

[103] M. A. Khan, M. Shatalov, H. P. Maruska, H. M. Wang, and E. Kuokstis, Jpn. J. Appl. Phys. **44**, 7191 (2005).

[104] J. Li, T. N. Oder, M. L. Nakarmi, J. Y. Lin, and H. X. Jiang, Appl. Phys. Lett. **80**, 1210 (2002).

[105] A. Chitnis, R. Pachipulusu, V. Mandavilli, M. Shatalov, E. Kuokstis, J. P. Zhang, V. Adivarhan, S. Wu, G. Simin, and M. A. Khan, Appl. Phys. Lett. **81**, 2938 (2002).

[106] J. S. Park, D. W. Fothergill, P. Wellenius, S. M. Bishop, J. F. Muth, and R. F. Davis, Jpn. J. Appl. Phys. **45**, 4083 (2006).

[107] J. C. Zhang, Y. H. Zhu, T. Egawa, S. Sumiya, M. Miyoshi, and M. Tanaka, Appl. Phys. Lett. **93**, 131117 (2008).

[108] K. B. Lee, P. J. Parbrook, T. Wang, J. Bai, F. Ranalli, R. J. Airey, and G. Hill, J. Cryst. Growth **311**, 2857 (2009).

[109] K. X. Chen, Q. Dai, W. Lee, J. K. Kim, E. F. Schubert, W. Liu, S. Wu, X. Li, and J. A. Smart, Appl. Phys. Lett. **91**, 121110 (2007).

[110] W. H. Yang, S. P. Li, H. Y. Chen, D. Y. Liu, and J. Y. Kang, J. Mater. Res. **25**, 1037 (2010).

[111] A. Khan, K. Balakrishnan, and T. Katona, Nature Photonics **2**, 77 (2008).

[112] I. Vurgaftman and J. R. Meyer, J. Appl. Phys. **94**, 3675 (2003).

APPENDIX I

LIST OF PUBLICATIONS DURING THE STUDY TOWARDS THE DOCTORAL DEGREE

Publications that resulted from my work leading to this dissertation are listed below:

1. Y. Huang, K. W. Sun, A. M. Fischer, Q. Y. Wei, R. Juday, F. A. Ponce, R. Kato and T. Yokogawa, *Effect of misfit dislocations on luminescence in m-plane InGaN quantum wells*, Appl. Phys. Lett. **98**, 261914 (2011).

2. A. M. Fischer, Z. H. Wu, K. W. Sun, Q. Y. Wei, Y. Huang, R. Senda, D. Iida, M. Iwaya, H. Amano, and F. A. Ponce, *Misfit strain relaxation by stacking fault generation in InGaN quantum wells grown on m-plane GaN*, Appl. Phys. Express **2** 041002 (2009).

APPENDIX II

PERMISSION FROM COAUTHORS

The coauthors of the publication that is part of chapter 5 have given their permission for use of the publication contents in this thesis.